A STUDY OF THE ELASTIC SCATTERING OF PROTONS BY N^{15}

Thesis by

Fred B. Hagedorn

In Partial Fulfillment of the Requirements

For the Degree of

Doctor of Philosophy

California Institute of Technology

Pasadena, California

1957

ACKNOWLEDGEMENTS

The author wishes to express his gratitude to Professors W. A. Fowler, T. Lauritsen, and C. C. Lauritsen for their guidance, advice, and assistance throughout the course of this work. In addition, numerous discussions with Professor R. F. Christy and Dr. F. S. Mozer about the analysis procedure and theoretical implications of the results have been very helpful and much appreciated. Thanks are also extended to Mr. J. C. Overley for his assistance with the experimental work and to the entire staff of the Kellogg Radiation Laboratory for its assistance with various aspects of this research.

ABSTRACT

A technique has been developed for preparing N^{15} targets which are satisfactory for the study of protons elastically scattered from N^{15}. Three excitation curves and nineteen angular distributions have been measured for $N^{15}(pp)N^{15}$ in the incident proton energy range from 600 to 1800 kev. These data have been analyzed and are consistent with the following excited states in O^{16}: an s-wave $J = 0^-$ state near 710 kev; a d-wave $J = 2^-$ state near 898 kev; an s-wave $J = 1^-$ state near 1028 kev; a d-wave $J = 3^-$ state near 1210 kev; and a p-wave $J = 1^+$ state near 1640 kev.

TABLE OF CONTENTS

TABLE OF CONTENTS (Cont'd)

I. INTRODUCTION

A detailed investigation of nuclear properties and characteristics has been in progress for many years. It is now generally agreed that nuclear energy levels or excited states exist and that each energy level may be characterized by specifying certain quantities such as the excitation energy, decay times for the various modes of decay, total angular momentum, parity, and isotopic spin admixtures. The systematic search for such energy levels, with the subsequent determination of their nuclear parameters, is an important field of nuclear experimentation since this type of information should be useful in acquiring further understanding of nuclear forces and nuclear structure.

The research reported herein is a part of this systematic search for and classification of nuclear energy levels, being concerned with the excited states of O^{16} which can be formed by combining the N^{15} nucleus with protons in the energy range of 600 to 1800 kev (corresponding to an O^{16} excitation energy range of 12.67 to 13.80 Mev). Once formed, such states may, considering only mass-energy conservation, break up in four different ways (excluding prompt beta processes):

$$N^{15} + P \rightarrow O^{16*} \begin{cases} \rightarrow N^{15} + P & Q = 0 \\ \rightarrow C^{12} + a_0 & Q = 4.96 \text{ Mev} \\ \rightarrow C^{12*} + a_1 & Q = 0.53 \text{ Mev} \\ \rightarrow O^{16} + \gamma & Q = 12.11 \text{ Mev} \end{cases}$$

The symbol O^{16*} here represents any of a number of excited states in O^{16}. This decay scheme is often simplified since many states do not break up in all four ways. An added complication, though,

is that the $N^{15}(p\gamma)O^{16}$ reaction can, in principle, leave the O^{16} nucleus in any one of its excited states lower than the one in question (to be followed, of course, by a subsequent radiation emission).

At the time the present research was initiated, considerable information about this particular region of excitation in O^{16} was available (see pages 134-138 of reference 1 for a complete summary and further references). Studies had been made of the α_0-particles, the α_1-particles, the 4.43-Mev gamma rays from C^{12} following the α_1 emission, and the capture gamma rays leaving O^{16} in its ground state. These studies had disclosed excited states at incident proton energies of 898, 1050, 1210 and 1640 kev. In addition excited states were known to exist at 340 and 430 kev. These energies are below the range studied in the present work, and no further mention will be made of these states.

The 898-kev state had been shown to decay by α_1-particles. Decay by either α_0-particles or the ground state gamma ray transition had been investigated and not observed. The angular correlation between the α_1-particles and the 4.43-Mev gamma rays from C^{12} had been measured as had also the separate α_1 and gamma ray angular distributions. All of this experimental evidence was consistent with d-wave proton formation of a $J = 2^-$ state.

The 1050-kev state had been shown to decay by both kinds of α-particles and by a 13-Mev gamma ray transition to the ground state of O^{16}. The large radiative width for the gamma ray reaction indicated an electric dipole transition, thereby implying a

$J = 1^-$ state. Isotropy of the 13-Mev gamma rays suggested formation by s-wave protons, which could combine with the $J = \frac{1}{2}^-$ N^{15} nucleus to form $J = 1^-$. The assignment $J = 1^-$ was also consistent with the fact that α_0-particle break-up requires spin-parity to be even-even or odd-odd, because of angular momentum conservation (using $J = 0^+$ for the ground state of C^{12}). However, it would be interesting to know with more certainty if there is but one excited state responsible for these three modes of decay. Electric dipole radiation would be forbidden (2) if the 1050-kev state had isotopic spin equal to zero ($T = 0$) and α-particle decay would be forbidden if $T = 1$. Hence, either two states exist or there is an admixture of $T = 0$ and $T = 1$ in the same state.

Both kinds of α-particles were shown to result from the 1210-kev state, the α_0-particles making an even-even or odd-odd assignment again necessary. The ground state gamma ray transition had been investigated and was not found. Separate angular distributions of the α_1-particles and the 4.43-Mev gamma rays from C^{12} appeared to require $J = 4^+$ or greater. Such an assignment was not entirely satisfactory, however, because it required the state to be formed by at least f-wave protons. The single particle limit of the partial proton width for such a state is about 0.006 of the observed total width of 22.5 kev. By means of the Breit-Wigner single level formula, this places an upper limit of 0.4 barns on the reaction cross section. Since the measured reaction cross section was about 0.7 barns (3,4,5), the formation of a $J = 4^+$ state by f-wave protons was questionable.

A unique assignment had not been established for the 1640-kev state. Investigation of this state had shown it to decay by α_1-particles but α_0-particles and the ground state gamma transition had not been observed. Angular distributions of the 4.43-Mev gamma rays from C^{12} had been measured and were consistent with either $J = 1^+$ or 2^-.

Therefore, of the four excited states in O^{16} that were known to exist in the energy region of interest, only the one at 898 kev had a unique assignment that was consistent with all of the available experimental evidence. None of the earlier studies in this region of excitation had included measurements of the protons elastically scattered from N^{15} because of the difficulty in preparing satisfactory targets for this experiment. In view of the desirability for additional information which might produce more definite assignments for the excited states discussed above, further investigation of this target problem seemed worthwhile.

A study of the elastic scattering of charged particles from nuclei in general reveals more information about the nucleus than other nuclear interactions. This is because the elastic scattering process depends on both the Coulomb amplitude (Rutherford scattering) and the nuclear amplitude. Interference between these two amplitudes enables the comparison of both the phase and magnitude of the nuclear amplitude with that of the Coulomb amplitude. Because these interference terms are proportional to the first power and not the square of the nuclear amplitude, scattering is a very sensitive tool.

The formal theory of scattering has been given by Bethe (6). The general approach of this theory is to describe the effects of the nuclear interaction in terms of several nuclear parameters, such as phase shifts, partial widths, and spins. The wave functions of the incident and scattered particles are written in terms of spherical harmonics and in this way phase shifts are associated with different values of orbital angular momentum for the incident and scattered particles. Calculation of the flux of scattered particles provides an expression for the differential cross section involving the incident energy, the scattering angle and the nuclear parameters. The energy and angle dependence and the absolute value of the measured cross section are then used to evaluate the unknown nuclear quantities. A more detailed discussion of this evaluation process is given in a later section.

Of importance for the present is the fact that analysis of the scattering data will provide much information about compound nuclear states. The excitation energy, spin, parity, total width, and proton partial width of a state can frequently be uniquely determined in this manner. Information about the nature of the non-resonant scattering may also be obtained. And in the case of $N^{15}(pp)N^{15}$, a study of any $J = 0^-$ states in this region of excitation could be made. Such states can decay neither by alpha particles nor through the ground state gamma ray transition because of angular momentum conservation and hence would not have been observed in the previous investigations.

It was with this motivation that the research reported herein was initiated. The primary objective was to develop N^{15} targets satisfactory for the elastic scattering experiment and to then perform this experiment, deducing from the results as much as possible about the various nuclear parameters of O^{16}.

II. PREPARATION OF NITROGEN TARGETS

1. General discussion of elastic scattering targets.

A target satisfactory for an elastic scattering experiment should meet two requirements: (1) it should not deteriorate rapidly under bombardment by reasonable proton beams (about 0.5 microampere per mm^2) and (2) it should contain relatively few atoms of substances with atomic weights greater than the nuclei from which the scattering is to be studied. The demand for reasonable target stability is obvious, so the second requirement will now be discussed.

An incident particle with energy E_1 and mass M_1 which is elastically scattered through a laboratory angle θ_L from a target nucleus of mass M_0 has energy E_2 which can be calculated according to classical kinematics:

$$E_2 = E_1 \left\{ \frac{M_1 \cos\theta_L}{M_0+M_1} \pm \left[\frac{M_1^2 \cos^2\theta_L}{(M_0+M_1)^2} + \frac{M_0-M_1}{M_0+M_1} \right]^{\frac{1}{2}} \right\}^2 \qquad (1)$$

This expression for E_2 is double-valued only if $M_0 \leq M_1$. If $M_0 > M_1$, then only the positive sign is to be taken. For the case $M_0 > M_1$, the partial derivative of E_2 with respect to M_0 is shown in Appendix I, Part 1, to be always greater than zero. Therefore, for a given incident energy and scattering angle, E_2 from a heavy nucleus is larger than E_2 from a light nucleus. If the target is thick and has a large number of nuclei heavier than the one under investigation, the incident beam of particles loses energy in passing beneath the target surface, allowing scattering to take place at energies smaller than the incident energy. This permits an incident particle to be

scattered from a heavy nucleus beneath the target surface and then to emerge from the target with energy and direction identical to that of a particle scattered from a lighter nucleus on the surface. Particle detection equipment cannot differentiate between the particles from the two types of scattering, resulting in an unavoidable yet significant background if heavier nuclei are present in large numbers in an elastic scattering target.

In general, the problem posed by the heavy nuclei may be solved in two ways. One may either prepare a target completely free of heavy material, or one may confine the heavier nuclei to a thin layer. The thin layer, moreover, may be either an unsupported foil or may be supported on a thick backing of lighter nuclei. The choice of technique depends on the particular situation. In the case of the present work, the objective was the preparation of N^{15} targets for a study of the elastic scattering of protons with incident energies less than 1800 kev and for scattering angles at least as small as 90^{o}.

2. General discussion of N^{15} targets.

The study (7, 8, 9, 10) of the elastic scattering of protons from N^{14} has shown that nitrogen gas, beryllium nitride, boron nitride, and adenine ($C_5H_5N_5$) are reasonably satisfactory nitrogen target materials, that frozen ammonia and melamine ($C_3H_6N_6$) are of some value but not entirely satisfactory, and that lithium nitride is of no value at all. This information served as the starting point for preparing N^{15} targets.

The natural abundance of N^{15} is 0.38%, so considerable

enrichment is necessary in order to make a practical target. At the time this research began*, the only commercially available enriched N^{15} was prepared by the Eastman Kodak Company, the maximum enrichment being about 60%. It was available in several chemical compounds and could, of course, have been converted into almost any other compound desired. A possible method of N^{15} target preparation would have been to make beryllium nitride, for instance, in which 60% of the nitrogen was N^{15}.

There are difficulties involved with this approach, however. For scattering angles of 100° or smaller, the over-all energy resolution of the experimental apparatus available is not good enough to completely resolve protons scattered by N^{15} from those scattered by N^{14}. It is possible in principle to subtract out the effect of the N^{14}, but this process depends upon accurate knowledge of density fluctuations of the nitrogen since N^{15} nuclei responsible for scattered particles of energy E_2 lie slightly deeper in the target than the N^{14} nuclei responsible for particles of the same energy. An illustration of the possible magnitude of this density problem is given in figure 1 which is a momentum profile of the elastically scattered protons from a clean beryllium disk that had been heated to about 900° C in the presence of anhydrous ammonia. The natural N^{15} abundance was present in this ammonia. A mixture of 60% N^{15} in a target such as this would provide a momentum profile which would be exceedingly difficult to interpret. A secondary problem, more or less accidental in origin, is that both N^{14} and

---

*Two years later (1956) the Isomet Corporation of Palisades Park, New Jersey, put on sale 95% enriched N^{15}.

N^{15} exhibit energy levels excited by protons of about 1050 kev energy. To subtract out these effects correctly would also be difficult.

Use of a gas target enriched to 60% in N^{15} would avoid the problem of density fluctuations, but other difficulties made this solution unattractive. A gas target could be either a differentially pumped chamber or a closed cell with a thin foil through which the beam enters. In the gas cell arrangement, the straggling of the incident beam resulting from its passing through the foil unavoidably introduces rather poor energy resolution for the experiment. Use of a differentially pumped chamber overcomes the loss of resolution, but nitrogen enriched in N^{15} is sufficiently expensive to make advisable a reclaiming system for the gas pumped out of the chamber. This gas would be contaminated by normal outgassing and incidental leaks. A filtering system could remove most contaminants, but the N^{14} added in this way would be inseparable. Knowledge of the ratio of N^{14} to N^{15} would be necessary at all times, and determining this ratio would require fairly complicated apparatus. Since none of this equipment (i.e. the differentially pumped chamber, the gas reclamation and purification system, and the isotope ratio measuring device) existed in the laboratory at the time, it was decided to restrict research to solid targets.

A further motivation to prepare more highly enriched N^{15} targets lay in the fact that such targets could be used in other experiments. At the time, the $N^{15}(dp)N^{16*}$ reaction had been done with 60% enriched N^{15} targets, and proton groups from $N^{14}(dp)N^{15*}$ were complicating the interpretation. Moreover, the techniques

developed for the N^{15} targets might well apply to preparing targets of other elements.

Therefore, after investigating the known methods for isotope enrichment, it was decided that the most feasible approach was by means of an electromagnetic isotope separator. This method affords relatively high enrichment in one step, and there is no difficulty associated with producing enough of the separated isotope to be useful in a nuclear physics experiment.

3. The isotope separator

An isotope separator has five main components: the ion source, the focusing and accelerating system, the mass analyzer, the collection chamber and the vacuum pumps. The components of the isotope separator to be described here are in some cases not of the optimum design, having been used for the sake of expediency since they were readily available or easily built. Suggestions for improvement will be made.

The ion source used was of the general type described by Thoneman et al. (11) and is illustrated in figure 2. A radio-frequency field of about 40 megacycles ionizes the gas in a pyrex vessel, and the ions are then extracted by a D.C. potential of 3000-4000 volts applied between a tungsten probe sealed in the top of the pyrex and the aluminum canal at the bottom. A coil provides a D.C. axial magnetic field of about 200 gauss near the canal. The available R-F power was estimated to be 400 watts, but no measurements of the power actually dissipated in the gas were ever attempted.

The gas flow to the ion source was controlled by a needle valve, Type 24-101A, manufactured by the Consolidated Engineering Company of Pasadena, California. A gas-tight enclosing jacket and worm-gear reduction assembly modified the needle valve for this particular application. While the isotope separator was in operation, the needle valve was at a D.C. potential of approximately 20 kilovolts, so adjustments in the gas flow were made by means of a lucite control rod that operated the worm-gear reduction assembly.

Obviously the versatility of the isotope separator was limited by the use of this type of ion source. If a metal were vaporized to provide gas for the discharge, some of the metal would condense on the walls of the pyrex vessel, thereby shielding the discharge from the external R-F field. From the point of view of N^{15} targets, this problem does not arise, and R-F ion sources actually have some very favorable features. They are quite stable and will operate for hours with no adjustment. This feature is of particular importance in an isotope separator, as is also the fact that R-F sources are economical in the use of gas. In addition, inherent simplicity of construction reduces the maintenance problem to a minumum and virtually eliminates leaks through the ion source housing from the surrounding atmosphere. Very intense beams are also possible; although this feature was never stressed in the present work, 0.8 milliamperes of hydrogen current was focused in a spot 5/16" in diameter at a distance of 14" from the ion source canal, the diameter of which was 0.060".

•Several gases have been used to provide ions. In addition to hydrogen, successful operation has been obtained with helium, nitrogen, oxygen, ammonia, neon, argon, and air. Complete quantitative measures were not made, but the trend is toward smaller maximum output for the heavier ions, the maximum neon current being about 0.2 milliamperes. A significant characteristic of the ion source was observed in connection with these various gases. Although reasonably efficient in the production of atomic hydrogen ions (approximately 60°/o mass 1, 25°/o mass 2, and 15°/o mass 3), this particular ion source produced only about 10°/o of the total current as atomic nitrogen or oxygen, almost all of the rest being the two-atom molecular ion. This effect is probably a result of higher dissociation energies for N_2 and O_2 and lower ion mobility for these heavier ions. Table I lists ionization potentials and dissociation energies for some of these gases.

TABLE I

Gas	Dissociation Energy (ev)	First Ionization Potential (ev)
H	----	13.53
H_2	4.78	15.6
N	----	14.48
N_2	7.38	15.51
O	----	13.55
O_2	5.08	12.5
NH_3	----	11.2

When the source was operated on NH_3, the ion beams N^+, NH^+, NH_2^+, NH_3^+, and NH_4^+ were all produced. In general, an isotope separator ion source should produce predominately one kind of ion from a given gas, for the sake of efficiency, and there is less difficulty in getting good separation from the adjacent masses if this ion is light. In view of these requirements, an R-F ion source is probably not the most desirable type for a multipurpose isotope separator. However its favorable features would appear to make it valuable for special applications.

The focusing and accelerating system of the isotope separator being described is illustrated in figure 2. A cylindrical electrode 1" in diameter was machined with a truncated cone at the top. The hole in the top was 5/16" in diameter. The top of the electrode was 5/32" from the bottom of the ion source canal which also opened out to 5/16" diameter. Microy supports insulated the electrode from the ion source. The focusing voltage was supplied by a Model PS-30 power supply manufactured by the Condenser Products Company of New Haven, Connecticut. This power supply is rated for 1% ripple at 1.0 milliampere and 30 kilovolts and was operated with a variac to provide variable voltage.

Since only this single electrode was used, the final energy of the ion beam was determined by the focusing requirements rather than by optimizing the collection of the separated isotope. In addition, a small change of focus was accompanied by a change of energy sufficient to move the ion beam from one spot on the collector to another, unless the analyzing magnet was changed

simultaneously. Use of several accelerating electrodes would provide both better focusing and the ability to vary the beam energy over a much larger range than was possible with this apparatus.

It would be desirable to be able to vary the beam energy over a large range. Operation at 3 to 5 kev enables the preparation of very thin targets of a particular isotope. Targets approximately one-half kev thick to one Mev protons can be produced at this energy, and the target thickness instead of the particle spectrometer would then determine the energy resolution. If, for example, one wished to make a detailed study of the elastic scattering of protons from C^{13} near the N^{14} energy level that is excited by 1747-kev protons incident on C^{13}, the only way to avoid making resolution corrections (12) of really large proportions, using the best particle spectrometers available today, is to use a very thin target. This level has a total width less than 0.4 kev (13), and the best spectrometer energy resolution, defined as $E/\Delta E$, available is about 500, making ΔE 3 kev. With this resolution, the size of the observed anomaly due to this resonance would be reduced by at least a factor of 2 or 3 from the size theoretically predicted (see figure 6, reference 10). A less extreme but still important example is the scattering anomaly due to the energy level in O^{15} which is excited by 1737-kev protons on N^{14}. The size of the anomaly at a scattering angle of 160° reported in reference 10 is 1.6 times that shown in reference 8. All of this difference has been attributed to resolution effects.

Limitations on the minimum practical operating voltage for an isotope separator exist, however. One such limitation may be seen by considering the path of a charged particle through a magnetic field. The non-relativistic expression relating the accelerating voltage V, the radius of curvature of the equilibrium orbit r_o (the equilibrium orbit is of significance in the case of non-uniform field analyzing magnets), the ion charge Ze and mass M, and the magnetic field at the equilibrium orbit B_o is

$$2VM = Ze\, r_o^2 B_o^2 \tag{2}$$

From equation 2 result directly

$$\frac{\Delta V}{V} = 2\,\frac{\Delta r_o}{r_o} \tag{3a}$$

$$\frac{\Delta M}{M} = 2\,\frac{\Delta r_o}{r_o} \tag{3b}$$

$$\frac{\Delta V}{V} = -\,\frac{\Delta M}{M} \tag{3c}$$

$$\frac{\Delta B_o}{B_o} = -\,\frac{\Delta r_o}{r_o} \tag{3d}$$

Equations 3a and 3c imply a lower limit for the operating voltage in terms of the total voltage spread, the masses to be separated, the radius of curvature, and the distance desired on the collector between the separated isotopes. For example, if ΔVZe were 0.15 kev and VZe were 3 kev, the isotope separator would not completely separate the ions $(N^{14}N^{15})^+$ and $(N^{15}N^{15})^+$. If ΔV is considered

fixed, a larger minimum value of V is required.

Another factor of considerable importance in establishing the lower limit for the operating voltage is space charge spreading of the beam. This effect increases as the transit time and intensity of the beam increase. As an example of the magnitudes involved, consider a beam of rectangular cross section 0.5 cm high and of small width with an energy of 20 Kev and an intensity of 250 microamperes. If this beam is composed of single-charged particles, the mass of which is 50 atomic mass units, it will be 0.85 cm high after traveling 65 cm if there are no compensating mechanisms (14, 15) tending to neutralize the charge of the beam.

An alternative solution for achieving the low beam energies sometimes desirable is to devise the collection chamber so that the ion beam may be electrostatically decelerated immediately before the ions strike the collector. The advantages of operating the isotope separator at moderately high voltages are then retained, but this technique requires a much more complex collection chamber. The insulation of the collection chamber must be capable of withstanding many kilovolts, the charge of the ion beam striking the collector must be metered and accurately integrated while the collector is many kilovolts above ground potential, signals from the ion beam when it shifts position slightly must be relayed to ground potential for feed-back regulation of the acceleration voltage, and so forth.

Yet another technique for preparing very thin targets is possible, in addition to actually creating a low-energy beam.

When the incident ion beam strikes the collector surface normally, a target of thickness designated by t is produced. However, if the target is turned so that the normal to the target surface is at an angle α with respect to the beam axis, the ion beam penetrates only a distance t cos α beneath the target surface. This method provides a target of thickness t cos α if it then is studied with the incident proton beam striking the surface normally. Small angle scattering of the ion beam puts a practical limit to the size of the angle α feasible, and care must be exercised to prevent this scattered beam from striking surfaces not connected electrically to the target because of the secondary electron emission problem. However, N^{15} targets approximately one-third "normal" thickness have been produced using this technique, and it is reasonable to assume that at least this factor of three would be applicable to most types of targets.

As a general rule, high voltages are desirable for the production of relatively thick targets of materials which have high (10^{-4} mm or greater) vapor pressures at room temperature. In such cases, the only known practical way to collect the isotope after separation is by occlusion in or chemical combination with a substance which does not have high vapor pressure. Neon, for instance, was driven into a tungsten plate at an energy of 20 kev during the course of this work and was observed to stay for several weeks. An example of chemical combination is the case of nitrogen collected in beryllium, to be discussed in detail later. The maximum thickness of backing material in which the separated

nuclei can occur is the range of the incident ion beam in the backing material. The work of Evans et al. (16) indicates that the stopping cross section for heavy ions in this low energy region is very nearly a constant, making the ion range proportional to its energy. In the cases of both occlusion and chemical binding, the ratio of separated nuclei to backing nuclei per unit volume has a maximum value. The only way to increase the total number of separated nuclei in the target is to increase the volume of backing material exposed to the ion beam.

One way to do this is to go deeper into the collector with a beam of higher energy. A second technique which will accomplish the same result, at least in principle, is the slow evaporation of the backing material at the same time the beam is collected, continuously exposing newly evaporated atoms to the incident ion beam. Such a technique, incidentally, has the advantage that the number of separated nuclei in the target (i.e. the target thickness) is unlimited. A possible disadvantage is that the rate of evaporation would have to be controlled to an extreme degree if the finished target is to be uniform in the density of the separated nuclei. But regardless of what technique is employed, it is obvious that an isotope separator becomes more useful as the range of available target thicknesses increases.

As an example to give an idea of the voltages necessary to produce a target of a given thickness, the N^{14} atom at an energy of 10 kev has a range in beryllium about equal to the distance in which one Mev protons would lose 1.5 kev. But it should be noted

that while the range of a heavy ion of low energy in a given material is about proportional to its energy, this constant of proportionality in turn depends upon the type of ion and type of material. Only approximate estimates are available for most combinations of ions and backing substances.

A 90^{o} uniform-field 12" radius magnet is used as the mass analyzer for the isotope separator being described. This magnet had been built for another purpose and was not particularly suited to this application since the pole pieces were only 13/32" apart and 1" wide. Three six-volt automobile batteries in series provided, with a rheostat, a stable, variable current supply for the magnet which required about 3.0 amperes to bend 20 kev $(N_{15}N_{15})^{+}$ ions. A potentiometer and shunt arrangement was used to measure accurately the magnet current fluctuations, but hysteresis effects are large enough to make necessary a flux measuring instrument. Because of the lack of a fluxmeter and the inability to alter the accelerating voltage without changing the focus (and therefore change the ion current), a precise measure of the separating power of this particular apparatus was difficult to obtain. An indication of this quantity may be obtained from figure 3, which is a plot of the ion current collected on a 1/8" high target with the accelerating voltage fixed as the magnet current was increased. The ion source was being supplied with a mixture of nitrogen, hydrogen, and ammonia in an effort to get measurable currents of integral mass numbers near mass-30. This attempt was not entirely successful. The loss of resolution from the finite width of the collector can be

estimated from the quantity ΔI noted in figure 3. This quantity is the change in magnet current required to move ions with a given initial energy and direction from the bottom of the 1/8" high collector to the top. The quantity ΔI is calculated from equation 3d and the additional assumption that the magnetic field is proportional to the magnet current. The total width at 5% of the maximum ordinate associated with each mass is approximately twice ΔI. This extra width is due predominately to voltage ripple in the accelerating power supply, energy spread of the beam as it leaves the ion source, and angular spread as the beam enters the magnet. The extent of the inhomogeneities of the magnetic field from the inner to outer radii of the pole pieces is not known. The effects from the finite width of the incoming beam disappear to first order for a 90° magnet.

Certain features of the magnet used in the isotope separator being described here could be improved. A larger vacuum chamber within the magnetic field than was available in these experiments is almost a necessity so that several isotopes of adjacent mass numbers may be collected at the same time. As mentioned above, a flux measuring device should certainly be incorporated, and a larger radius of curvature would provide greater separating power. But beyond that, one can choose from a wide range of types. Successful isotope separators have been built with magnets of 60°, 90°, and 180° with uniform fields and with focusing fields. No single type appears to be overwhelmingly superior.

The collection chamber of the isotope separator used in

these experiments was rebuilt several times but was never considered to be a complete success. Because the magnet and its supporting structure were of an awkward design, space was extremely limited in the region where the beam came out of the magnet. The most recently designed chamber was made from a 1/8" wall brass cylinder $3\frac{1}{2}$" in diameter and 5" long. A section view of this is shown in figure 4. A brass plate was soldered in one end, and the other end was soldered to a ring that sealed on an O-ring in the housing at the end of the magnet vacuum chamber. Ten glass-to-metal insulated terminals were soldered in the housing and chamber, into which were waxed two 1-3/4" diameter glass windows. Two spring-loaded levers which were operated through sylphon bellows and one port into which was O-ring sealed the collector assembly were also available. The collector assembly was electrically insulated from the collection chamber by means of a lucite fitting. A 3/4" diameter brass rod sealed on an O-ring in this lucite fitting and could slide back and forth in the horizontal direction over $1\frac{1}{2}$". A 1/8" hole was bored in the 3/4" rod 9/32" off center but parallel to its axis, and a 1/8" diameter rod was O-ring sealed in this hole. The actual collector was fastened to the 1/8" rod, so that by the rotation and sliding of the 3/4" rod, a point on the collector could be moved vertically through 9/16" and horizontally through $1\frac{1}{2}$". The plane of the collector could be adjusted to any angle by rotation of the 1/8" rod with respect to the 3/4" rod. It was thus possible to adjust the collector position so that the beam deposited the desired isotope in the desired

location. The collector assembly was insulated so that the incident beam could be metered and the charge integrated if desired.

In order to meter all of the charge from the incident beam, lose none of the secondary electrons knocked out of the collector, and gain none of the secondary electrons knocked out elsewhere by stray beam, the target was maintained at +300 volts with respect to the chamber walls and a ring was maintained at -300 volts between the collector and the beam-size defining diaphragm. This diaphragm was a solid disk 2" in diameter and had a 5/16" diameter hole in it. It was mounted on one of the spring-loaded levers. Proper alignment allowed the beam to pass through the hole to the collector, while moving the diaphragm horizontally permitted the complete shielding of the collector from the beam. Insulation of the diaphragm enabled metering of the charge that was collected there, which in turn required +300 volts on the diaphragm and -300 volts on a ring between the diaphragm and the second movable lever. This lever supported an insulated beam catcher that was 1/8" high and which could be moved up to intercept a section of the beam in order to investigate its density in different regions. This narrow collector was run at +300 volts and a third electron suppressor ring at -300 volts was placed between it and the magnet vacuum chamber.

Other features of the collection chamber were high-current, water-cooled terminals for a furnace in which beryllium was readily evaporated, water-cooled walls near the furnace (the furnace was 1/4" from the wall so that it didn't interfere with the passage of the ion beam), and an ionization gauge for measuring

the pressure. The lowest pressure achieved was 10^{-6} mm with the furnace cold, and it was generally about 4×10^{-6} mm while evaporating beryllium.

Several additions and improvements have appeared desirable. For one, an air-lock should be provided so that the collector assembly can be removed without bringing the entire system up to atmospheric pressure. Another suggestion that should be investigated is the introduction of a "getter" to improve the vacuum in the vicinity of the collector. The desirability of a better vacuum will be discussed in the following section in which will be given detailed analyses of the nitrogen targets prepared. More effective shielding of the many electrically insulated components in the collection chamber from the furnace is also necessary. Since fractions of microamperes of beam current are to be collected on occasion, and because the collectors are at a 300 volt potential with respect to ground, the insulating supports should have resistance of 10^8 ohms or more. The fact that the vaporized atoms of some metals, beryllium for one, do not all stick the first time they impinge on a solid surface introduces the requirement for quite intricate shielding if evaporation is to be done in the collection chamber, all the time maintaining the 10^8 ohm resistances. Moreover, provision should be made for a pair of "regulator electrodes" which can be used to provide signals from a small portion of one of the separated beams for a feedback regulation of the beam position. These electrodes should be movable without destroying the vacuum since regulation would be done sometimes on the isotope of interest

and sometimes on a component several mass units lighter or heavier. An additional need is a safety system to prevent contamination in the event of a spark or momentary power failure. And finally, the utmost care in design should be exercised, attempting to construct the entire collection chamber from materials that outgas as little as possible. In particular, the use of O-rings should be minimized, if not eliminated, since a collection chamber free from hydrocarbons is extremely important in the preparation of pure targets.

The vacuum pumps, of course, are fundamentally related to this problem. Two oil diffusion pumps were used in the apparatus being described. An 8" pump connected near the ion source and a 4" pump connected near the collection chamber. Each of these pumps had a cold trap which was kept at dry ice temperatures while targets were being made, and a large liquid air cold trap was suspended about 6" from the collector assembly. Had sufficient space been available, an additional liquid air cold trap would have been installed closer to the collector. Because of the great importance of maintaining a clean system, it would probably be advisable in any future design to incorporate a refrigeration unit to provide continuously cooled traps for the pumps.

4. Nitrogen targets prepared with the isotope separator

In the preparation of nitrogen targets for elastic scattering with the isotope separator, the two-atom molecular ion beam was collected in either beryllium or graphite. Focusing occurred at an accelerating voltage of about 20 kilovolts, and, as explained

in the preceding section, operation was therefore limited to beams of around 20 kev. Polished beryllium disks were used as collectors in the first attempts at target preparation. These disks were cut to be about 1/16" thick from a 3/8" diameter beryllium rod. Carborundum sandpaper was used for the initial smoothing and polishing, and an iron oxide polishing paper was used for the final polishing. Despite extreme care in the polishing process, significant traces of carbon and oxygen, presumably worked into the surface from the polishing papers, were always present in the surface of the beryllium. Momentum analysis of protons elastically scattered from the beryllium provided a measure of this contamination. Figure 5 shows a typical momentum analysis, although the data displayed in this figure are from an N^{14} target made on evaporated beryllium. Had the surface been polished, the carbon and oxygen peaks would have been about twice as high relative to the nitrogen. Since complete resolution between an N^{15} peak and an O^{16} peak would not be possible at smaller scattering angles (see figure 6 for an example of several angles), minimizing the oxygen contamination on these nitrogen targets was of great importance. For this reason, the evaporation of a beryllium backing immediately before collection of the nitrogen was attempted.

The necessary thickness of the evaporated beryllium was determined by the atomic weight of the material onto which the beryllium was evaporated. As was shown in a previous section, a heavier atom provides elastically scattered particles of a higher energy for a given incident energy and scattering angle than does

a lighter one. Therefore the beryllium layer had to be thick enough to reduce the energy of the protons scattered from the backing material so that they would be of lower energy than the protons scattered from the nitrogen in the outer surface of the beryllium. Steel, quartz and beryllium were tried as backings for the evaporated beryllium. The beryllium thickness required for steel and quartz backings proved to be difficult to obtain. The beryllium layer developed greater and greater internal stresses as it got thicker. Much of the time these stresses induced the pulling away of the beryllium from the backing and the subsequent shattering of the foil as it continued to spring loose from the supporting material. A second problem was due to space limitations. The collector was about 3" from the furnace and adequate cooling was difficult. Frequently during the long evaporations necessary, the collected beryllium became so hot that it was oxidized by the oxygen remaining at a pressure of 4×10^{-6} mm. This oxidation process could be followed visually as the appearance and intensification of a hazy appearance on the collector surface, which would have been an excellent mirror if it had been pure beryllium. This haziness was shown to be an oxygen contamination by elastic scattering analysis. Evaporation for several periods of shorter duration than required for the heating of the collector was attempted, but the alternate heating and cooling apparently enhanced the internal stresses since the shattering of the beryllium became much more pronounced.

For these reasons, polished beryllium disks were used to collect the evaporated beryllium. The thickness of evaporated

beryllium required in this case was just that necessary to guarantee that the protons scattered from the surface oxygen in the polished beryllium had less energy than the protons scattered from the nitrogen in the evaporated surface. Figure 5 is a momentum profile of an N^{14} target collected in an evaporated beryllium surface. Significant carbon and oxygen contaminations still are apparent. Less than half of this oxygen contamination can be traced to the beryllium itself, but it is true that in the course of this research, elastic scattering analyses of even freshly evaporated beryllium have never demonstrated a beryllium surface to be completely free from oxygen. Presumably oxygen captured from the atmosphere by a few of the surface atoms of the beryllium accounts for this phenomenon, but no convincing proof of this hypothesis was obtained.

Information about the origin of the remainder of the oxygen contamination apparent in figure 5 was obtained, however. Figure 7 gives the results of the following experiment. After several attempts that failed, a polished steel surface $1\frac{1}{2}'' \times \frac{1}{2}''$ had enough beryllium evaporated on it to permit an elastic scattering analysis of the nitrogen and oxygen content. The beryllium coated iron was exposed, in differing locations, to different amounts of the N^{14} beam from the isotope separator. The pressure in the collection chamber, the adjustment of the ion source, and all other observed quantities were the same for each of the different targets, which were prepared one after another. The order of preparation, in terms of the microcoulombs of mass-28-beam collected, was 3750, 30000, 7500, 22500, and 15000. Momentum

analyses were then performed on the various targets, and the values of the peaks corresponding to N^{14} and O^{16} are plotted in figure 7. The non-zero intercept of the O^{16} curve has been discussed above. The subsequent increase of O^{16} is consistent with ionization of the beryllium surface by the incident ion beam causing this particular area of beryllium to act as a getter for the residual oxygen. No other reasonable mechanism for this oxygen build-up has been suggested.

Also of significance in figure 7 is the apparent saturation of the beryllium with nitrogen after collection of about 7500 microcoulombs of beam. A measurement of the spot into which nitrogen was driven enabled calculation of the N^{14} atom density, which was found to be about 3×10^{17} atoms per cm^2. It has been experimentally determined that one Mev protons lose around 2.7 kev in passing through the region in which N^{14} is located in targets prepared in this fashion. Calculations using the best available estimate of the proton stopping cross section per nitrogen atom of beryllium nitride (17) indicate that beryllium nitride containing this quantity of nitrogen would cause one Mev protons to lose 3.3 kev. In view of the facts that the charge collection system was not accurately calibrated, that the exact point of saturation cannot be determined from figure 7, that an accurate measure of the area of N^{14} content is difficult, and that there is no a priori guarantee that the "sticking probability" of an incident nitrogen atom is unity, the agreement of these two numbers is felt to be consistent with the hypothesis that all of the nitrogen was chemically bound to the beryllium in the form of Be_3N_2. Also consistent with this hypothesis is the

observation that the nitrogen content of such targets has been observed to change neither under bombardment by several microamperes of proton beam nor at temperatures in excess of 400° C. Beryllium nitride is stable at temperatures in excess of 2200° C while an occluded gas would rapidly diffuse out at 200° C, according to the work of Thulin (18). Moreover, by making estimates (by interpolating and extrapolating the data of Evans et al. (16)) of the range of nitrogen ions in beryllium, the number of beryllium atoms per cm^2 that 10 kev nitrogen ions should pass before stopping is 4×10^{17}. Assuming 3×10^{17} nitrogen atoms per cm^2 which are all bound as Be_3N_2 requires 4.5×10^{17} beryllium atoms per cm^2.

Such N^{14} targets have two primary disadvantages, then. They have significant amounts of C^{12} and O^{16} in addition to the N^{14}, and the exact number of N^{14} atoms is not known. Even so, considerable use (10) was made of this type of target. The oxygen contamination appeared to be too large for satisfactory N^{15} targets, however. As a result, graphite was investigated as a possible backing. The first technique attempted was the use of carbon foils prepared in the way described by Seagrave (19), incorporating the modifications of Milne (20). Each foil was glued over a hole in a piece of tantalum, and the N^{15} was collected in the region over the hole. A factor of two or three improvement in the ratio of N^{15} to O^{16} was achieved with this method, but the foils would not withstand the prolonged proton bombardment required. They

cracked, curled up, and pieces sometimes fell out. When different foil thicknesses all displayed the same behavior, the use of 1/16" thick graphite disks was investigated. These disks were machined from a graphite rod and were polished in the same way as the beryllium. In view of the grainy texture of the graphite, it polished remarkably well, appearing to the eye to be as smooth as the beryllium. The surface oxygen problem was again present, as can be seen from the top profile of figure 8. However, this oxygen could be driven out of the graphite by heating it in vacuum to a yellow-orange color. (This process did not remove oxygen when attempted with beryllium.) The middle profile of figure 8 illustrates the oxygen-free graphite. The bottom profile of figure 8 illustrates the composition of a typical N^{15} target in a graphite backing. As in the beryllium-backed N^{14} targets, O^{16} was picked up during the collection of the nitrogen. But upon saturation of the carbon with nitrogen, the N^{15} to O^{16} ratio was somewhat better than with the beryllium backed targets. However, the subsequent heating in a vacuum of the N^{15}-containing graphite to an estimated temperature of 500° C drove off more than half of the O^{16} present with but a small effect on the N^{15} content. Further heating at this temperature accomplished nothing, and increasing the temperature reduced the N^{15} content appreciably. This technique produced targets with four times less oxygen on them than on the beryllium backed ones, but the saturation quantity of N^{15} in graphite is about 1.5×10^{17} atoms per cm^2 or half of what it is in beryllium for incident 10-kev nitrogen atoms.

As a result, there were approximately eight times as many N^{15} atoms as O^{16} atoms. Such targets were usable for the elastic scattering experiment, but less contamination by oxygen would have been helpful. No further experiments on the preparation of targets for elastic scattering have been carried out, however, since arriving at the point of making targets that were usable.

The stability of the graphite-backed N^{15} targets was not as good as that of beryllium backed targets, but the loss of N^{15} was small enough under bombardment by a microampere of protons so that it was quite difficult to measure. Indications are that losses of 2 - 4% probably occurred during 4 - 5 hours of bombardment. Occlusion of nitrogen by the carbon could not explain this stability in view of the rapid loss of occluded gases reported by Thulin (18). Oxygen, when accelerated by the isotope separator and collected in carbon, disappeared quite rapidly, under proton bombardment, a behavior certainly consistent with occlusion of either oxygen gas or a gaseous carbon-oxygen compound. That nitrogen collected in graphite is much more stable than would be otherwise expected leads to the suggestion that there exists a carbon-nitrogen compound that is stable and which has a fairly low vapor pressure at temperatures at least as high as 400° C. As was the case for beryllium backings, the graphite ultimately becomes saturated with the nitrogen. Approximately one-half as many atoms are required to saturate the graphite as were necessary for the beryllium, which suggests there are two or three carbon atoms per nitrogen atom in the assumed carbon-nitrogen compound. Chemists agree that such a compound exists, but its

chemistry is not understood (21).

Targets containing N^{15} for other types of experiments have also been prepared. Beryllium foils which were 25 kev thick to one Mev protons produced excellent N^{15} targets for a study (5) of the long range alpha particles from the reaction $N^{15}(p\alpha_0)C^{12}$. The short range alpha particles from $N^{15}(p\alpha_1\gamma)C^{12}$ have been studied (and will be discussed in greater detail in a following section of this paper) at various energies and angles with targets made by collecting N^{15} in 200 microgram per cm^2 aluminum leaf. The stripping reaction $N^{15}(dp)N^{16}$ has been studied (22) using N^{15} embedded in an unsupported 1000$\mathring{A}$ nickel foil.

Attempts to prepare N^{15} targets that have failed were generally unsuccessful because of unsatisfactory collectors. Gold and silver leaf of about 200 micrograms per cm^2 have not proved satisfactory. The metal seems to disappear from the reasonably well defined region where the nitrogen beam is collected, ultimately leaving a hole where the beam was most intense and then trailing off through translucency to the opacity of the undamaged leaf. Also, on several occasions when nickel foils were being used as collectors, the foils have pulled partially away from the mounting frames. Approximately the same nitrogen beam current was used for most targets prepared, and in every instance in which the nickel foil was not in good thermal contact with its supporting frame, essentially no nitrogen was found in the foil upon subsequent analysis. On the other hand, the three nickel foils that did remain in contact with the frames each had the expected N^{15} content.

Nickel nitride (Ni_3N_2) is a known but uncommon chemical compound and is supposed to decompose at a temperature of a few hundred degrees. Apparently in the cases where the nickel foils have not been in good thermal contact with the supporting frames, the bombardment by the nitrogen beam has raised the nickel to temperatures higher than are stable for nickel nitride.

The possibility of using nickel or some other heavy material for foils in which to collect N^{15} for elastic scattering targets was investigated, and no improvement in the N^{15} to O^{16} ratio was observed. An additional problem was apparent in the case of these heavier backing materials in that the momentum spectrum of the protons elastically scattered from the foil was not rectangular but had a tail off towards the low-momentum side caused by straggling and by scattering from the walls of the spectrometer. The N^{15} peak appeared superposed on this tail, and as the scattering angle was decreased, the N^{15} peak moved up the tail toward the peak due to the heavy atoms. Such targets would have been satisfactory for elastic scattering only at large angles and high incident energies.

That the elastic scattering was not studied in the present work below 600 kev incident proton energy is a limitation imposed by the targets that were produced. As is indicated above, the N^{15} is distributed in the top layer of the graphite. This layer becomes thicker in terms of energy lost by the incident protons as the incident energy is decreased. When the energy lost in traversing the region in which the N^{15} is located becomes about half of the energy

difference between protons scattered from N^{15} and C^{12}, it is no longer possible to resolve all of the protons scattered by N^{15} from those scattered by C^{12}. This mixing is a fundamental limitation of the target and appears around 650 kev at a scattering angle of 90^{o}. A backing material with smaller atomic weight is necessary to avoid this difficulty. The most promising approach appears to be the use of beryllium backings, but the use of beryllium requires a reduction of the oxygen contamination, as has been previously discussed.

A further aspect of preparing N^{15} targets with the isotope separator is the gas supply for the ion source. Experiments with ammonia indicated that significant contamination between ions $(N^{15}H_n)^+$ and $(N^{14}H_{n+1})^+$ distinctly excluded this gas as a possibility. Subsequent work has indicated that the presence of either water or hydrogen provides enough of this isotopic mixing to be troublesome. The obvious solution is to use pure nitrogen. Because the relatively wide peaks seen in figure 3 cause a mixing of N^{14} and N^{15}, a reasonably high percentage of N^{15} was desirable to begin with.

For this reason, NH_4NO_3 with 63% of the nitrogen in the ammonia radical as N^{15} was used to prepare the nitrogen for the ion source. The NH_4NO_3 was mixed with an excess of previously dried CaO as the first step of this preparation. Ammonia was evolved along with water when this mixture was heated in a vacuum, and these two vapors were frozen with liquid air in a separate pyrex vessel that could be isolated from the rest of the

system. Some chips of CuO were in this separate vessel, and after isolation and allowing it to warm up to room temperature, the pyrex vessel was heated with a bunsen burner until all of the ammonia had been reduced to nitrogen and water by the hot CuO. This mixture of nitrogen and water was then diluted by adding about twenty parts of helium (purified by activated charcoal at liquid nitrogen temperatures) to one part of nitrogen. Such a dilution decreased the maximum attainable nitrogen beam by less than 30%, and therefore made the N^{15} target preparation more economical since the amount of enriched NH_4NO_3 necessary to produce one target was reduced by a factor of about fifteen. This mixture was allowed to flow through several turns of copper coil at liquid nitrogen temperature and then to the needle valve that regulated flow into the ion source. When it entered the ion source, it was very nearly a mixture of pure nitrogen and helium.

The gas supply container, the liquid air container, and the condensation coil were all run at the potential of the ion source, about 20 kilovolts above ground. This arrangement permitted the gas pressure to be as low as desired without danger from a breakdown in the gas line. Practically all of the enriched nitrogen gas therefore passed through the ion source.

Utilizing the technique described above, twelve N^{15} targets in graphite backings were prepared. Each of these targets possessed approximately the same characteristics, and through the use of these targets the data to be described in a following section were obtained.

III. APPARATUS AND PROCEDURE FOR THE ELASTIC SCATTERING EXPERIMENT

1. Apparatus

The apparatus used for this study of the elastic scattering of protons by N^{15} has been previously described in detail. A 1.8 Mv electrostatic accelerator (20, 23) provided the proton beam from which was selected a portion homogeneous in energy to within at least 0.1% by an 80° electrostatic analyzer similar in design to that described by Fowler et al. (24). The protons scattered from the target through a given angle and into a certain solid angle entered the magnetic spectrometer (25) which was mounted (26) so as to allow a continuously variable laboratory scattering angle between 0 and 160°. Most of the data for the present experiment were taken with spectrometer momentum resolution (defined as $p/\Delta p$) of about 300 and with an effective spectrometer acceptance solid angle of 3.10×10^{-3} steradians, although a resolution of 600 and solid angles of 1.65×10^{-3} and 0.488×10^{-3} steradians were also available. The scattered protons were detected with a thin cesium iodide crystal and a photomultiplier tube, this arrangement being described in more detail by Mozer (27).

2. Calibration

Calibration of the apparatus described above was accomplished by techniques previously described in detail (27). A gamma ray resonance excited by protons of known incident energy is the basis of the electrostatic analyzer calibration, and the elastic scattering of protons energetically analyzed by the calibrated

analyzer provided protons of known (calculated from equation 1) energy for the magnetic spectrometer calibration. During the experiments being reported here, two different gamma ray resonances were used for calibration: $F^{19}(p\alpha\gamma)O^{16}$ at 873.5 kev (28) and $Al^{27}(p\gamma)Si^{28}$ at 993.3 kev (28). In addition several other $F^{19}(p\alpha\gamma)O^{16}$ states have been intensively studied (29). The 669 kev and 1346 kev resonances in $F^{19}(p\alpha\gamma)O^{16}$ were used in addition to the mass two beam on the 669 and 873.5-kev resonances to check the linearity of the analyzer plate voltage measuring device. The results of this investigation are given in Table II, where C_p times 10^7 multiplies the potentiometer reading, E_p, in millivolts to give the energy of the incident beam in ev.

TABLE II

E_p(mv)	C_p	E_R(kev)	Incident Beam
66.75	1.0040	669.0(F^{19})	Mass one
87.17	1.0031	873.5(F^{19})	Mass one
99.18	1.0017	993.3(Al^{27})	Mass one
133.71	1.0023	669.0(F^{19})	Mass two
134.42	1.0015	1346.0(F^{19})	Mass one
174.58	1.0015	873.5(F^{19})	Mass two

The determination of E_p from the experimental data was possible to within about $\pm 0.05\%$, and the probable errors for the values of E_R are $\pm 0.10\%$ (28, 30). It should be noted that the values obtained from the comparison of mass one and mass two beams

at a given resonance are different and that these differences fit into a systematic decrease of C_p with increasing energy. Therefore, it has been concluded that the voltage measuring device currently installed on this electrostatic analyzer is probably not measuring a quantity exactly proportional to the voltage across the analyzer plates. The deviation, however, is seen to be of almost negligible importance.

3. Thin target procedure

The N^{15} targets described above are thin targets inasmuch as the incident proton beam (over the proton energy range investigated here) lost but a small fraction of its total energy in passing through the entire concentration of N^{15}. The data obtained from these targets were essentially a series of momentum analyses, as in figure 6, at various angles and energies. Such data are related to the differential elastic scattering cross section by the following equation, which is similar to an equation worked out in detail by Snyder et al. (25)

$$\frac{d\sigma}{d\Omega_{c,L}} = \frac{ZeR}{q n_T \Omega_{c,L}} \int \frac{N(I)dI}{I} \qquad (4)$$

In this equation, Ze is the charge of each incident particle, q is the amount of charge collected from the incident beam (note q and Ze are to be expressed in the same units), R is the momentum resolution of the spectrometer (R = 300 generally in this experiment), $\Omega_{C,L}$ is the effective solid angle in steradians of the spectrometer in either the center-of-mass system (C) or in the

laboratory system (L), n_T is the total number of target nuclei per unit area, and the integral is obtained from the momentum spectrum. Since the value of I, the inverse momentum in arbitrary units, changes but slightly over the N^{15} peak, the above integral is very nearly equal to the area under the N^{15} peak divided by I at N_{max}. Hence

$$\int \frac{N(I)dI}{I} \approx \frac{1}{I(N_{max})} \int N(I)\, dI.$$

The procedure followed, therefore, was to take complete momentum profiles at a series of energies and angles, relative to one energy and angle. By taking a complete profile at the reference energy and angle for each new target, a set of values for $\int \frac{N(I)dI}{I}$ was obtained that could be corrected for fluctuations of n_T from one target to another or between two regions of the same target. The ratios of $\int \frac{N(I)dI}{I}$ to N_{max} were then plotted as a function of energy for a given angle and as a function of angle for a given energy. Measuring N_{max} was then enough to obtain (by interpolation from the graphs just described) the value of $\int \frac{N(I)dI}{I}$ at all other energies and angles. By using this technique, relative cross sections for the excitation functions and angular distributions shown in figures 9 to 27 were obtained.

The determination of the absolute value of the cross-section was accomplished by measuring the following set of quantities. One measurement was the evaluation of the expression $\frac{Ze\,R}{q\Omega_{C,L}}$, a second was determining n_T for a particular target, and the third was obtaining a value of $\int \frac{N(I)dI}{I}$ for the target in which n_T was known. The knowledge of these three quantities then enabled calculation

of the absolute differential cross section from equation 4.

The expression $\frac{Ze\,R}{q\Omega_{C,L}}$ was evaluated by measuring the elastic scattering yield with the magnetic spectrometer from freshly evaporated thick copper and assuming this scattering to be exactly equal to that calculated from the Rutherford differential cross section. The thick target yield is related (for details see reference 25) to the cross section as follows:

$$\frac{d\sigma}{d\Omega_{C,L}} = \frac{N_{st}\,Ze\,R\,Y_T}{N_{sc}\,q\,\Omega_{C,L}\,\varepsilon_{20}}\left[\varepsilon_1\left(\frac{\partial E_2}{\partial E_1}\right)+\varepsilon_2\left(\frac{\cos\theta_T}{\cos\theta_T'}\right)\right]\ \frac{cm^2}{steradian} \qquad (5)$$

N_{st} is the number of stopping atoms per unit volume, and N_{sc} is the number of scattering nuclei per unit volume ($N_{st} = N_{sc}$ for copper elastic scattering). The quantity $\frac{Ze\,R}{q\Omega_{C,L}}$ is the same as in equation 4, Y_T is the thick target yield, E_{20} is the energy of the particles accepted by the spectrometer, ε_1 and ε_2 are the stopping cross sections for the incident particles in the scattering material at the energies before and after scattering respectively, $\frac{\partial E_2}{\partial E_1}$ is obtained from equation 1, and θ_T and θ_T' are the angles between the normal to the target and the incident and scattered particles respectively. The customary unit of measure for stopping cross sections is ev-cm^2. If such units are employed and E_{20} is expressed in ev, the differential cross section of equation 5 is in cm^2/steradian.

The Rutherford differential cross section in the center-of-mass system is given by

$$\frac{d\sigma_R}{d\Omega_c} = 1.296\left[\frac{Z_0 Z_1}{E_1 M_0}(M_0+M_1)\csc^2\frac{\theta_c}{2}\right]^2 \times 10^{-27} \frac{cm^2}{steradian} \quad (6)$$

Z_0 and Z_1 are the number of electron charges possessed by the target and incident nuclei respectively, and M_0 and M_1 are their respective masses. The center-of-mass scattering angle is denoted by θ_C, and the incident particle energy E_1 is in Mev in the laboratory system. For the case of elastic scattering, the laboratory scattering angle, θ_L, is related to θ_C by

$$\sin(\theta_c - \theta_L) = \frac{M_1}{M_0}\sin\theta_L \quad (7)$$

The center-of-mass solid angle Ω_C is related to the laboratory solid angle Ω_L for the case of elastic scattering by

$$\frac{\Omega_L}{\Omega_c} = \frac{\sqrt{1-\frac{M_1^2}{M_0^2}\sin^2\theta_L}}{\left[\sqrt{1-\frac{M_1^2}{M_0^2}\sin^2\theta_L} + \frac{M_1}{M_0}\cos\theta_L\right]^2} \quad (8)$$

Therefore, by measuring Y_T, θ_T, and θ_T', using tabulated values of $\mathcal{E}_1$ and $\mathcal{E}_2$, and calculating E_{20}, $\frac{\partial E_2}{\partial E_1}$ and $\frac{d\sigma_R}{d\Omega_{C,L}}$, it was possible to evaluate the quantity $\frac{Ze\,R}{q\Omega_{C,L}}$ for a particular combination of the apparatus constants. This calculation is carried out numerically in Appendix VI.

Using this same combination of apparatus constants, n_T and $\int\frac{N(I)}{I}\,dI$ were evaluated. Because of the method used for preparing the N^{15} targets, neither the total number nor the density distribution of the N^{15} atoms was precisely known. By measuring

the 4.43-Mev gamma ray yield due to the 898-kev $N^{15}(p\alpha_1\gamma)C^{12}$ resonance from a relatively thick target of known composition and then comparing this yield to that obtained from the thin target, the total number of N^{15} atoms per unit area in the thin target can be obtained in terms of the stopping cross section of the semi-thick target material and directly measurable quantities. A semi-thick evaporated layer of KNO_3 enriched to 61% N^{15} was used for this measurement. In Appendix I, part 2, the relationship necessary for determining n_T is derived and is the following:

$$n_T = \frac{A}{(\tan^{-1}x_2 - \tan^{-1}x_1)} \times \frac{2\tan^{-1}\frac{\xi}{\Gamma}}{\epsilon\, Y_{max}} \qquad (9)$$

Here A is the value of $\int Y(E)\,dE$ for the thin target where Y(E) is the resonant yield of the 4.43-Mev gamma ray at the incident proton energy E and where $x_i = \frac{E_i - E_R}{\Gamma/2}$, E_R being the resonance energy and Γ being the total width of the resonance. Y_{max} is the maximum gamma ray yield from the KNO_3 target of ξ thickness in which the stopping cross section in ev-cm^2 per N^{15} nucleus is ϵ. Equation 9 is based on the assumption that the efficiency for counting the gamma rays from the two kinds of targets is the same. This same efficiency was accomplished experimentally by arranging to measure Y(E) for the thin target and Y_{max} for the thick target alternately, and demonstrating reproducability of the results. The value of ξ was obtained from the 4.43-Mev gamma ray excitation function for the KNO_3 target, and the average value from different

targets was such that $\xi/\Gamma \approx 20$, so that $\tan^{-1} \frac{\xi}{\Gamma} \approx \frac{\pi}{2}$. The stopping cross section was calculated from the sums of the stopping cross sections for potassium, nitrogen, and oxygen. By using an estimated value for potassium obtained by interpolating a plot of measured stopping cross sections versus atomic number, the value 55.7×10^{-15} ev-cm^2 per N^{15} nucleus was calculated.

Immediately following the gamma ray measurements, a momentum analysis was performed on the elastically scattered protons from the same thin target for which n_T had been measured. This measurement provided a value of $\int \frac{N(I)dI}{I}$ so that the absolute cross section could be calculated at this particular energy and scattering angle from equation 4. The relative cross sections were then normalized to this value. An example of this calculation is given in Appendix VI.

The KNO_3 targets used for the normalization of the elastic scattering cross section were also used for the investigation of possible gamma radiation resonant near 710 kev. Potassium nitrate enriched to 61% N^{15} was obtained from the Eastman Kodak Company, and after carefully melting the KNO_3 in a tantalum furnace, it was evaporated onto a clean chromium-plated brass blank. Such targets were evaporated in the target chamber of the electrostatic accelerator in order to prevent moisture in the atmosphere from combining with the KNO_3 and changing the stopping cross section. A cooled target holder was built to enable beams up to 1.5 microamperes of proton current per mm^2 to be

used on the KNO_3 held at dry-ice temperatures. No deterioration of the nitrogen yield was observed using this arrangement, but contaminants from the vacuum system were frozen on top of the KNO_3 in spite of a liquid air trap 3" from the target. Corrections for the presence of this contamination were made.

4. Corrections applied to the data

Before actual numerical values of the integral $\int \frac{N(I)dI}{I}$ in equation 4 were obtained from the individual momentum spectra, a correction was made for the non-zero counting rate observed when the spectrometer was set to accept momenta different from those characteristic of elastic protons from carbon, nitrogen or oxygen. The bottom spectrum illustrated in figure 8 shows, for example, that at inverse momenta of 62.0 and 64.0, a few counts were obtained. These counts are caused by protons elastically scattered from a heavy impurity in the graphite. No such background was observed from the carbon foils which were presumably pure carbon. The middle spectrum of figure 8 presents a magnified view of this background from a clean graphite target. A study of the energy and angular variation of this background was made, and then the appropriate subtractions were made both in the evaluation of $\int \frac{N(I)dI}{I}$ and in the determination of the values of the N^{15} peaks for the cases in which complete profiles were not obtained.

A second subtraction was necessary to obtain values of $\int \frac{N(I)dI}{I}$ for scattering angles of less than about 115^{o}. Figure

6 illustrates complete momentum profiles at three different angles, and from this illustration is seen the impossibility of graphically estimating a separation of the contributions from N^{14}, N^{15}, and O^{16} at 90°. By inspection of the 160° data, adequate division of the 125° profile was considered possible, but for smaller scattering angles, the entire area was measured. By combining the knowledge of the target composition obtainable from the 160° profile with knowledge of the N^{14} and O^{16} elastic scattering cross sections, a correction was calculated which was subtracted from the total area. The cross section information for N^{14} was obtained from reference 10 while that for O^{16} was obtained from reference 31, as modified by reference 32 and extrapolated by a method discussed in Appendix II.

A third correction applied to the final relative cross sections was to increase by 3% the measurements at center-of-mass angles of 150° and 160°. A study of the effective solid angle of the spectrometer as a function of scattering angle conducted by Mozer (27) shows that the solid angle is reasonably constant for angles less than 135°, then decreases by 3% between 135° and 150° and remains 3% low out to 160°. This correction is a compensation of this effect.

5. Probable error

The probable error of the cross sections reported here is estimated to be 11% for the absolute value and 6% for relative values for a scattering angle of 160°, going up to 12%

for relative values at an angle of 90°. Uncertainties in the firing voltage of the current integrator (0.5%), measurement of the relative scattering angles (0.3%), measurement of the relative solid angles (1.0%), and measurement of the relative scattering energies (0.2%) are minor sources of the relative cross section probable errors. The major source of uncertainty is in the evaluation of the area beneath the points comprising the momentum spectrum, subtraction of the background, and subtraction of the N^{14} and O^{16} contributions at forward angles (6 to 12%).

The probable error of the absolute value results from uncertainties in the current integrater firing voltage (0.5%), the measurement of the quantity $\frac{Ze\,R}{q\Omega_{C,L}}$ (estimated at about 4% because of the probable error in the stopping cross section for copper and the assumption that copper scattering is Rutherford), the measurement of the absolute angle of scattering (1.0%) and energy of scattering (0.3%), the determination of the area of the proton momentum profile (6%), the determination of the quantity A involved in the absolute cross section measurement (6%), and the stopping cross section of potassium nitrate (6%).

IV. ANALYSIS AND RESULTS OF THE ELASTIC SCATTERING OF PROTONS FROM N^{15}

1. General discussion of analysis procedure

The techniques employed for analyzing the elastic scattering data obtained in the present experiment have been described by Christy (33) and Mozer (27), and the basic theory of the scattering has been given by Bethe (6). The essence of this type of analysis is a comparison of the observed differential cross sections with cross sections calculated from expressions involving various nuclear parameters. Agreement between the calculated and observed cross sections generally is taken to mean that the values assumed for the parameters are correct. The expressions from which the cross sections are calculated have been expressed in a general form by Blatt and Biedenharn (34), but the representation given by Mozer (27) was found in the present work to be more easily applied. A résumé of this representation and the subsequent analysis procedure will be given here in order to define the terminology, to provide a method for obtaining the cross section equations, and to explain how the results described in a following section were deduced.

The cross section for elastic scattering is the absolute square of the amplitude for scattering, taking into consideration the fact that some of the terms of the amplitude interfere coherently while others do not. A convenient representation for the various terms of this amplitude is a matrix which groups all of the mutually coherent terms into individual matrix elements, each

of these elements corresponding to a particular initial and final channel spin configuration. Channel spins are defined as the vectorial combinations of the target nucleus spin I and the proton spin (for protons as the incident particles) so that channel spins $J_{ch} = I \pm \frac{1}{2}$ are possible. A channel spin J_{ch} has $2J_{ch} + 1$ different projections m_{ch} on the Z-axis, and the channel spin configuration is given by specifying J_{ch} and m_{ch}: (J_{ch}, m_{ch}) and (J'_{ch}, m'_{ch}) for initial and final channel spin configurations respectively. This matrix will therefore be square with $(4I+2)^2$ elements. Figure 28 is such a matrix for the case of $N^{15}(pp)N^{15}$, where $I = \frac{1}{2}$.

The usual conservation laws apply to the scattering process, and these laws impose limitations on the kind of terms that can appear in a given matrix element. If ℓ and ℓ' are the orbital momenta (with Z-projections m_ℓ and m') of the incident and scattered protons, and if J is the total angular momentum (with Z-projection m) of the compound nuclear state formed, then the following relations must apply in addition to the conservation of parity:

$$\vec{J}_{ch} + \vec{\ell} = \vec{J} = \vec{J}' + \vec{\ell}' \tag{10}$$

$$m_{ch} = m = m'_{ch} + m' \tag{11}$$

It should be noted that equation 11 is written for the case $m_\ell = 0$, corresponding to an incident plane wave of protons traveling parallel to the Z-axis.

The matrix elements themselves are composed of three types of terms in general. The amplitude for Coulomb scattering f_c is one of these three types; f_c occurs only in diagonal elements since off-diagonal elements correspond to spin reorientation exclusively. This amplitude term is given explicitly by

$$f_c = \sqrt{R}\, e^{i\xi} \quad \text{where} \quad \xi = \frac{Z_0 Z_1 e^2}{\hbar v} \ln\left(\csc^2 \frac{\theta_c}{2}\right), \quad R = \frac{d\sigma_R}{d\Omega_c} \text{ (See eq. 6)} \tag{12}$$

where v is the relative velocity between the incident particle and the target nucleus and where all other symbols are defined as for equation 6.

The other two types of terms in the matrix elements both have the same formal expression in the least complicated case, this expression being a product of three factors. One factor is the product of two Clebsch-Gordon coefficients. A second factor is the spherical harmonic $Y_{\ell'}^{m'}$ defined by Blatt and Weisskopf (35), and the third factor is given by

$$f^J_{J_{ch} J'_{ch} \ell\ell'} = \frac{\sqrt{4\pi}}{2k}\, i^{(\ell - \ell' + 1)} (2\ell + 1)^{1/2}\, e^{i(\eta_\ell + \eta_{\ell'} - 2\eta_0)}\, f^J_{sc} \tag{13}$$

where $$\eta_\ell - \eta_0 = \sum_{j=1}^{\ell} \tan^{-1}\left(\frac{Z_0 Z_1 e^2}{j\hbar v}\right)$$

and where $k = \frac{\mu v}{\hbar}$, μ being the reduced mass of the system. A description of the factor $f_{sc}^{\ J}$ will follow a discussion of the Clebsch-Gordon coefficients.

These coefficients are geometrical factors related to vector addition. Equations 10 and 11 state that the configurations (J_{ch}, m_{ch}) and $(\ell, 0)$ combine to form (J, m) which then decomposes into (J'_{ch}, m'_{ch}) and (ℓ', m'). The quantum mechanical rules for vector addition require

$$|J_{ch} - \ell| \leq J \leq |J_{ch} + \ell|, \quad |J'_{ch} - \ell'| \leq J \leq |J'_{ch} + \ell'|,$$

and that J be integral or half-integral. Results of these requirements are that in general (J_{ch}, m_{ch}) and $(\ell, 0)$ may form several different configurations (J, m) and that a particular (J, m) may decompose into (J'_{ch}, m'_{ch}) and (ℓ', m') which have several combinations of m' and m'_{ch} allowed by equation 11. One of the two Clebsch-Gordon coefficients which appear in a general scattering amplitude term is the probability amplitude that a particular (J, m) is formed. The other Clebsch-Gordon coefficient is the probability amplitude that the (J, m) which is formed then decomposes into a particular combination (J'_{ch}, m'_{ch}) and (ℓ', m'). The properties of these coefficients have been discussed in detail by Condon and Shortley (36).

All nuclear properties are included in the factor f_{sc}^{J}. Two different kinds of nuclear scattering occur: $\underline{f}_{sc}^{J}$ will represent scattering where spin-flip and/or orbital momentum change do not take place, and $\underline{\underline{f}}_{sc}^{J}$ will represent scattering which includes either or both spin-flip and orbital momentum change. No physical distinction between these two types has been made in the present experiment since the particle detector was not capable of differentiating various polarizations and orbital momenta, but such an experiment

could be done in principle. Several degrees of complexity in $\underset{\equiv}{f}^{J}_{sc}$ or $\underset{-}{f}^{J}_{sc}$ exist, depending on whether or not non-resonant scattering and reactions are present. A rather simple case turned out to be satisfactory to describe the present results, so the discussion will be limited to this case. Mozer (27) describes more complex situations, and in some of these cases $\underset{\equiv}{f}^{J}_{sc}$ and $\underset{-}{f}^{J}_{sc}$ no longer have the same formal appearance.

Realistic assumptions about elastic scattering processes generally must allow for nuclear non-resonant scattering in addition to Coulomb and nuclear resonance scattering. The quantity f^{J}_{sc} must account for the nuclear parts of the scattering amplitude. The simplest realistic assumption is to limit the non-resonant scattering to s-wave protons for low energies and to consider non-resonant reactions negligible. The restriction to s-waves may be rationalized as follows. A naive picture of the incident plane wave of protons decomposed into partial waves of different angular momenta limits the closest approach to the nucleus by protons of the ℓ^{th} partial wave to $\ell\lambda\!\!\!^{-}$. For $N^{15}(pp)N^{15}$, $\lambda\!\!\!^{-} \approx 5 \times 10^{-13}(E)^{-\frac{1}{2}}$ cm with the incident proton energy E in Mev. The nuclear radius of N^{15} is approximately 5×10^{-13} cm, so energies of more than one Mev would be necessary before protons with $\ell \neq 0$ would be near enough to the N^{15} so that they could interact appreciably with the average nuclear potential in the region of the nucleus. One way to describe the non-resonant scattering is in terms of this interaction with the nuclear potential, and this description is referred to as potential scattering.

In the following discussion, the so-called potential phase shifts for $\ell \neq 0$ will be assumed to be zero because of the expectation that only s-waves will interact appreciably with the N^{15} nuclear potential in the proton energy range investigated in this work.

By limiting non-resonant scattering to s-waves and by excluding non-resonant reactions, the following definitions of $\underline{f}^{J}_{sc}$ and $\underline{\underline{f}}^{J}_{sc}$ can be used:

$$\text{For } \ell=\ell'=0, \quad \underline{f}^{J}_{sc} = \frac{\Gamma_{psJ}}{\Gamma_J} e^{2i\phi_J}(e^{2i\delta_J}-1) + e^{2i\phi_J} - 1 \qquad (14)$$

$$\text{Otherwise, } \underline{f}^{J}_{sc} = \underline{\underline{f}}^{J}_{sc} = \alpha^{\ell}_{JJ_{ch}} \alpha^{\ell'}_{JJ'_{ch}} \frac{(\Gamma_{p\ell J}\,\Gamma_{p\ell' J})^{\frac{1}{2}}}{\Gamma_J}(e^{2i\delta_J}-1) \qquad (15)$$

where δ_J is the resonant phase shift defined by $\cot \delta_J = \frac{E_R - E}{\Gamma_J/2}$, E_R being the resonance energy and Γ_J being the total width of the state with spin J, where ϕ_J is an s-wave potential phase shift (ϕ_J is ϕ_0 or ϕ_1 for this experiment), where $(a^{\ell}_{JJ_{ch}})^2$ is the fraction of the total amount of compound nucleus of spin J formed by the combination of ℓ with J_{ch}, and where $\Gamma_{p\ell J}$ is the partial width for proton formation or decay of the compound state J by a proton with ℓ orbital momentum. It is to be noted that $\underline{f}^{J}_{sc}$ and $\underline{\underline{f}}^{J}_{sc}$ are formally represented identically in equation 15, but if spin-flip occurs, $J_{ch} \neq J'_{ch}$ and if orbital-momentum change occurs $\ell \neq \ell'$. Moreover, that non-resonant scattering is assumed only if $\ell = \ell' = 0$ and $J_{ch} = J'_{ch}$ explains why $\underline{\underline{f}}^{J}_{sc}$ does not appear in equation 14. This equation is generally written more concisely as follows:

For $\ell=\ell'=0$, $f^J_{sc} = f_J + i g_J - 1$ (14a)

where $f_J = \cos 2\phi_J \left[1 - \frac{2\sqrt{p_s J}}{\sqrt{J}} \sin^2 \delta_J\right] - \frac{2\sqrt{p_s J}}{\sqrt{J}} \sin 2\phi_J \sin\delta_J \cos\delta_J$

$g_J = \sin 2\phi_J \left[1 - \frac{2\sqrt{p_s J}}{\sqrt{J}} \sin^2 \delta_J\right] + \frac{2\sqrt{p_s J}}{\sqrt{J}} \cos 2\phi_J \sin\delta_J \cos\delta_J$

All of the factors appearing in the scattering amplitude matrix elements of figure 28 have now been defined and briefly described. It is to be emphasized that the number of possible terms in each matrix element is infinite since an infinite number of choices for J, ℓ, and ℓ' exist. Those terms shown are for particular choices of J, ℓ, and ℓ', but not even all of these terms were used simultaneously. For instance, the matrix element for the formation and decay of a $J = 2^-$ state by d-wave protons in initial and final channel spin configurations of (1, 1) and (1, 1) respectively, also allowing Coulomb scattering and s-wave non-resonant and resonant scattering, is $f_c + Y^o_o f^1_{11ss} + \frac{1}{2} Y^o_2 f^2_{11dd}$. If one had in addition a $J = 1^+$ state forming and breaking up by p-waves in the same region as the $J = 2^-$ state mentioned above, $\frac{1}{2} Y^o_1 f^1_{11pp}$ would be added to this amplitude, giving four terms. In this way the cross section for quite complicated cases may be obtained. By squaring the absolute value of each matrix element, summing the squares of the sixteen amplitudes, and dividing by four (this is the usual sum over final and average over initial states), the cross section for a particular set of assumptions is obtained. Listed below are certain sets of parameters

which are relevant to this experiment along with the corresponding cross sections. Non-resonant scattering by s-waves is assumed everywhere.

(a) Formation and decay of either or both $J = 0^-$ and $J = 1^-$ states in O^{16} by s-wave protons.

$$\frac{d\sigma/d\Omega_c}{d\sigma_R/d\Omega_c} - 1 = \left[\frac{\sin\xi}{k\sqrt{R'}} - \frac{1}{2k^2R}\right]\left[X-1\right] - \frac{Y\cos\xi}{k\sqrt{R'}} - \frac{U}{4k^2R} \qquad (16)$$

where
$$X = \tfrac{1}{4}f_0 + \tfrac{3}{4}f_1$$
$$Y = \tfrac{1}{4}g_0 + \tfrac{3}{4}g_1$$
$$U = 1 - \tfrac{1}{4}(f_0^2+g_0^2) - \tfrac{3}{4}(f_1^2+g_1^2)$$

Mozer (27) shows (for s-waves only): $U = \frac{\sigma_{\text{reaction}}}{\pi\lambda^2}$. A numerical example of the application of equation 16 is given in Appendix VI.

(b) Formation and decay by s-waves of $J = 0^-$ and/or $J = 1^-$ states plus p-wave formation and decay of a $J = 1^+$ state. Hereafter the subscript J will be omitted from Γ_{pJ} and Γ_J.

$$\frac{d\sigma/d\Omega_c}{d\sigma_R/d\Omega_c} - 1 = \text{equation 16} - \frac{3\Gamma_{pp}\mu}{4\Gamma k\sqrt{R'}}\left[A_1\cos\xi - B_1\sin\xi\right]$$
$$+ \frac{3\Gamma_{pp}\mu}{8\Gamma k^2R}\left[A_1\left\{(1-\alpha^2)g_0+\alpha^2g_1\right\} + B_1\left\{(1-\alpha^2)f_0+\alpha^2f_1-1\right\}\right]$$
$$+ \frac{9\Gamma_{pp}^2\sin^2\delta_1}{8\Gamma^2k^2R}\left[2\mu^2+2\alpha^2(1-3\mu^2)+\frac{3}{2}\alpha^4(3\mu^2-1)\right] \qquad (17)$$

where $\mu = \cos\theta_c$

$\alpha \equiv \alpha'_{11}$; $[(\alpha'_{10})^2 + (\alpha'_{11})^2 = 1$ by definition$]$

$A_1 = 2 \sin\delta_1 \cos(2\eta_1 - 2\eta_0 + \delta_1)$

$B_1 = -2 \sin\delta_1 \sin(2\eta_1 - 2\eta_0 + \delta_1)$

(c) Formation and decay by s-waves of $J = 0^-$ and $J = 1^-$ states plus d-wave formation and decay of a $J = 2^-$ state.

$$\frac{d\sigma/d\Omega_c}{d\sigma_R/d\Omega_c} - 1 = \text{equation 16} - \frac{5\Gamma_{pd} P_2(\mu)}{4\Gamma K\sqrt{R}}\left[A_2\cos\xi - B_2\sin\xi\right]$$

$$+\frac{5\Gamma_{pd} P_2(\mu)}{8\Gamma K^2 R}\left[A_2\{(1-\alpha^2)g_0 + \alpha^2 g_1\} + B_2\{(1-\alpha^2)f_0 + \alpha^2 f_1 - 1\}\right]$$

$$+\frac{25\Gamma_{pd}^2 \sin^2\delta_2}{16\Gamma^2 K^2 R}\left[(1 - 6\mu^2 + 9\mu^4) - \alpha^2(2 - 24\mu^2 + 30\mu^4) + \alpha^4(2 - 21\mu^2 + 25\mu^4)\right] \quad (18)$$

where $P_2(\mu) \equiv$ second Legendre polynomial

$\alpha \equiv \alpha^2_{21}$

$A_2 = 2 \sin\delta_2 \cos(2\eta_2 - 2\eta_0 + \delta_2)$

$B_2 = -2 \sin\delta_2 \cos(2\eta_2 - 2\eta_0 + \delta_2)$

(d) Formation and decay by s-waves of $J = 0^-$ and $J = 1^-$ states plus d-wave formation and decay of a $J = 3^-$ state.

$$\frac{d\sigma/d\Omega_c}{d\sigma_R/d\Omega_c} - 1 = \text{equation 16} - \frac{7\Gamma_{pd} P_2(\mu)}{4\Gamma K\sqrt{R}}\left[A_2\cos\xi - B_2\sin\xi\right]$$

$$+\frac{7\Gamma_{pd} P_2(\mu)}{8\Gamma K^2 R}\left[A_2 g_1 + B_2 f_1 - 1\right] + \frac{\Gamma_{pd}^2 \sin^2\delta_3}{16\Gamma^2 K^2 R}\left[19 - 6\mu^2 + 55\mu^4\right] \quad (19)$$

Symbols as defined in (c).

In the above equations, the parameters $\Gamma_{p\ell}$, Γ, a, ϕ_0 and ϕ_1 are all adjustable. Values of ϕ_0 and ϕ_1 are chosen to obtain the measured non-resonant cross section, and values which provide agreement between the calculated and observed cross sections at resonances are determined for $\Gamma_{p\ell}$, Γ, and a. More detailed information about evaluating these parameters will be given below.

Thus far, the technique for obtaining a theoretical expression for the cross section in terms of the various nuclear parameters has been discussed. Experience in the analysis of elastic scattering data indicates there are essentially two different types of data (see reference 33), and the exact application of the theoretical expressions depends on the type of data to be analyzed. If the resonant scattering either is negligible or results from broad levels (i.e. levels with sufficient total widths so that approximately $\frac{\Gamma}{E_R} > 0.1$), the most fruitful approach is to compare experimental with theoretical angular distributions in order to evaluate the unknown parameters in the cross section equation. On the other hand, narrow levels are more easily analyzed by comparing the cross sections as a function of energy for a given angle. This distinction between narrow and broad level analysis is a result of the character of the cross section equation. The energy and angle dependence of the cross section equation can in general be expressed as follows:

$$\frac{d\sigma/d\Omega_c}{d\sigma_R/d\Omega_c} - | = B(E,\theta_c) + S(E,\theta_c)\sin^2\delta_J + A(E,\theta_c)\sin\delta_J\cos\delta_J \qquad (20)$$

As before $\cot \delta_J = \frac{E_R - E}{\Gamma_J/2}$. The coefficients B, S, and A are energy dependent in rather complex ways, but for small percentage changes of energy, there are but small changes in the coefficients. Narrow level analysis is based on the assumption that the only significant energy variation over the resonance region is in δ_J, making the coefficients B, S, and A dependent only on θ_C and the nuclear parameters. It can be shown in general that as long as one retains the assumption that non-resonant processes with $\ell \neq 0$ do not make appreciable contributions to the scattering, A is proportional to $P_{\ell'}(\cos \theta_C)$. Therefore, the cross section as a function of energy is symmetric around E_R at an angle for which $P_{\ell'}(\cos \theta_C) = 0$ if the excited state decays by emission of a proton with ℓ' units of orbital momentum. Hence, inspection of the measured cross section at several angles frequently leads to the deduction of the orbital angular momentum of the scattered protons. (Accidental symmetries are possible, however, and such possibilities must be investigated.) Narrow level analysis is performed by fitting equation 20 to the excitation functions at several angles, and the values of S and A obtained from this fitting of the experimental data are compared with the values calculated for various assumptions about the nuclear parameters. The fitting of equation 20 is made easier if independent data (from a reaction cross section, for instance) giving values for E_R and Γ are available.

Implicit in broad level analysis is the assumption that the energy variations of δ_J are not confined to small enough regions so that other energy variations may be neglected. Therefore, a

more convenient expression of the cross section equation is of the form of equation 16:

$$\frac{d\sigma/d\Omega_c}{d\sigma_R/d\Omega_c} - 1 = \left[\frac{\sin\xi}{K\sqrt{R}} - \frac{1}{2K^2R}\right]\left[X - 1\right] - \frac{Y\cos\xi}{K\sqrt{R}} - \frac{U}{4K^2R} \qquad (16)$$

where $X = \frac{1}{4}f_0 + \frac{3}{4}f_1$ and $Y = \frac{1}{4}g_0 + \frac{3}{4}g_1$

In a non-resonant region, angular distributions can be compared with this equation to obtain values of X and Y (U has been assumed negligible in non-resonant regions, as discussed above). These values of X and Y are in turn related to the values of the two s-wave potential phase shifts by the expressions following equation 14a. Values of the potential phase shifts at the resonant energies determined in the narrow level analysis may be combined with this information in order to obtain a consistent set of individual potential phase shifts at the energies for which angular distributions were measured. These phase shifts should be monotonically decreasing with energy (the phase shifts are negative) and should not be in violent disagreement with the inequality derived by Wigner (37) given by

$$\frac{d\phi_J}{dK} > -r \qquad (21)$$

where r is the interaction radius. Since the derivation of equation 21 did not take into account any kind of potentials except a square well representing the nucleus, rigorous adherence to it is not required because it is known that other potentials also exist near the

nucleus. However, much more rapid decrease of the potential phase shifts than allowed by equation 21 would cast appreciable doubt on the analysis.

In regions where broad resonances exist, equation 16 is still used to obtain values of X, Y and perhaps U from the experimental angular distributions (U may be obtained from the reaction cross section, if this cross section is known). However here X and Y contain not only information about the potential phase shifts but also information about the s-wave resonant phase shifts. Explicitly, X and Y are given, for the s-wave case, by

$$X = \tfrac{1}{4} f_0 + \tfrac{3}{4} f_1$$
$$Y = \tfrac{1}{4} g_0 + \tfrac{3}{4} g_1$$

where

$$f_J = \cos 2\phi_J \left[1 - \frac{2\Gamma_{psJ}}{\Gamma_J} \sin^2 \delta_J \right] - \frac{2\Gamma_{psJ}}{\Gamma_J} \sin 2\phi_J \sin \delta_J \cos \delta_J$$

$$g_J = \sin 2\phi_J \left[1 - \frac{2\Gamma_{psJ}}{\Gamma_J} \sin^2 \delta_J \right] + \frac{2\Gamma_{psJ}}{\Gamma_J} \cos 2\phi_J \sin \delta_J \cos \delta_J$$

As ϕ_0 and ϕ_1 increase in magnitude (become more negative), X becomes less than unity and Y becomes less than zero. In a plot of X vs. Y the point (X, Y) moves clockwise around the unit circle (if $\phi_0 \approx \phi_1$) as the potential phase shifts increase in magnitude. Now if an s-wave resonance exists, a counter-clockwise circle of radius $\frac{(2J+1)\Gamma_{psJ}}{4\Gamma_J}$ is superposed on the more slowly moving clockwise circle as δ_J goes between 0 and π. From such plots of X vs. Y, therefore, one can obtain an estimate of $\frac{(2J+1)\Gamma_{psJ}}{4\Gamma_J}$

from the radius of the circle. If $\frac{\Gamma_{psJ}}{\Gamma_J}$ is known from other experimental data, then frequently J can be immediately determined. Such an approach is not very accurate, however, since the "counter-clockwise circles" are distorted by changes in $\frac{\Gamma_{psJ}}{\Gamma_J}$ and ϕ_J as δ_J goes between 0 and π. In addition, the experimental data are not likely to produce values of X and Y that fall nicely on a well defined line.

If the plot of X vs. Y does indicate that the broad resonance is s-wave, then detailed angular distributions can be calculated by computing values of X and Y for the best choices of ϕ_J, Γ_{psJ}, E_R, Γ_J, and J available from the X vs. Y plot. Comparison with the experimental angular distributions may suggest changes for improving the agreement. In this way, a set of values for the nuclear parameters may be obtained which is consistent with the experimental data.

One further effect that must be considered in the analysis of broad levels is the energy-dependent level shift that appears in the theory of Wigner and Eisenbud (38). Thomas (39) has shown this effect to be important in some cases. The method given by Thomas for calculating this quantity has been used and is discussed in more detail in Appendix V. Increases of about 10% in the observed level widths are indicated from these calculations, but small changes in the nuclear radius affect this correction considerably, so no correction has been made to the values of the widths quoted below.

The present results have been adequately described in terms of two broad s-wave resonances, three narrow non-s-wave resonances, and only s-wave non-resonant scattering. Therefore the preceding discussion should be a sufficiently comprehensive background for the analysis and results to be discussed in the following sections.

2. Analysis and results

(a) Non-resonant scattering

All of the experimental data were consistent with only s-wave non-resonant scattering and zero non-resonant reaction cross sections. The potential phase shifts ϕ_0 and ϕ_1 could not be determined very accurately from the data, but consistency is obtained with the following values, through which a smooth curve may be drawn for interpolation:

E kev	$\phi_0 = \phi_1$ Degrees
650	-4.2
800	-7.5
950	-10.3
1100	-12.9
1250	-15.3
1400	-17.4
1550	-19.3
1700	-20.9
1800	-21.7

These values do not violate the inequality given by equation 21, and the agreement between the theoretical and experimental angular distributions may be seen in figures 10 to 22. By referring to figure 9, the non-resonant regions of the cross section may be selected for this comparison, since several of the angular distributions are at energies relatively close to resonances.

An inspection of equation 16 and the definitions of X and Y indicates that the cross section is more strongly dependent on changes in ϕ_1 than in ϕ_0. It has been empirically shown that 30-40% changes in ϕ_0 can be fairly well covered up by smaller changes in ϕ_1. To within the accuracy of the data, a choice of a unique set of values is not possible. The values tabulated above appear to be in the middle of the allowable range of fluctuation. In general, the interference terms could not be used for a more accurate estimate of ϕ_0 and ϕ_1 in the vicinity of a narrow resonance, either. Only ϕ_1 appears in equation 19, for example, which is applicable to the 1210-kev state. However $\frac{\Gamma_{pd}}{\Gamma}$ is not known accurately, and again a range of possible values for ϕ_1 exists. Both of these ranges of ϕ_1 are consistent with one another, but the fact remains that ϕ_1 and ϕ_0 are not precisely known since similar ambiguities also occur at the other narrow resonances.

(b) The 710-kev state

The 710-kev state was discovered in this research. The elastic scattering excitation functions shown in figure 9 exhibit pronounced anomalies near 710 kev, and the data for 90° and $125^\circ 16'$ exhibit interference minima for this state. Because the

antisymmetric interference terms are proportional to $P_{\ell'}(\cos \theta_c)$, pure p- or d-wave formation and decay of the 710-kev state can be immediately excluded. In view of the relatively large width of the state, s-wave formation is strongly indicated. The elastic scattering data obtained in the present work are quantitatively consistent with s-wave formation of a $J = 0^-$ state at 710 $\pm$ 7 kev with a total width of 40 $\pm$ 4 kev at 710 kev. Figures 10 to 12 illustrate the comparison between the observed and calculated angular distributions, and figure 29 is a plot of X vs. Y as discussed above, the values of X and Y plotted being those that went into the calculation of the angular distributions shown as solid curves in figures 10 to 22.

All other information about the 710-kev state is consistent with the assignment $J = 0^-$. Previous work (3) shows that this state does not decay by long range alphas (α_0), short range alphas (α_1), or by the ground state gamma transition. Additional evidence against the gamma transition was obtained in this work by detecting the 13-Mev gamma radiation from the 1028-kev state with a 4" x 4" NaI(Tl) crystal for a measurement of the excitation function from 600 to 1000 kev. Although the rise from the 1028-kev state was apparent at 700 kev, no indication of resonance at 710 kev was observed in the 13-Mev radiation. A $J = 0^-$ state at this energy would be forbidden by angular momentum conservation to decay by alpha particles because C^{12} must be left in a $J = 0^+$ or $J = 2^+$ state. Similarly the ground state gamma ray transition

would be $0 \rightarrow 0$ which also is forbidden. The assignment $J = 0^-$ thus accounts for these absences.

One would expect, however, that cascading gamma ray decay should occur if this state is $J = 0^-$. Such gamma rays were found, and an excitation function of 5-9 Mev gamma rays is shown in figure 30. A pulse height analysis of these gamma rays is shown in figure 31. These gamma rays were detected with the 4" x 4" NaI(Tl) crystal. Kavanagh (40) has measured the pulse height spectra from several pure gamma rays detected with this crystal, and the full-energy and pair-plus-one peaks are about the same size for the 4.43-Mev gamma ray. For a 6.13-Mev gamma ray, the pair-plus-one peak is about 1.5 times the pair and full-energy peaks.

The solid curve drawn through the points in figure 30 has been calculated, taking into account both the effects of target thickness and the energy dependence of the total width, initially assuming a Breit-Wigner one level formula. The expression used for this calculation is derived in Appendix III. That the experimental points begin to rise above the curve near 775 kev is a result of a tail on the 13-Mev gamma ray pulse height spectrum; this tail was producing appreciable 5-9 Mev "counts" above 775 kev.

Although no attempt was made in the present work to obtain an accurate measurement of the energies of the cascading gamma rays, figure 31 is certainly consistent with the hypothesis that the $J = 1^-$ state at 7.12 Mev in O^{16} is the intermediate step in the cascade. A more accurate measurement would be desirable, but the difficulties are substantial because of the relatively large cross

section for the production of the 4.43-Mev gamma rays (see figure 31) from the first excited state of C^{12}. It is of interest to point out, however, that this situation is one whereby a direct check of the M1 versus M2 transition rates can be made if the predominant mode of decay of the 710-kev state is through the $J = 1^-$ state at 7.12 Mev. A $J = 2^+$ state at 6.91 Mev is known, and a sufficiently detailed experiment could directly compare the number of magnetic dipole transitions with the number that are magnetic quadrupole. The complete decay scheme may be complicated by the fact that the 7.12-Mev state decays primarily to the ground state, apparently violating the isotopic spin selection rule (41).

(c) The 898-kev state

Considerable information was available about the 898-kev state at the time this elastic scattering measurement was initiated (see page 136 of reference 1 for a summary and further references). Angular distributions of the α_1-particles and of the 4.43-Mev gamma rays had separately given the assignment $J = 2^-$, as had the α_1-γ angular correlation. Formation and decay of this state by d-waves were indicated. Narrow level analysis of the scattering data was applied to this level, since $\Gamma = 2.2$ kev, and equation 18 written in the form of equation 20 was employed. By using the channel spin ratio quoted by Kraus et al. (4), the experimental data were used to determine a value of $\frac{\Gamma_{pd}}{\Gamma}$ that gave the best agreement between calculated and observed cross sections. The value obtained was $\frac{\Gamma_{pd}}{\Gamma} = 0.56$, and the solid curves shown in figures 23 and 24

were calculated assuming a d-wave $J = 2^-$ state. The resolution corrections shown in these figures were calculated using a technique similar to the one discussed by Webb et al. (12). The target thicknesses were fairly accurately determined for these resolution corrections by obtaining excitation functions of the 4.43-Mev gamma rays, thereby providing a technique independent of the magnetic spectrometer for measuring the target thickness.

The above value of $\frac{\Gamma_{pd}}{\Gamma}$ may be used to calculate the reaction cross section for the α_1-particle reaction by application of the Breit-Wigner single level formula

$$\sigma_{Reaction} = \frac{\omega \pi \lambda^2 \Gamma_{pd} \Gamma_{\alpha_1}}{(E_R - E)^2 + \Gamma^2/4} \qquad (22)$$

where ω is the statistical factor $\frac{2J+1}{(2S+1)(2I+1)}$ with S and I the spins of the incident and target nuclei, where λ is the reduced wave length for the incident protons, and where Γ_{pd} and Γ_{α_1} are the partial proton and alpha widths. At resonance,

$$\sigma_{Reaction} = 4\pi \lambda^2 \omega \frac{\Gamma_{pd}(\Gamma - \Gamma_{pd})}{\Gamma^2}$$

for the 898-kev state since $\Gamma_{pd} + \Gamma_{\alpha_1} \approx \Gamma$. Then

$\sigma_{\text{Reaction}} = 1.02$ barns by using $\frac{\Gamma_{pd}}{\Gamma} = 0.56$.

The measured value of this cross section obtained from the data of Kraus et al. (4) is 0.83 ± 0.21 barns. Therefore all available information is consistent with d-wave formation of a $J = 2^-$ state at 898 kev.

(d) The 1028-kev state

The 1028-kev state had been studied in some detail prior to this experiment (see reference 1, page 136). This state was thought to decay by both kinds of alpha particles and by 13-Mev gamma rays, but some question existed as to whether or not there were two states very close to one another, one giving rise to the alpha particles and the other decaying by gamma rays. The broad level analysis of the elastic scattering data gives no evidence for the existence of two levels, and both the scattering data and a recently measured excitation function for the 13-Mev gamma rays are consistent with a $J = 1^-$ state formed by s-waves at 1028 $\pm$ 10 kev with a total width of 140 $\pm$ 7 kev at 1028 kev. This gamma ray excitation function from a thin target is shown in figure 32, where the solid line has been calculated from the single level formula including the energy dependence of the total and partial widths. The elastic scattering data are shown with calculated angular distributions in figures 13 to 16, and the X vs. Y plot may be seen in figure 29. As was done for the 710-kev state, the values of X and Y plotted are those derived from the solid lines in the figures showing the angular distributions. The calculated cross sections are for $\frac{\Gamma_{ps}}{\Gamma} = 0.8$ at 1028 kev. The reaction cross section for $N^{15}(p\alpha_0)C^{12}$ has been measured (3, 5) and that for $N^{15}(p\alpha_1\gamma)C^{12}$ can be estimated from the gamma ray excitation function (5), giving a total of 0.4 barns to be compared with 0.35 barns calculated from $\frac{\Gamma_{ps}}{\Gamma} = 0.8$ and $J = 1$. (These reaction cross section values were used to calculate values of U for the broad level analysis.)

The formation of a $J = 1^-$ state at 1028 kev by s-wave protons therefore appears well established, and this state appears to be a mixture of isotopic spins $T = 0$ and $T = 1$ (42).

(e) The 1210-kev state

Previous investigations of the 1210-kev state (see reference 1) had included measurement of excitation functions for both kinds of alpha particles and separate angular distributions of the α_1-particles and the 4.43-Mev gamma rays. The α_1 distribution was measured by Kraus et al. (4), and the gamma ray angular distribution has been measured by Kraus et al. and by Barnes et al. (43). The gamma ray data were shown to be consistent with either $J = 3^-$, $\ell_p = 2$, $\ell_a = 1$ and 3, or $J = 4^+$, $\ell_p = 3$, $\ell_a = 2$. Higher values of J could also fit the data. The α_1 angular distribution appeared to exclude $J = 3^-$ but was consistent with $J = 4^+$. So the $J = 4^+$ assignment was accepted, although the single particle limit of the f-wave partial proton width predicted a reaction cross section only half the size of the measured value, as mentioned above.

However, the $J = 4^+$ assignment now has a strong argument against it. The elastic scattering data shown in figures 25 and 26 are impossible to describe in terms of this assignment. As has been pointed out above, the antisymmetric term in the cross section equation is proportional to $P_{\ell'}(\cos \theta_C)$. A state with $J = 4^+$ could be formed with $\ell_p \geq 3$, and by conservation of parity, formation and decay must take place only with odd ℓ_p-values. $P_\ell(\cos \theta_C)$ is zero for all odd values of ℓ at $\theta_C = 90^\circ$, but the

experimental cross section of figure 26 indicates distinctly that an antisymmetric term is present. This argument excludes, in addition to $J = 4^+$, all even-parity assignments. The fact that the 1210-kev state decays by α_0-particles requires that its spin-parity assignment be even-even or odd-odd. Hence only odd-odd assignments remain. The assignment $J = 3^-$ for this state, forming and decaying by d-wave protons, was used for the calculation of the solid lines shown in figures 25 and 26, with $\frac{\Gamma_{pd}}{\Gamma} = 0.18$. Using these values to calculate the reaction cross section, one gets 0.63 barns. The measured α_0 cross section is 0.31 barns (5) and the measured α_1 cross section is 0.37 barns (4), giving a total of 0.68 barns. The agreement is entirely satisfactory as far as the scattering data is concerned, but the α_1 angular distribution measured by Kraus et al. appears to distinctly contradict these scattering data deductions.

Therefore, this angular distribution was remeasured. The results of this measurement are shown in figure 33, and figure 34 shows a typical momentum profile obtained. The angles less than 90° were done with N^{15} embedded in 200 microgram per cm^2 aluminum leaf, but the targets used for elastic scattering sufficed for the back angles. Complete agreement with the earlier measurements of Kraus et al. were obtained. The accuracy of the data excludes agreement with the $J = 3^-$ curve.

An investigation of other possible explanations of this phenomenon has been made. The expression for the α_1 angular distribution for any mixture of d- and g-wave protons forming a $J = 3^-$ state which decays by any mixture of p- and f-wave

alphas has been calculated and is given in Appendix IV. The necessary $\cos^4\theta_c$ and/or $\cos^6\theta_c$ dependence to fit the data shown in figure 33 cannot result from this expression assuming $\frac{\Gamma_{pg}}{\Gamma_{pd}} \leq 0.01$. Such an assumption seems necessary in view of the fact that $\frac{\Gamma_{pg}}{\Gamma} \leq 0.003$ in order not to exceed the single particle limit for the reduced partial proton width. A $J = 1^-$ state formed by any mixture of s- and d-wave protons which decays by any mixture of p- and f-wave alphas has terms only up to $\cos^2\theta_c$ and therefore is not acceptable. The only remaining solutions lie in the region of higher J. The case of $J = 5^-$ has been considered, and the a_1 distribution expected from formation by g-wave protons and decay by f-wave alphas has been calculated and is given in Appendix IV. This distribution permits reasonable agreement with the experimental data, but the elastic scattering data cannot be fitted with these assumptions. In the first place, $\frac{\Gamma_{pg}}{\Gamma} \leq 0.003$ would produce an anomaly too small to observe. Secondly, if the cross section equation is written in the form of equation 20 and if the coefficients S and A are evaluated for the case $J = 5^-$ and $\ell = \ell' = 4$, using values of potential phase shifts consistent with those listed above, then

$$S = -0.82 \frac{\Gamma_{pg}}{\Gamma} + 1.81 \frac{\Gamma_{pg}^2}{\Gamma^2}$$

and

$$A = 2.47 \frac{\Gamma_{pg}}{\Gamma}$$

The measured cross section at 90° dips and then rises with increasing energy. These values of S and A would give a rise followed by a dip for any value of $\frac{\Gamma_{pg}}{\Gamma} \leq 1$.

Higher values of J and ℓ appear totally unreasonable, so one is left with an apparent paradox. The only data inconsistent with the $J = 3^-$ assignment is the α_1 angular distribution, but independent measurements of this quantity gave good agreement with one another. A determination of the α_1-γ angular correlation would perhaps be useful for resolving this situation. The correlation function for d-wave proton formation of a $J = 3^-$ state which decays by any mixture of p- and f-wave alphas and the correlation function for f-wave proton formation of a $J = 4^+$ state which decays by d-wave alphas have been calculated from a general expression given by Seed and French (44) and are given in Appendix IV. Plots of three of these functions are shown in figure 35, and it appears that a choice between these two values of J should certainly be possible. As of the present, however, the assignment for the 1210-kev state has not been definitely established.

(f) The 1640-kev state

The 1640-kev state was known to decay by α_1-particles. Prior to the present work, a study had been made by Kraus (45) of the angular distribution of the 4.43-Mev gamma rays from C^{12}, and these results were consistent with $J = 1^+$ or $J = 2^-$. A recent remeasurement of this angular distribution (5) had favored $J = 1^+$ but was still in agreement with the channel spin ratios given by Kraus. The elastic scattering data are shown in figure 27. Narrow level analysis has been applied, although this state was borderline between being broad and narrow with $\Gamma = 68$ kev (5). The solid lines shown in figure 27 are calculated (using the channel

spin ratio obtained from the gamma ray angular distributions) for p-wave formation and decay of a $J = 1^+$ state with $\frac{\Gamma_{pp}}{\Gamma} = 0.15$, $\Gamma = 68$ kev, and $E_R = 1640$ kev. The agreement is satisfactory, and $J = 1^+$ appears well established. The resonant reaction cross section calculated for this state is 0.18 barns; a measurement of this quantity has not been made.

(g) Summary

Five excited states of O^{16} between 12.67 and 13.80 Mev have been investigated in this research. In Table III is a summary of information available about these states as a result of this and previous work.

TABLE III. Properties of Five Excited States of O^{16} Reached by $N^{15}+p$.

E_R (kev)	J^π	ℓ_p	Γ (kev)	$\frac{\Gamma_{p\ell}}{\Gamma}$	$\frac{\gamma_{p\ell}}{(\gamma_{p\ell})_{Lim}}$
710±7*	0^{-*}	0^*	40±4	1*	0.10*
898±1	2^-	2	2.2±0.2	0.56*	0.07*
1028±10†	1^-	0	140±10†	0.8*	0.09*
1210±2	$(3^-)^*$	(2)*	22.5±1	(0.18)*	(0.06)*
1640±3	1^{+*}	1*	68±3	0.15*	0.007*

In this table, uncertain quantities appear in parentheses. E_R is the resonance energy for the incident protons in kev, J^π is the

---

*Denotes quantities uniquely determined by the present work.

†This state has previously been referred to as $E_R = 1050$ kev and $\Gamma = 150$ kev.

spin and parity of the O^{16} state, ℓ_p is the orbital momentum of the proton forming the state, Γ is the total width in kev, $\Gamma_{p\ell}$ is the partial proton width for the state, and $\gamma_{p\ell}/(\gamma_{p\ell})_{Lim}$ is the ratio of the reduced partial proton width to the single particle limit of the reduced partial proton width. For calculation of this ratio, a nuclear radius of 4×10^{-13} cm has been used, and the quantity $P_\ell \; E_1^{\frac{1}{2}}$ has been taken from the graphs of Christy and Latter (46). The equation

$$\gamma_{p\ell}/(\gamma_{p\ell})_{Lim} = 0.0367 \frac{M_0 R \Gamma_{p\ell}}{(M_0+M_1) P_\ell E_1^{\frac{1}{2}}} \times 10^{13}$$

defines $\gamma_{p\ell}/(\gamma_{p\ell})_{Lim}$ where R is the nuclear radius in centimeters, $\Gamma_{p\ell}$ is the observed partial width in Mev in the laboratory system, P_ℓ is the penetration factor, and E_1 is the incident proton energy in Mev in the laboratory system, M_1 is the mass of the proton, and M_0 is the mass of the target nucleus.

APPENDIX I, Part 1

To show: $\frac{\partial E_2}{\partial M_0} > 0$ if $M_0 > M_1$ (see equation 1)

Given: $$E_2 = E_1\left\{\frac{M_1\cos\theta_L}{M_1+M_0} + \left[\frac{M_1^2\cos^2\theta_L}{(M_0+M_1)^2} + \frac{M_0-M_1}{M_0+M_1}\right]^{\frac{1}{2}}\right\}^2$$

$$\frac{\partial E_2}{\partial M_0} = 2E_1\left\{\frac{-M_1\cos\theta_L}{(M_1+M_0)^2} + \frac{M_0M_1+M_1^2\sin^2\theta_L}{(M_0+M_1)^3\left[\frac{M_1^2\cos^2\theta_L}{(M_0+M_1)^2} + \frac{M_0-M_1}{M_0+M_1}\right]^{\frac{1}{2}}}\right\}$$

$$\times\left\{\frac{M_1\cos\theta_L}{M_1+M_0} + \left[\frac{M_1^2\cos^2\theta_L}{(M_0+M_1)^2} + \frac{M_0-M_1}{M_0+M_1}\right]^{\frac{1}{2}}\right\}$$

The bracket $\left\{\frac{M_1\cos\theta_L}{M_1+M_0} + \left[\frac{M_1^2\cos^2\theta_L}{(M_0+M_1)^2} + \frac{M_0-M_1}{M_0+M_1}\right]^{\frac{1}{2}}\right\}$ may be seen by inspection to be greater than zero, while straightforward algebra produces the identity

$$\left\{-\frac{M_1\cos\theta_L}{(M_1+M_0)^2} + \frac{M_0M_1+M_1^2\sin\theta_L}{(M_0+M_1)^3\left[\frac{M_1^2\cos^2\theta_L}{(M_0+M_1)^2} + \frac{M_0-M_1}{M_0+M_1}\right]^{\frac{1}{2}}}\right\}$$

$$\equiv \frac{M_1}{(M_0+M_1)^2}\left\{-\cos\theta_L + \frac{(1+\frac{M_1}{M_0}\sin^2\theta_L)}{(1-\frac{M_1^2}{M_0^2}\sin^2\theta_L)^{\frac{1}{2}}}\right\}$$

Recalling $M_0 > M_1$, the last bracket can be seen to be always greater than zero, proving $\frac{\partial E_2}{\partial M_0} > 0$.

APPENDIX I, Part 2

Derivation of equation 9:

It is desired to obtain an expression relating the thick target gamma ray yield from an evaporated KNO_3 target enriched in N^{15} to 61% to the thin target gamma ray yield from an N^{15} target in a

graphite disk. The gamma ray yield from a target of thickness ξ is given by

$$Y = \int_{E-\xi}^{E} \sigma(E') \frac{dE'}{\varepsilon} \tag{1'}$$

where $\sigma(E)$ is the cross section for the gamma ray reaction and ε is the stopping cross section for the incident particles in the target material per N^{15} nucleus. For the case of a thin target (i.e. $\xi \ll E$),

$$dY = \sigma(E) \frac{dE}{\varepsilon} \tag{2'}$$

Here ε is the stopping cross section per N^{15} nucleus in the graphite disk. This quantity is a function of the local density of the N^{15}, denoted by $\rho(x)$, where x is the distance beneath the graphite surface. Therefore in an incremental distance dx, the energy lost dE by protons passing through dx is

$$dE = \varepsilon \rho(x)\, dx \tag{3'}$$

Combining equations 2' and 3' gives

$$dY(E,x) = \sigma(E)\rho(x)\, dx \tag{4'}$$

Now if the integration over x is performed keeping E constant at x, the resulting integral corresponds to the yield from all target nuclei at a single energy and is:

$$Y(E) = \sigma(E)\, n_T \tag{5'}$$

where $n_T = \int_0^\infty \rho(x)dx$, n_T therefore being the total number of N^{15} nuclei per unit area exposed to the incident beam. Integration over E then gives, using the Breit-Wigner one level expression for $\sigma(E)$,

$$A = \int_{E_1}^{E_2} Y(E)dE = \frac{2\pi\lambda^2 \omega \Gamma_\rho \Gamma_\gamma}{\Gamma} n_T \left[\tan^{-1}x_2 - \tan^{-1}x_1\right] \qquad (6')$$

where $$x_i = \frac{E_i - E_R}{\Gamma/2}$$

In the case where the target thickness ξ is somewhat larger, but still not large enough so that the energy dependence of ε and λ^2 are of importance, then

$$Y = \frac{\lambda^2}{\varepsilon} \int_{E-\xi}^{E} \frac{\sigma(E')dE'}{\lambda^2} = \frac{2\pi\lambda^2 \omega \Gamma_\rho \Gamma_\gamma}{\varepsilon \Gamma}\left[\tan^{-1}(x) - \tan^{-1}(x - \frac{2\xi}{\Gamma})\right] \qquad (7')$$

The maximum value of Y occurs at $E = E_R + \frac{\xi}{2}$ giving

$$Y_{max} = \frac{4\pi\lambda^2 \omega \Gamma_\rho \Gamma_\gamma}{\varepsilon \Gamma} \tan^{-1}(\frac{\xi}{\Gamma}) \qquad (8')$$

Dividing equation 8' by equation 6' and solving for n_T gives the desired expression

$$n_T = \frac{A}{(\tan^{-1}x_2 - \tan^{-1}x_1)} \times \frac{2\tan^{-1}(\frac{\xi}{\Gamma})}{\varepsilon Y_{max}} \qquad (9')$$

For the case $\xi \gg \Gamma$ and $|x_i| \gg 1$, the inverse tangents approach $\pi/2$ resulting in

$$n_T \approx \frac{A}{\varepsilon Y_{max}} \qquad (10')$$

APPENDIX II--Method of calculation of the $O^{16}(pp)O^{16}$ cross section for scattering angles of 115^{o} or less

The $O^{16}(pp)O^{16}$ cross section had to be known as a function of angle and energy in order to correct for the presence of O^{16} in the N^{15} targets. The only available O^{16} scattering data for the energies of interest was that given in reference 31 and renormalized by reference 32. Reference 31 reported the differential cross section at a laboratory angle of 164^{o}. For purposes of the present work, it was necessary to know the cross section at smaller scattering angles. The assumption was therefore made that the scattering resulted only from the Coulomb interaction and from an s-wave potential phase shift. Because O^{16} has a $J = 0^{+}$ ground state, only one s-wave potential phase shift exists, and this phase shift was evaluated from the 164^{o} data by using equation 16 with the appropriate re-definitions. Given in the following tabulation are the values of the s-wave potential phase shift obtained as a function of proton energy.

Proton energy (kev)	Phase shift (radians)
600	-.039
900	-.135
1200	-.250
1500	-.385
1800	-.490

Using these phase shifts, the cross sections at scattering angles of 75^{o}, 90^{o}, and 115^{o} were calculated for the range of energies of interest.

APPENDIX III--Calculation of the gamma ray excitation function for the 710-kev state

The gamma ray excitation function for the 710-kev state was measured by using a target of thickness ξ which was of the same general magnitude as the total width Γ of the state. Moreover, the energy variation of the total width, proportional to $P_\ell E^{\frac{1}{2}}$ where P_ℓ is the penetration factor for ℓ units of orbital momentum, was large over an energy region of the same size as the total width. These two effects have been taken into account approximately in the following way. The gamma ray yield from a target of thickness ξ is given by

$$Y(E) = \int_{E-\xi}^{E} \frac{\sigma(E')dE'}{\varepsilon}$$

where ε is the stopping cross section per disintegrable nucleus. The cross section is assumed to be given by the Breit-Wigner one level formula

$$\sigma(E) = \frac{\omega \pi \lambda^2 \Gamma_\rho \Gamma_\gamma}{(E-E_R)^2 + \Gamma^2/4}$$

For this particular case, $\Gamma_\rho \approx \Gamma$ and $\Gamma \sim P_o E^{\frac{1}{2}}$. Values of P_o have been calculated from the tables of Bloch et al. (47), and a linear approximation of $\Gamma = 2(a_0 + a_1 E)$ fits the calculated values quite adequately. Hence by neglecting the energy dependence of ε ,

$$Y(E) \sim \int_{E-\xi}^{E} \frac{(a_0+a_1E')dE'}{E'\left[(E'-E_R)^2+(a_0+a_1E')^2\right]}$$

$$Y(E) \sim \left\{\frac{a_0}{2(E_R^2+a_0^2)}\right\} \ln \left[\frac{E^2\left[(E-\xi-E_R)^2+(a_0+a_1E-a_1\xi)^2\right]}{(E-\xi)^2\left[(E-E_R)^2+(a_0+a_1E)^2\right]}\right]$$

$$+\left\{\frac{1}{a_0+a_1E_R}\right\}\left\{\frac{(a_0E_R-a_0^2a_1)}{(E_R^2+\Gamma^2/4)}+a_1\right\}\left\{\tan^{-1}\left[\frac{(1+a_1^2)E+a_0a_1-E_R}{a_0+a_1E_R}\right]\right.$$

$$\left.-\tan^{-1}\left[\frac{(1+a_1)^2(E-\xi)+a_0a_1-E_R}{a_0+a_1E_R}\right]\right\}$$

Knowledge of ξ, a_0, and a_1 enabled calculation of the relative excitation function if values of E_R and Γ at E_R were assumed.

APPENDIX IV. Various angular distribution and correlation functions

Given below is the alpha particle angular distribution for formation of a $J = 3^-$ state by combining d- or g-wave protons with a $J = \frac{1}{2}^-$ nucleus, and then allowing alpha decay by p- or f-waves to a $J = 2^+$ state. The partial width ratios are given in terms of the following parameters:

$$\Gamma_{pg} = A^2 \Gamma_{pd} \qquad \text{and} \qquad \Gamma_{\alpha f} = B^2 \Gamma_{\alpha p}$$

The phase difference between the proton waves is denoted by α and the phase difference between the alpha particle waves is denoted by β. The angle θ_C is the center-of-mass angle between the incoming protons and the outgoing alphas, and $\mu = \cos\theta_C$.

$$W(\mu) \sim 46 + 25A^2 + \frac{1659}{20} B^2 + \frac{1155}{32} A^2B^2 + \frac{959\sqrt{15}}{40} AB^2 \cos\alpha$$

$$+ \frac{4\sqrt{15}A\cos\alpha}{3} + 18\sqrt{7}\, AB \cos\alpha \cos\beta - \frac{(18+25A^2)}{6}\sqrt{\frac{21}{5}} B \cos\beta$$

$$+ \left\{72 + \frac{125}{3} A^2 + \frac{2709}{10} B^2 + \frac{10325}{32} A^2B^2 - \frac{16527}{40}\sqrt{15}\, AB^2 \cos\alpha \right.$$

$$\left. -4\sqrt{15}\, A\cos\alpha + 3(174 + 125A^2)\sqrt{\frac{21}{5}} B\cos\beta - 204\sqrt{7}\, AB\cos\alpha\cos\beta \right\}\mu^2$$

$$+ \left\{ -\frac{945}{4} B^2 - \frac{19075}{32} A^2B^2 + \frac{8925}{8}\sqrt{15}\, AB^2\cos\alpha \right.$$

$$\left. + 250\sqrt{7}\, AB\cos\alpha\cos\beta - \frac{25}{2}(22 + 15A^2)\sqrt{\frac{21}{5}} B\cos\beta \right\}\mu^4$$

$$+ \left\{ \frac{30625}{96} A^2B^2 - \frac{6125}{8}\sqrt{15}\, AB^2\cos\alpha \right\}\mu^6 .$$

The magnitude of the cosine of the phase difference between two partial waves ℓ and ℓ' in a Coulomb field is given by Bloch et al. (47).

$$\left|\cos\left[\sum_{j=\ell'+1}^{\ell}\left(\tan^{-1}\frac{\eta}{j}\right)-\pi\right]\right|$$

Here $\eta = 0.1574\, Z_1 Z_2 \left(\frac{A_{red}}{E_C}\right)^{\frac{1}{2}}$ with Z_1 and Z_2 denoting the nuclear charges of the two particles with relative orbital momentum ℓ or ℓ', A_{red} being their "reduced mass number", and E_C being the center-of-mass energy in Mev. For the 1210 resonance in $N^{15}+p$,

$$\cos\alpha = \pm 0.846$$

$$\cos\beta = \pm 0.030$$

* * * * * * * * *

Given below is the α_1-γ correlation function for the formation of a $J = 3^-$ state by combining d-wave protons with a $J = \frac{1}{2}^-$ nucleus. This state then decays by p- and f-wave alphas to a $J = 2^+$ state which in turn goes by electric quadrupole radiation to a $J = 0^+$ state. The alphas are observed at an angle of 90° in the center-of-mass system with respect to the incident protons. The gamma rays are observed in the plane established by the incoming protons and outgoing alphas, and θ_C is the center-of-mass angle between the alphas being observed and the gamma rays being observed. B, μ, and $\cos\beta$ are defined as above.

$$C(\mu) \sim \left(1-\sqrt{\tfrac{21}{6}}\,B\cos\beta+\frac{7B^2}{48}\right)+\left(\frac{7\sqrt{21}}{18}\,B\cos\beta-\frac{217B^2}{432}\right)\mu^2$$
$$-\left(\frac{13}{9}+\frac{11\sqrt{21}}{27}\,B\cos\beta+\frac{14}{27}B^2\right)\mu^4$$

* * * * * * * * * * * *

The correlation function is given below for f-wave protons combining with a $J = \frac{1}{2}^-$ nucleus for the formation of a $J = 4^+$ state which decays by d-wave alphas. All else is the same as in the immediately preceding correlation function.

$$C(\mu) \sim 1 - \frac{141}{50}\mu^2 + \frac{58}{125}\mu^4$$

* * * * * *

Given below is the angular distribution for g-wave proton formation of a $J = 5^-$ state from a $J = \frac{1}{2}^-$ nucleus followed by f-wave alpha decay to $J = 2^+$ state.

$$W(\mu) \sim 171 + 186\mu^2 - 525\mu^4 + 952\mu^6$$

APPENDIX V--Effects of the level shift on the observed widths of broad levels

Thomas (39) has given formulas for the calculation of the level shift Δ_λ which appears in the theory of Wigner and Eisenbud (38) and for the calculation of the true width Γ_λ in terms of the observed width Γ'_λ. These expressions are

$$\Delta_\lambda = -\sum (g_{s\ell} + \ell)\gamma_{\lambda s\ell}$$

$$\Gamma'_{\lambda s\ell} = \Gamma_{\lambda s\ell}\left[1 + \sum \gamma_{\lambda s\ell}\left(\frac{dg_{s\ell}}{dE}\right)_{E=E_R}\right]^{-1}$$

$$\Gamma_\lambda = \sum \Gamma_{\lambda s}$$

where the level shift, observed resonance energy E_R, and true resonance energy E_λ satisfy

$$E_\lambda + \Delta_\lambda - E_R = 0 .$$

The quantity $g_{s\ell}$ is defined as:

$$g_{s\ell} = \left\{\frac{d\left[\ell n(F_{s\ell}^2 + G_{s\ell}^2)^{\frac{1}{2}}\right]}{d\left[\ell n(kr)\right]}\right\}_{r=R}$$

where $F_{s\ell}$ and $G_{s\ell}$ are the regular and irregular solutions of the wave equation defined by Bloch et al. (47). The definition for $\gamma_{\lambda s\ell}$ in units of Mev is

$$\gamma_{\lambda s\ell} = 2.277 \frac{\Gamma_{\lambda s\ell}}{P_{s\ell} E^{\frac{1}{2}}} \frac{10^{-13}}{R} \text{ Mev}$$

where $\Gamma_{\lambda s\ell}$ is the partial width in Mev for s-type particles with ℓ orbital momentum for the λ^{th} state, E is the energy in Mev of the s-type particle in the laboratory system, and R is the nuclear

radius in centimeters. By using these definitions and the tables of Bloch et al. (47), Δ_λ and Γ_λ were calculated. Figure 36 shows a plot of g_{po} for s-wave protons from which $\Delta_{\lambda po}$ is easily obtained. In the case of the 1028-kev state, $\Delta_{\lambda a_0 1}$ and $\Delta_{\lambda a_1 1}$ were shown to be negligible so $\Delta_\lambda \approx \Delta_{\lambda po}$ for both the 710 and 1028-kev states. The values of g_{po} are fairly well fitted with a linear function in energy over the region considered here so that the corrections provided by use of the more accurate resonance denominator

$$(E_\lambda + \Delta_\lambda - E)^2 + \frac{1}{4}\Gamma_\lambda^2$$

are negligible. Similarly, Γ_λ' was shown to be within about 10% of Γ_λ, but this calculation is quite sensitive to the nuclear radius assumed, and no corrections have been made for this effect because of the relatively small correction indicated.

APPENDIX VI--Sample Calculations

Part 1. Normalization of the cross section by use of equations 4, 5, 6, 7, 8, and 9

Equation 6 is used to calculate the Rutherford cross section for elastic scattering of 1.002 Mev protons from copper through a laboratory angle of $158^{\circ}20'$. From equation 7, θ_C is obtained first:

$$\sin(\theta_C - 158^{\circ}20') = \frac{1.008}{63.57} \sin(158^{\circ}20') = 0.0147$$

$$\theta_C - 158^{\circ}20' = 51'$$

$$\therefore \theta_C = 159^{\circ}11'$$

Then

$$\frac{d\sigma_R}{d\Omega_C} = 1.296 \left[\frac{29}{1.002}\left(\frac{64.58}{63.57}\right)\left(\frac{1}{0.9835}\right)^2\right]^2 \times 10^{-27} \frac{cm^2}{ster.}$$

$$= 1.197 \times 10^{-24} \frac{cm^2}{ster.} = 1.197 \text{ barns/ster.}$$

From equation 8,

$$\frac{\Omega_L}{\Omega_C} = \frac{\sqrt{1 - \left(\frac{1.008}{63.57}\right)^2 \sin^2(158^{\circ}20')}}{\left[\sqrt{1 - \left(\frac{1.008}{63.57}\right)^2 \sin^2(158^{\circ}20')} + \frac{1.008}{63.57}\cos(158^{\circ}20')\right]^2}$$

$$= 1.012$$

Therefore $\frac{d\sigma_R}{d\Omega_L} = 1.183$ barns/ster.

Now the thick target yield from copper scattering will be used in equation 5 in conjunction with this value of $\frac{d\sigma_R}{d\Omega_L}$ to evaluate the quantity $\frac{ZeR}{q\Omega_L}$. This involves the following values:

$Y_T = 51,060$ counts

$\varepsilon_1 = 12.37 \times 10^{-15}$ ev-cm^2

$\varepsilon_2 = 12.74 \times 10^{-15}$ ev-cm^2

$\frac{\partial E_2}{\partial E_1} = 0.941$

$E_{20} = 9.43 \times 10^5$ ev

$\theta_T = \theta'_T = 79^\circ 10'$

$$\frac{ZeR}{q\Omega_L} = \frac{d\sigma_R}{d\Omega_L} \frac{2E_{20}}{Y_T} \left[\varepsilon_1 \frac{\partial E_2}{\partial E_1} + \varepsilon_2 \left(\frac{\cos\theta_T}{\cos\theta'_T} \right) \right]^{-1}$$

$$= \frac{1.183 \times 10^{-24} \times 2 \times 9.43 \times 10^5}{5.106 \times 10^4} \left[12.37 \times 0.941 \times 10^{-15} + 12.74 \times 10^{-15} \right]^{-1}$$

$$= 1.792 \times 10^{-9} \text{ steradians}^{-1} \ *$$

The quantity n_T will now be calculated using equation 9. By graphical integration of the yield vs. energy plot, A was found equal to 2.01×10^7 "counts-ev". Also

$Y_{max} = 2940$ counts

$\xi = 52$ kev

$\Gamma = 2.2$ kev

$\varepsilon = 5.57 \times 10^{-14}$ ev-cm^2 per N^{15} nucleus

$x_2 = 9.0$

$x_1 = -7.1$

---

*Nominal values of the quantities involved in this measurement are $R = 292$, $\Omega = 3.1 \times 10^{-3}$ steradians, and $q = CV$ where $C = 1.0 \mu f$ and $V = 9.2$ volts, giving $ZeR/q\Omega_L = 1.64 \times 10^{-9}$ steradians^{-1}.

$$n_T = \frac{2.01 \times 10^7}{\tan^{-1}9.0 - \tan^{-1}(-7.1)} \times \frac{2\tan^{-1}(\frac{52}{2.2})}{5.57 \times 10^{-14} \times 2.940 \times 10^3}$$

$$n_T = 1.31 \times 10^{17} \quad N^{15} \text{ nuclei/cm}^2$$

The value obtained for $\int \frac{N(I)dI}{I}$ corresponding to the above n_T at $E = 1.100$ Mev and $\theta_L = 158^\circ 20'$ was 16.1. Equation 4 then gives

$$\frac{d\sigma}{d\Omega_L} = \frac{1.792 \times 10^{-9}}{1.31 \times 10^{17}} \times 16.1 \text{ cm}^2/\text{ster.}$$

$$= 2.19 \times 10^{-25} \text{ cm}^2/\text{ster.} = 219 \text{ millibarns/ster.}$$

Since $\frac{\Omega_L}{\Omega_C} = 1.137$ for $N^{15}(pp)N^{15}$ at $\theta_L = 158^\circ 20'$,

$\frac{d\sigma}{d\Omega_C} = 249$ mb/ster.

$\frac{d\sigma_R}{d\Omega_C} = 63.4$ mb/ster. for $N^{15}(pp)N^{15}$ at $\theta_L = 158^\circ 20'$

and $E = 1.100$ Mev, so

$$\frac{d\sigma/d\Omega_C}{d\sigma_R/d\Omega_C} = 3.92 \text{ at } \theta_L = 158^\circ 20' \text{ and } E = 1.100 \text{ Mev}$$

Part 2. Calculation of theoretical cross section at $\theta_L = 158^\circ 20'$, and $E = 1.100$ Mev

Equation 16 gives the expression for the cross section at this energy and this is

$$\frac{d\sigma/d\Omega_C}{d\sigma_R/d\Omega_C} - 1 = \left[\frac{\sin\xi}{k\sqrt{R}} - \frac{1}{2k^2R}\right](X-1) - \frac{\cos\xi}{k\sqrt{R}} Y - \frac{U}{4k^2R}$$

where $X = 1/4\, f_0 + 3/4\, f_1$

$Y = 1/4\, g_0 + 3/4\, g_1$

$$f_J = \cos 2\phi_J \left[1-2\frac{\Gamma_{psJ}}{\Gamma_J}\sin^2\delta_J\right] - \frac{2\Gamma_{psJ}}{\Gamma_J}\sin 2\phi_J \sin\delta_J\cos\delta_J$$

$$g_J = \sin 2\phi_J \left[1-2\frac{\Gamma_{psJ}}{\Gamma_J}\sin^2\delta_J\right] + \frac{2\Gamma_{psJ}}{\Gamma_J}\cos 2\phi_J \sin\delta_J\cos\delta_J$$

$$k^2 = \frac{2\mu^2 E_{LAB}}{\hbar^2 m_1} = \frac{2m_0^2 m_1 E_{LAB}}{\hbar^2(m_0+m_1)^2}$$

$$\frac{d\sigma_R}{d\Omega_C} = R = 1.296\left[\frac{Z_0 Z_1}{E_{LAB}}\frac{(m_0+m_1)}{m_0}\csc^2\frac{\theta_C}{2}\right]^2 \times 10^{-27}$$

$$k^2 R = \frac{2.592\, Z_0^2 Z_1^2 m_1}{\hbar^2 E_{LAB}}\csc^4\frac{\theta_C}{2} \times 10^{-27}$$

$$= \frac{2.592 \times 1 \times 49 \times 938.2 \times (1.0153)^4 \times 10^{-27}}{(1.973)^2 \times 10^{-22} \times 1.100}$$

$$= 0.2956$$

Therefore $k\sqrt{R} = 0.5437$

$$\xi = \frac{Z_0 Z_1 e^2}{\hbar v}\ln(\csc^2\frac{\theta_C}{2}) = \frac{Z_0 Z_1}{137}\left(\frac{c}{v}\right)\ln(\csc^2\frac{\theta_C}{2})$$

$$= \frac{1\times 7}{137}\sqrt{\frac{938.2}{2\times 1.100}}\ln(1.0153)^2$$

$$= 0.0322$$

Hence $\sin\xi = 0.0322$ and $\cos\xi = 0.9995$

$\phi_1 = \phi_0 = -12.9^\circ \Rightarrow \sin 2\phi_0 = -0.435$ and $\cos 2\phi_0 = 0.900$

$\delta_0 = \cot^{-1}\left(\frac{-390}{65.0}\right) \Rightarrow \sin\delta_0 = 0.163$ and $\cos\delta_0 = -0.987$

$$\delta_1 = \cot^{-1}\left(\frac{-72}{78.7}\right) \Rightarrow \sin\delta_1 = 0.738 \text{ and } \cos\delta_1 = -0.675$$

$$\frac{\Gamma_{ps0}}{\Gamma_0} = 1 \quad \text{and} \quad \frac{\Gamma_{ps1}}{\Gamma_1} = 0.82$$

$$f_0 = 0.900\left[1-2(0.163)^2\right] - 2 \times (-0.435)\times(0.163)\times(-0.987)$$

$$= 0.709$$

Similarly, $f_1 = -0.261$

$g_0 = -0.701$

$g_1 = -0.784$

and $X = -0.019$

$Y = -0.763$

From reference 5, $\sigma_{Reaction} = 145 \times 10^{-27} cm^2$ at 1.100 Mev.

Hence $U = \dfrac{\sigma_{Reaction}}{\pi \lambda^2} = \dfrac{\sigma_{Reaction}}{\pi} \times k^2$

$$U = \frac{145\times10^{-27}}{\pi} \times 2 \times \left(\frac{15}{16}\right)^2 \times \frac{938.2\times1.100}{(1.973)^2\times10^{-22}}$$

$U = 0.215$

$$\frac{d\sigma/d\Omega_C}{d\sigma_R/d\Omega_C} - 1 = \left[\frac{0.0322}{0.5437} - \frac{1}{2\times0.2956}\right]\left[-1.019\right] - \frac{0.9995\times(-0.763)}{0.5437}$$

$$- \frac{0.215}{4\times0.2956} = 1.663 + 1.403 - 0.181 = 2.885$$

Therefore, $\dfrac{d\sigma/d\Omega_C}{d\sigma_R/d\Omega_C} = 3.885$

REFERENCES

1. F. Ajzenberg and T. Lauritsen, Rev. Modern Phys. 27, 77 (1955)
2. L. A. Radicati, Phys. Rev. 87, 521 (1952)
3. Schardt, Fowler, and Lauritsen, Phys. Rev. 86, 527 (1952)
4. Kraus, French, Fowler, and Lauritsen, Phys. Rev. 89 299 (1953)
5. F. B. Hagedorn and J. B. Marion, Phys. Rev. (To be published)
6. H. A. Bethe, Rev. Modern Phys. 9, 69 (1937)
7. Ferguson, Clark, Gove, and Sample, Chalk River Project Report PD-261 (1956). Unpublished
8. G. W. Tautfest and S. Rubin, Phys. Rev. 103, 196 (1956)
9. R. E. Pixley, Private communication
10. Hagedorn, Mozer, Webb, Fowler, and Lauritsen, Phys. Rev. (To be published Jan. 1, 1957)
11. Thoneman, Moffatt, Roaf, and Sanders, Proc. Phys. Soc. London, 61, 483 (1948)
12. Webb, Hagedorn, Fowler, and Lauritsen, Phys. Rev. 99, 138 (1955)
13. J. B. Marion and F. B. Hagedorn, Phys. Rev. 104, 1028 (1956)
14. Smith, Parkins, and Forrester, Phys. Rev. 72, 989 (1947)
15. C. J. Zilverschoon, Ph.D. Thesis, University of Amsterdam (1954)
16. Evans, Stier, and Barnett, Phys. Rev. 90, 825 (1953)
17. T. S. Webb Jr., Ph.D. Thesis, Calif. Inst. of Tech. (1955)
18. S. Thulin, Arkiv F. Fys., Bd. 9 Nr. 11 (1955)

19. J. Seagrave, Phys. Rev., 85, 197 (1952)

20. E. A. Milne, Ph.D. Thesis, Calif. Inst. of Tech. (1953)

21. D. M. Yost, Private communication

22. W. Zimmerman, Jr., Phys. Rev. 104, 387 (1956)

23. Lauritsen, Lauritsen, and Fowler, Phys. Rev. 59, 241 (1941)

24. Fowler, Lauritsen, and Lauritsen, Rev. Sci. Inst. 18, 818 (1947)

25. Snyder, Rubin, Fowler, and Lauritsen, Rev. Sci. Inst. 21, 852 (1950)

26. W. D. Warters, Ph.D. Thesis, Calif. Inst. of Tech. (1953)

27. F. S. Mozer, Ph.D. Thesis, Calif. Inst. of Tech. (1956)

28. Herb, Snowden, and Sala, Phys. Rev. 75, 246 (1949)

29. C. A. Barnes, Phys. Rev. 97, 1226 (1955)

30. C. A. Barnes, Private communication

31. Laubenstein, Laubenstein, Koester, and Mobley, Phys. Rev. 84, 12 (1951)

32. Eppling, Cameron, Davis, Divatia, Galonsky, Goldberg, and Hill, Phys. Rev. 91, 438A (1953)

33. R. F. Christy, Physica, To be published. Report on Amsterdam Conference (1956)

34. J. M. Blatt and L. C. Biedenharn, Rev. Modern Phys. 24, 258 (1952)

35. J. M. Blatt and V. F. Weisskopf, Theoretical Nuclear Physics, John Wiley and Sons, New York (1952)

36. E. U. Condon and G. H. Shortley, The Theory of Atomic Spectra, Cambridge University Press, Cambridge (1951)

37. E. P. Wigner, Phys. Rev. 98, 145 (1955)

38. E. P. Wigner and L. Eisenbud, Phys. Rev. 72, 29 (1947)

39. R. G. Thomas, Phys. Rev. 81, 148 (1951)

40. R. W. Kavanagh, Ph.D. Thesis, Calif. Inst. of Tech (1956)

41. G. A. Jones and D. H. Wilkinson, Phys. Rev. 90, 722 (1953)

42. D. H. Wilkinson, Phys. Rev. 90, 721 (1953)

43. Barnes, James, and Neilson, Can. J. of Phys. 30, 717 (1952)

44. J. Seed and A. P. French, Phys. Rev. 88, 1007 (1952)

45. A. A. Kraus, Jr., Phys. Rev. 94, 975 (1954)

46. R. F. Christy and R. Latter, Rev. Modern Phys. 20, 185 (1948)

47. Bloch, Hull, Broyles, Bouricius, Freeman, and Breit, Rev. Modern Phys. 23, 147 (1951)

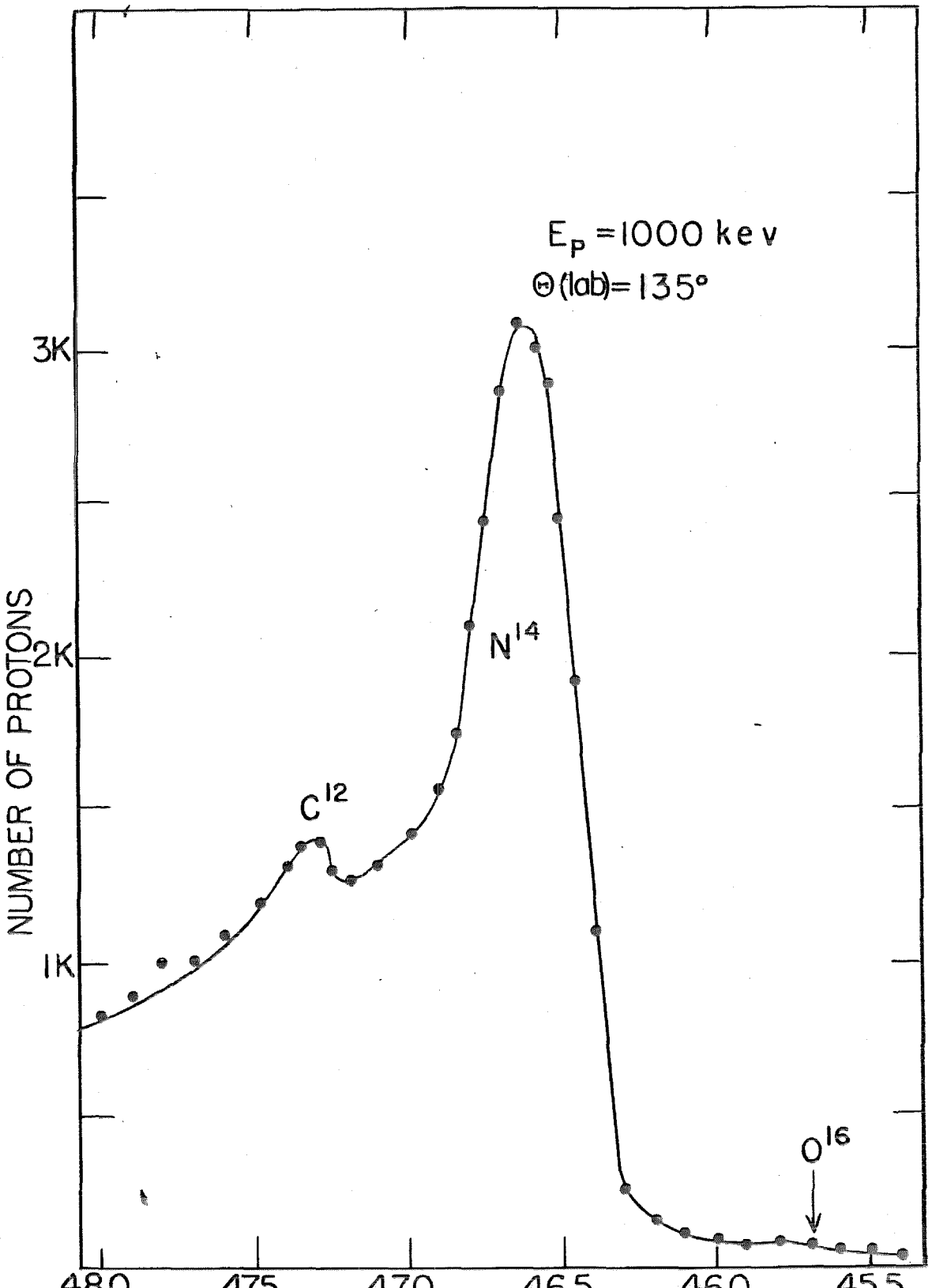
E_p = 1000 kev
Θ(lab) = 135°
3K
2K
1K
NUMBER OF PROTONS
C^{12}
N^{14}
O^{16}
48.0
47.5
47.0
46.5
46.0
45.5
INVERSE MOMENTUM (ARBITRARY UNITS)

FIGURE 1

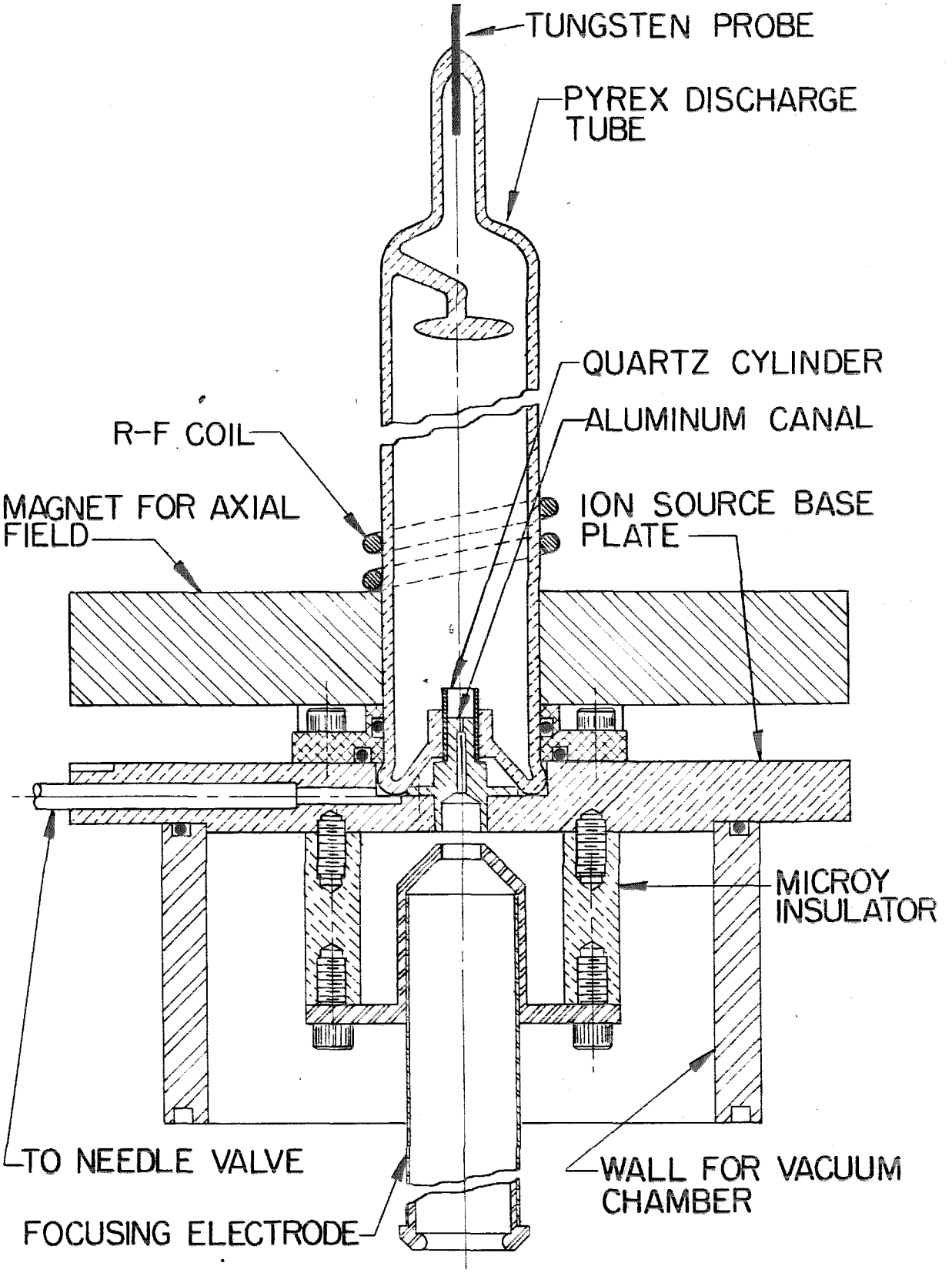

ION SOURCE AND FOCUSING SYSTEM

FIGURE 2

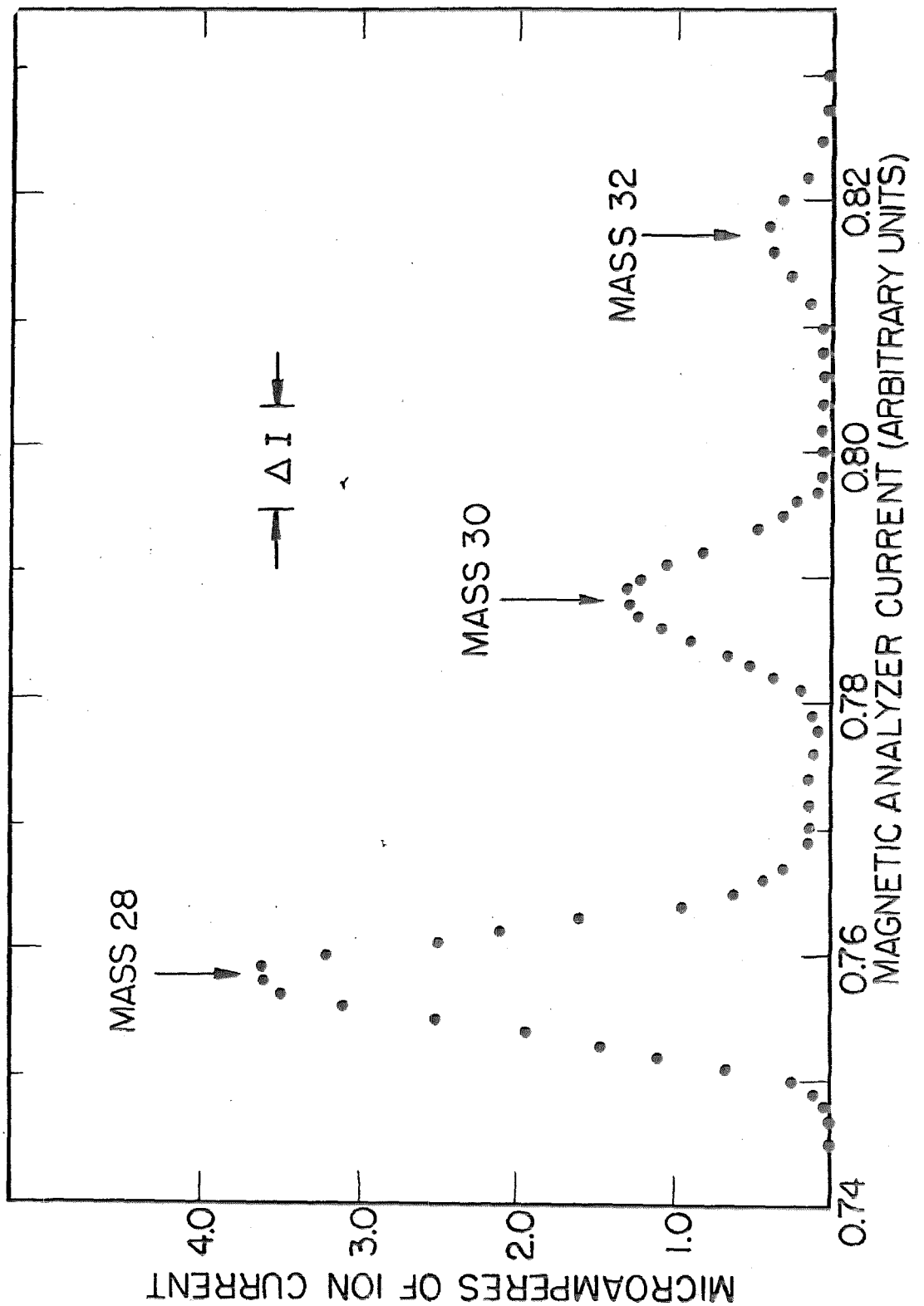
MICROAMPERES OF ION CURRENT
4.0
3.0
2.0
1.0
0.74
0.76
0.78
0.80
0.82
MAGNETIC ANALYZER CURRENT (ARBITRARY UNITS)
MASS 28
MASS 30
MASS 32
ΔI

FIGURE 3

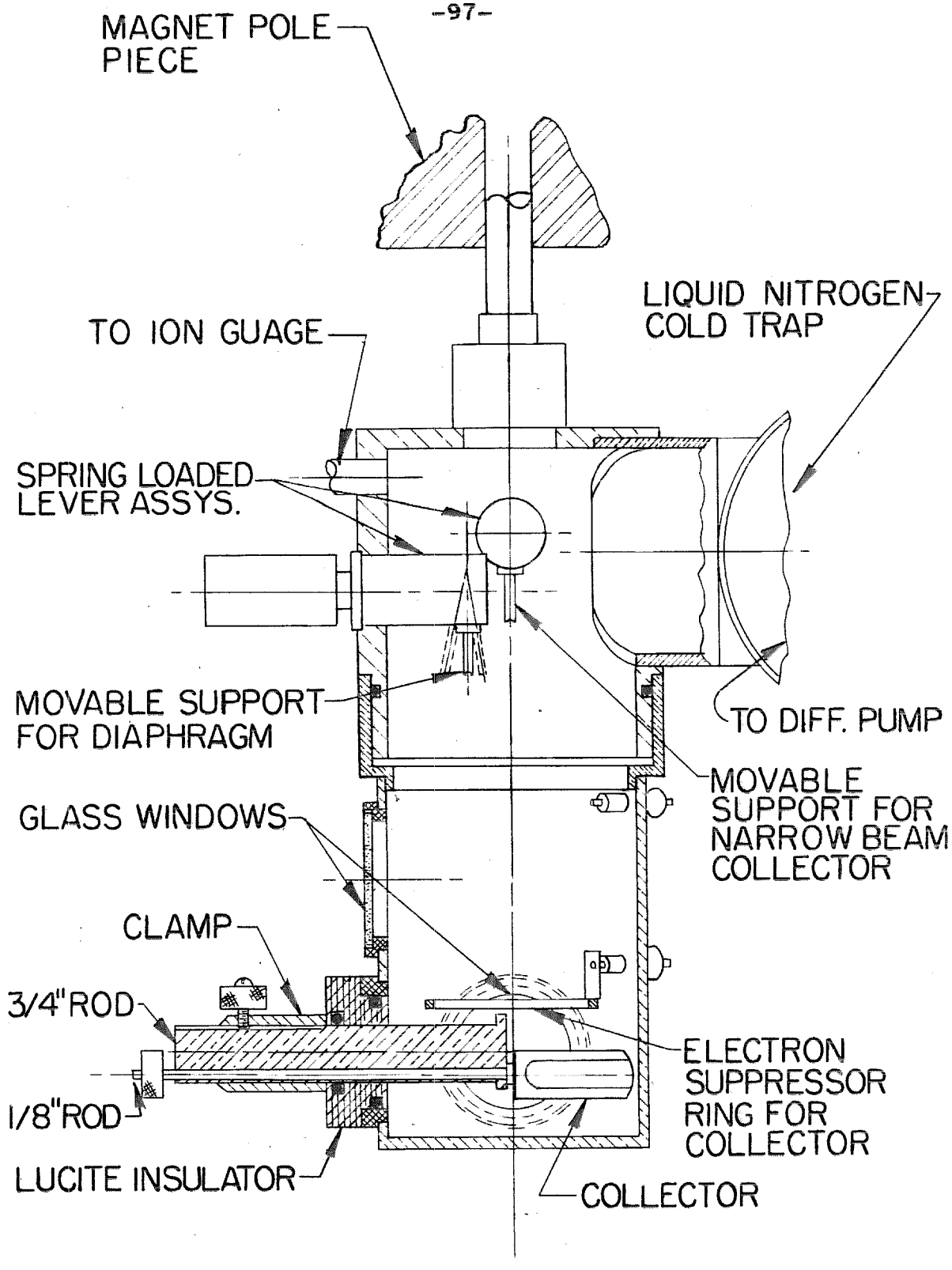

ISOTOPE SEPARATOR COLLECTOR CHAMBER

(ONE-HALF ACTUAL SIZE)

FIGURE 4

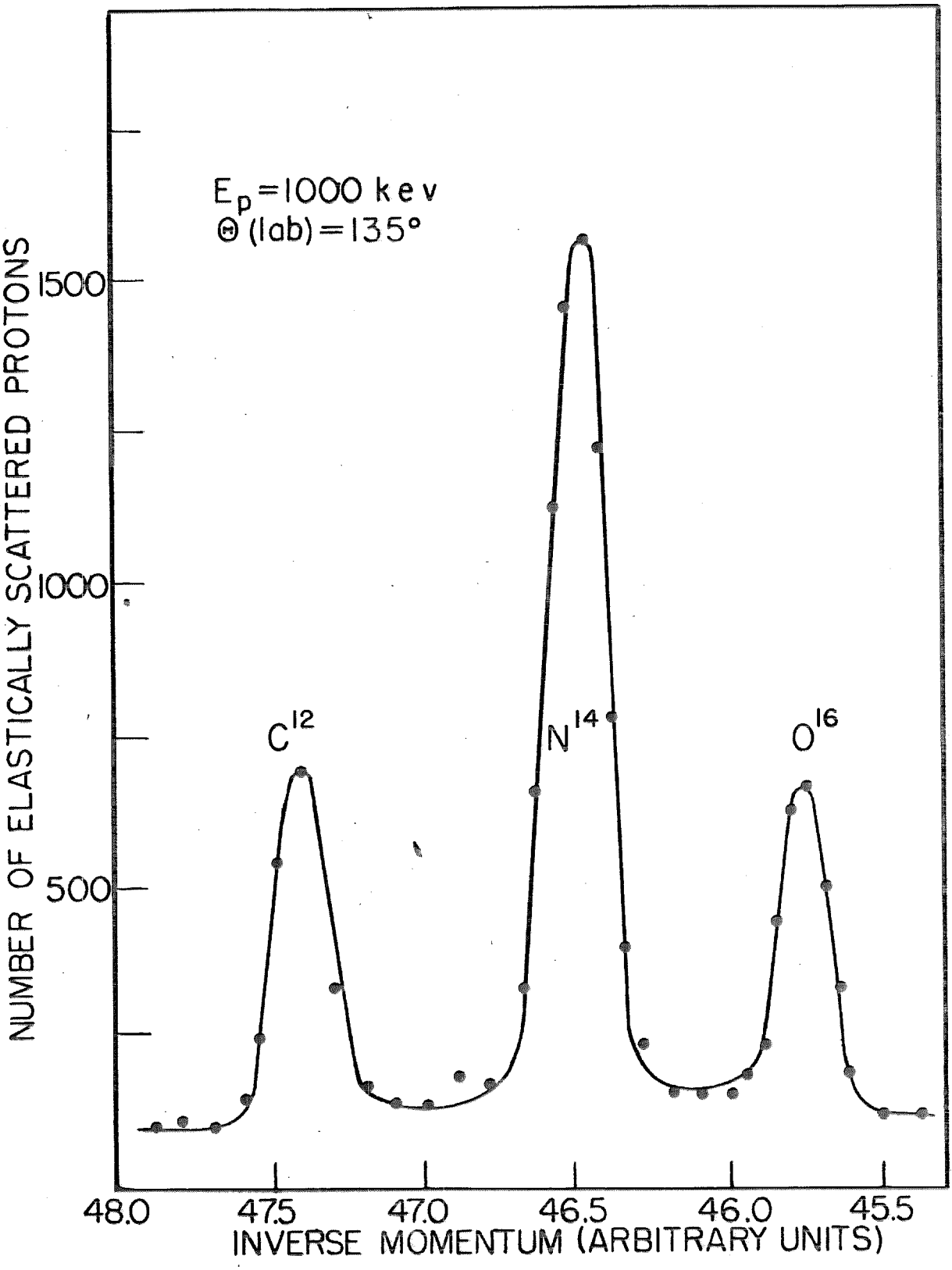
E_p = 1000 kev
Θ (lab) = 135°
NUMBER OF ELASTICALLY SCATTERED PROTONS
1500
1000
500
C^{12}
N^{14}
O^{16}
48.0
47.5
47.0
46.5
46.0
45.5
INVERSE MOMENTUM (ARBITRARY UNITS)

FIGURE 5

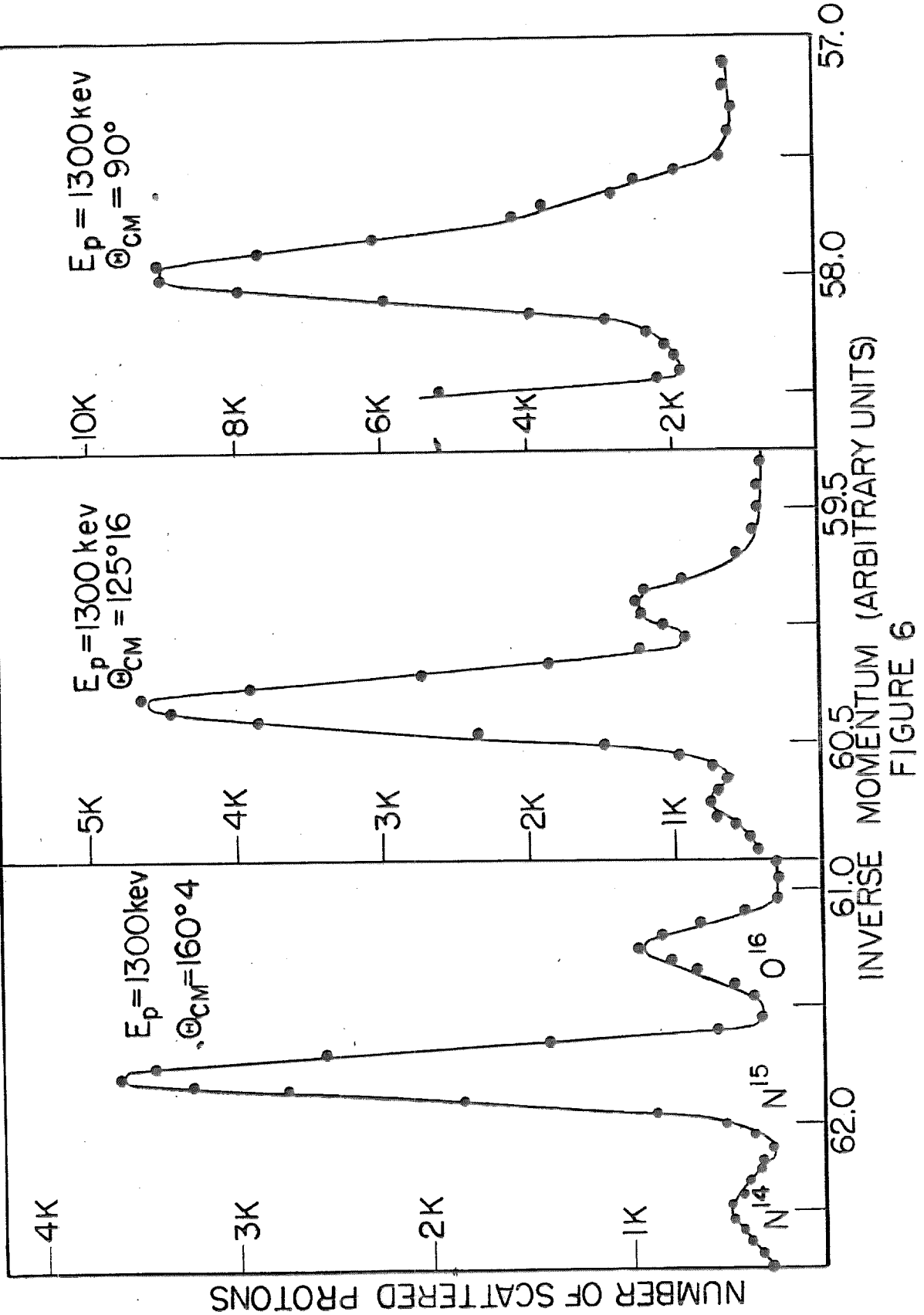
NUMBER OF SCATTERED PROTONS
4K
3K
2K
1K
N^{14}
N^{15}
O^{16}
E_p=1300kev
Θ_{CM}=160°4
5K
4K
3K
2K
1K
E_p=1300 kev
Θ_{CM} =125°16
10K
8K
6K
4K
2K
E_p = 1300kev
Θ_{CM} = 90°
62.0
61.0
60.5
59.5
58.0
57.0
INVERSE MOMENTUM (ARBITRARY UNITS)

FIGURE 6

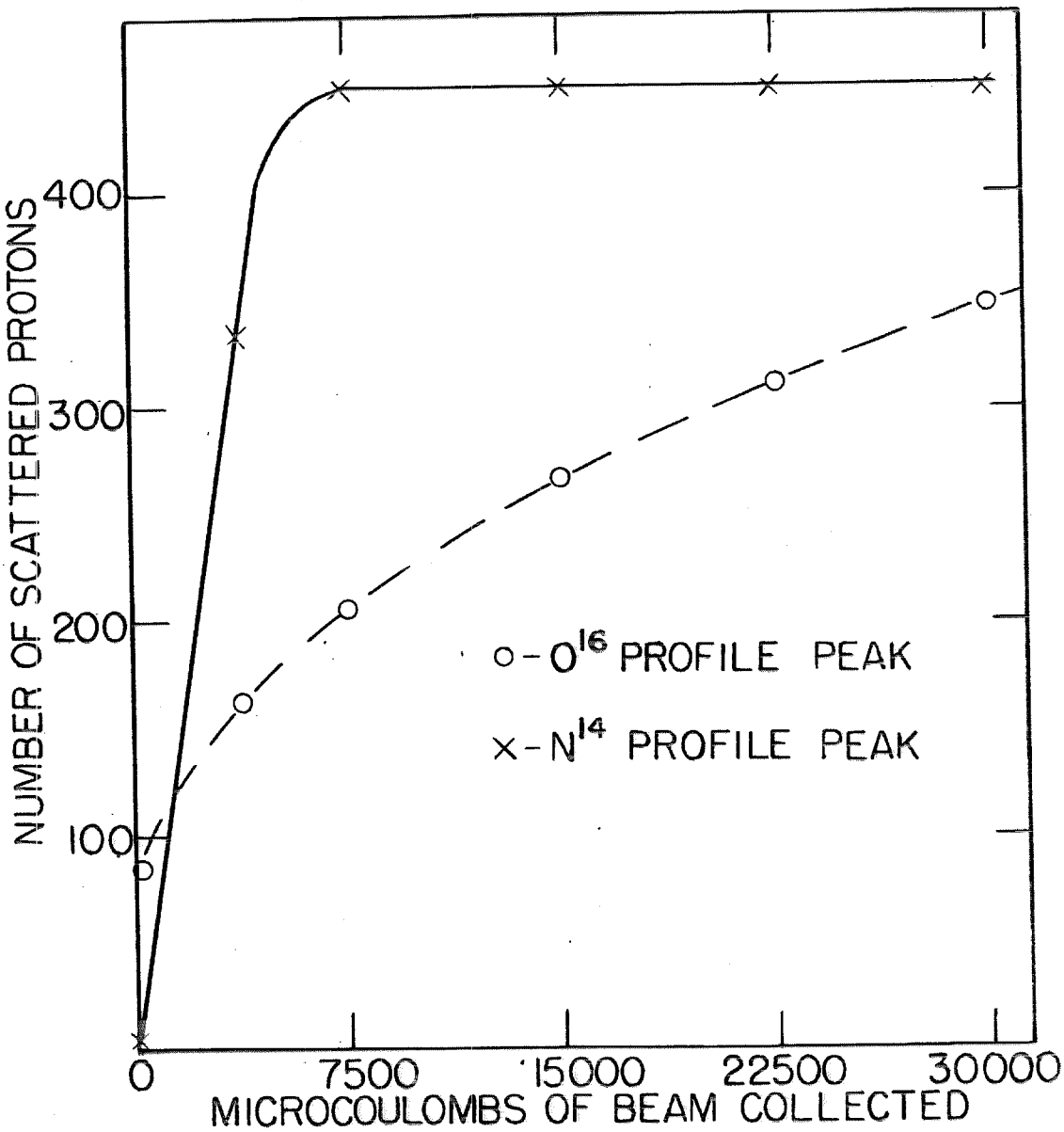
NUMBER OF SCATTERED PROTONS
400
300
200
100
0
7500
15000
22500
30000
MICROCOULOMBS OF BEAM COLLECTED
o - O16 PROFILE PEAK
x - N14 PROFILE PEAK

FIGURE 7

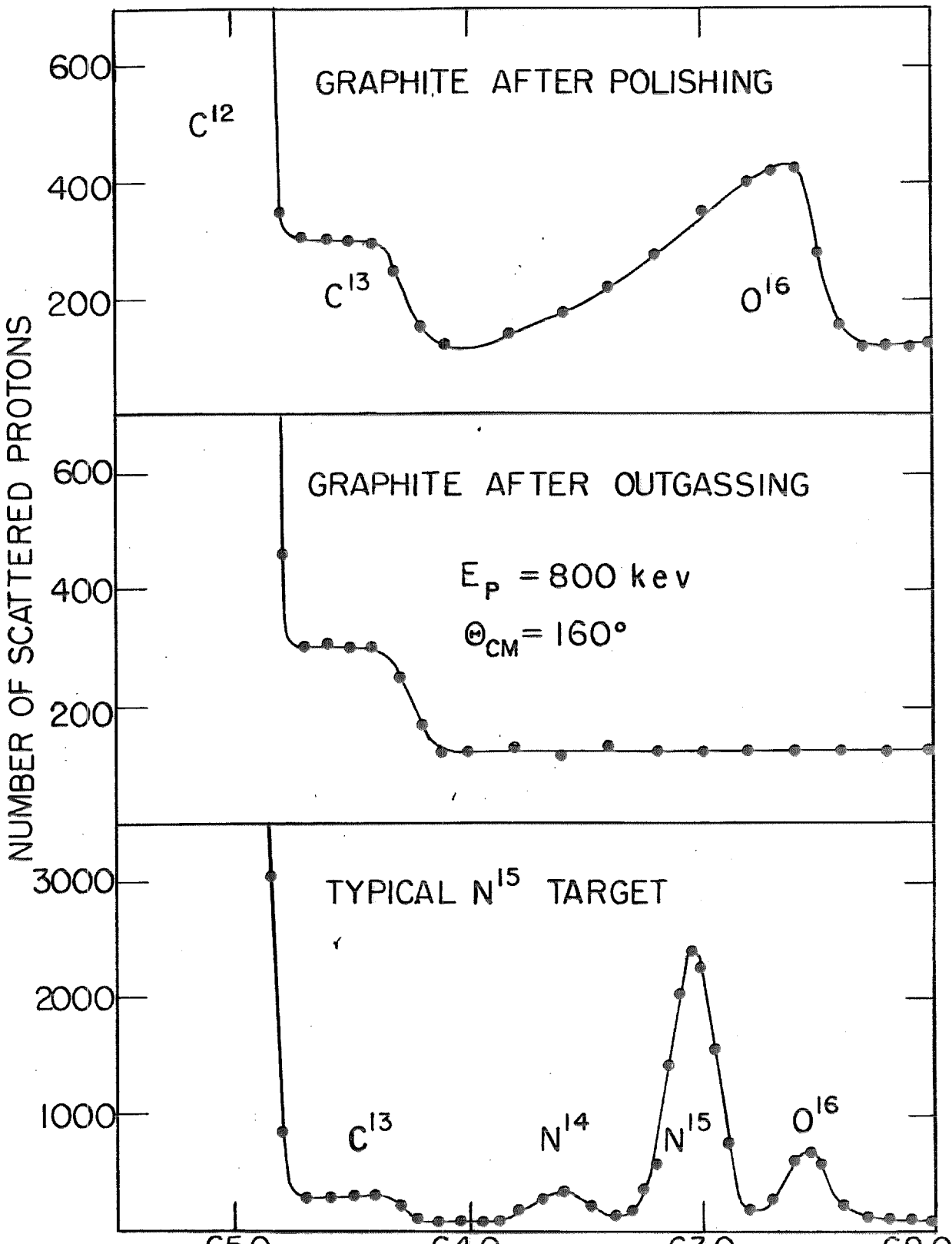
GRAPHITE AFTER POLISHING
C12
C13
O16
GRAPHITE AFTER OUTGASSING
Ep = 800 kev
ΘCM = 160°
TYPICAL N15 TARGET
C13
N14
N15
O16
600
400
200
3000
2000
1000
NUMBER OF SCATTERED PROTONS
65.0
64.0
63.0
62.0
INVERSE MOMENTUM (ARBITRARY UNITS)

FIGURE 8

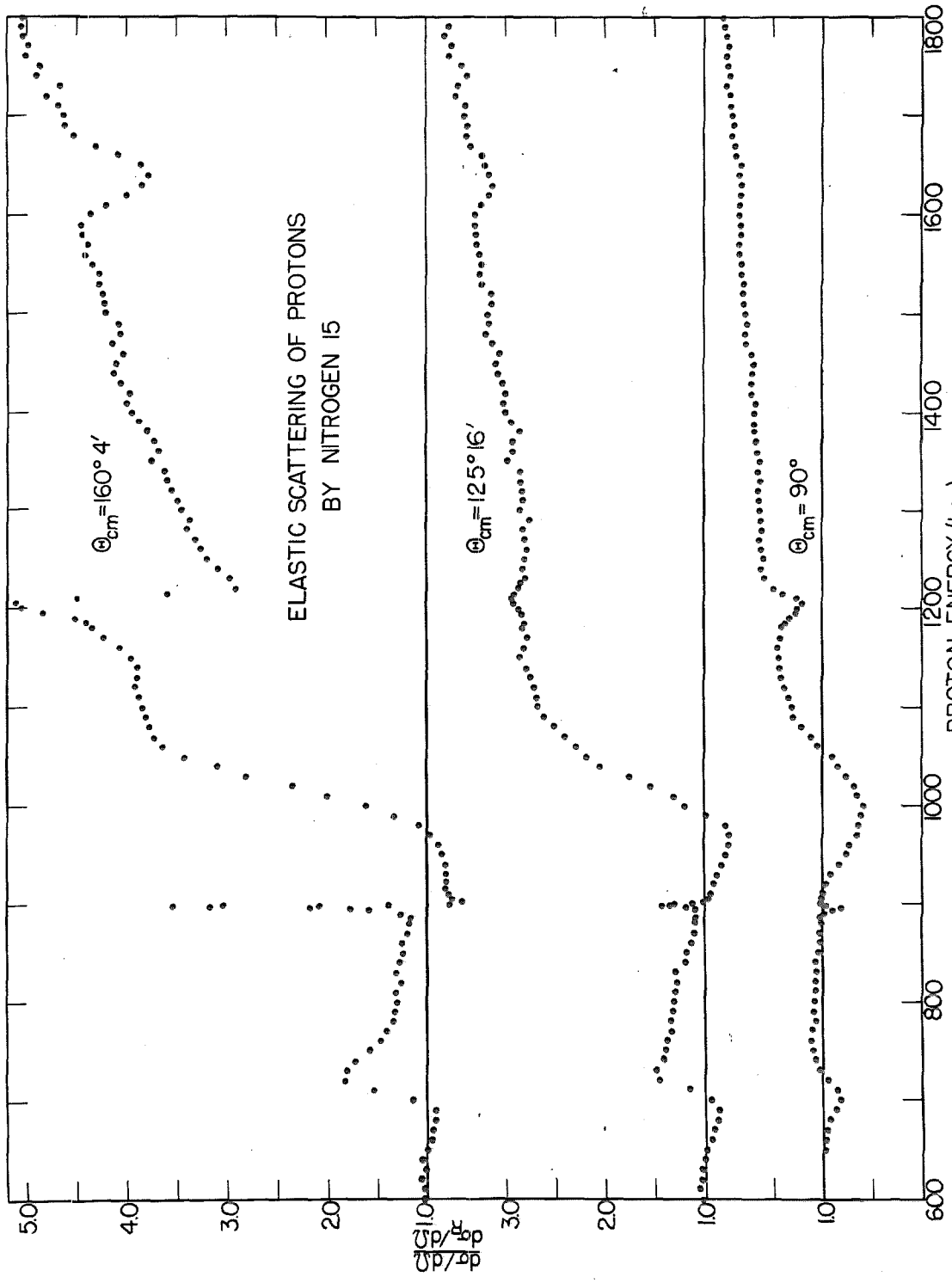
ELASTIC SCATTERING OF PROTONS
BY NITROGEN 15
Θ_{cm}=160° 4'
Θ_{cm}=125° 16'
Θ_{cm}= 90°
$d\sigma/d\Omega$
$d\sigma/d\Omega_p$
5.0
4.0
3.0
2.0
1.0
3.0
2.0
1.0
1.0
600
800
1000
1200
1400
1600
1800
PROTON ENERGY (kev)

FIGURE 9

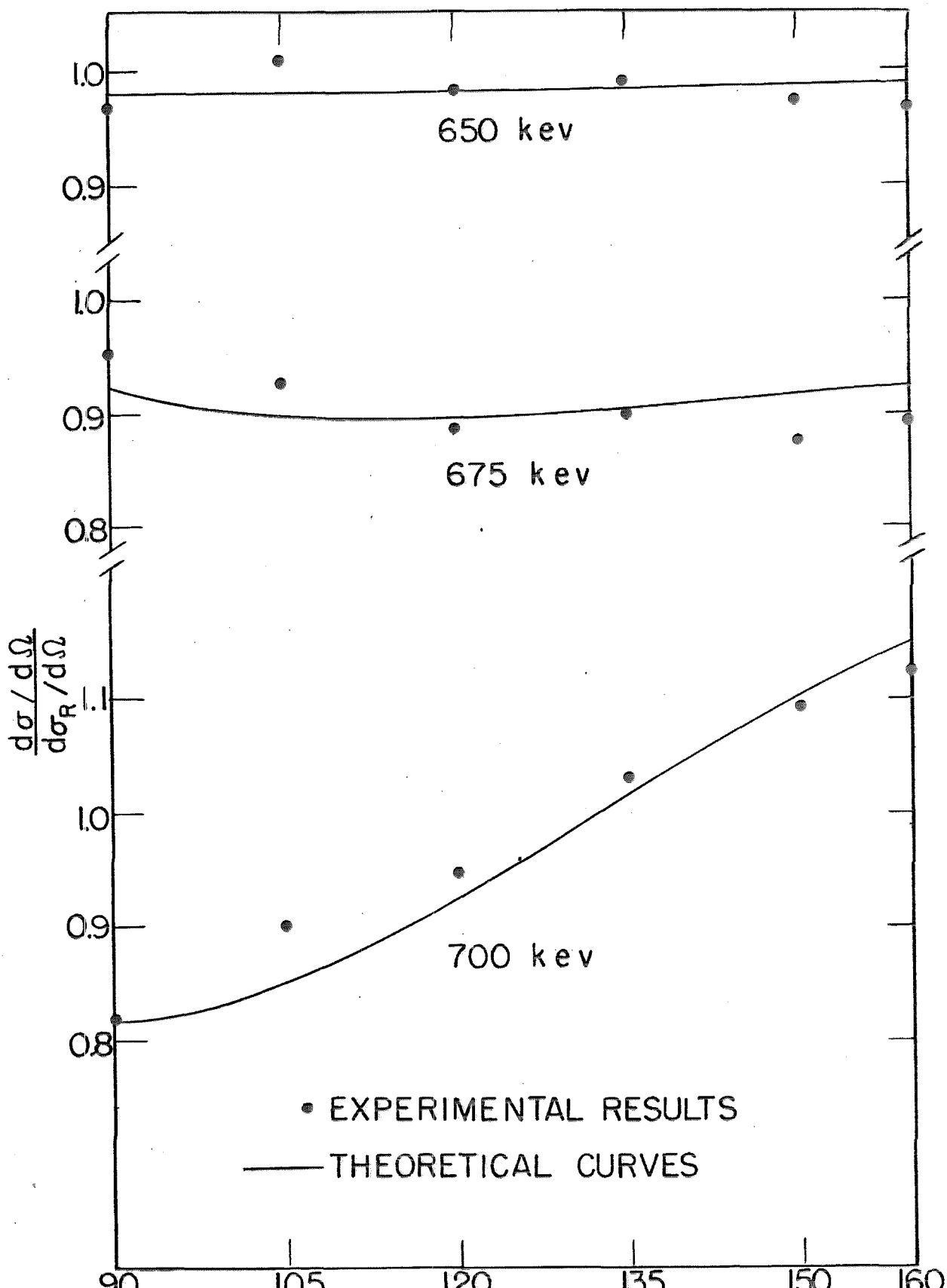
1.0
650 kev
0.9
1.0
0.9
675 kev
0.8
dσ/dΩ / dσR/dΩ
1.1
1.0
0.9
700 kev
0.8
• EXPERIMENTAL RESULTS
—— THEORETICAL CURVES
90
105
120
135
150
160
CENTER-OF-MASS ANGLE (DEGREES)

FIGURE 10

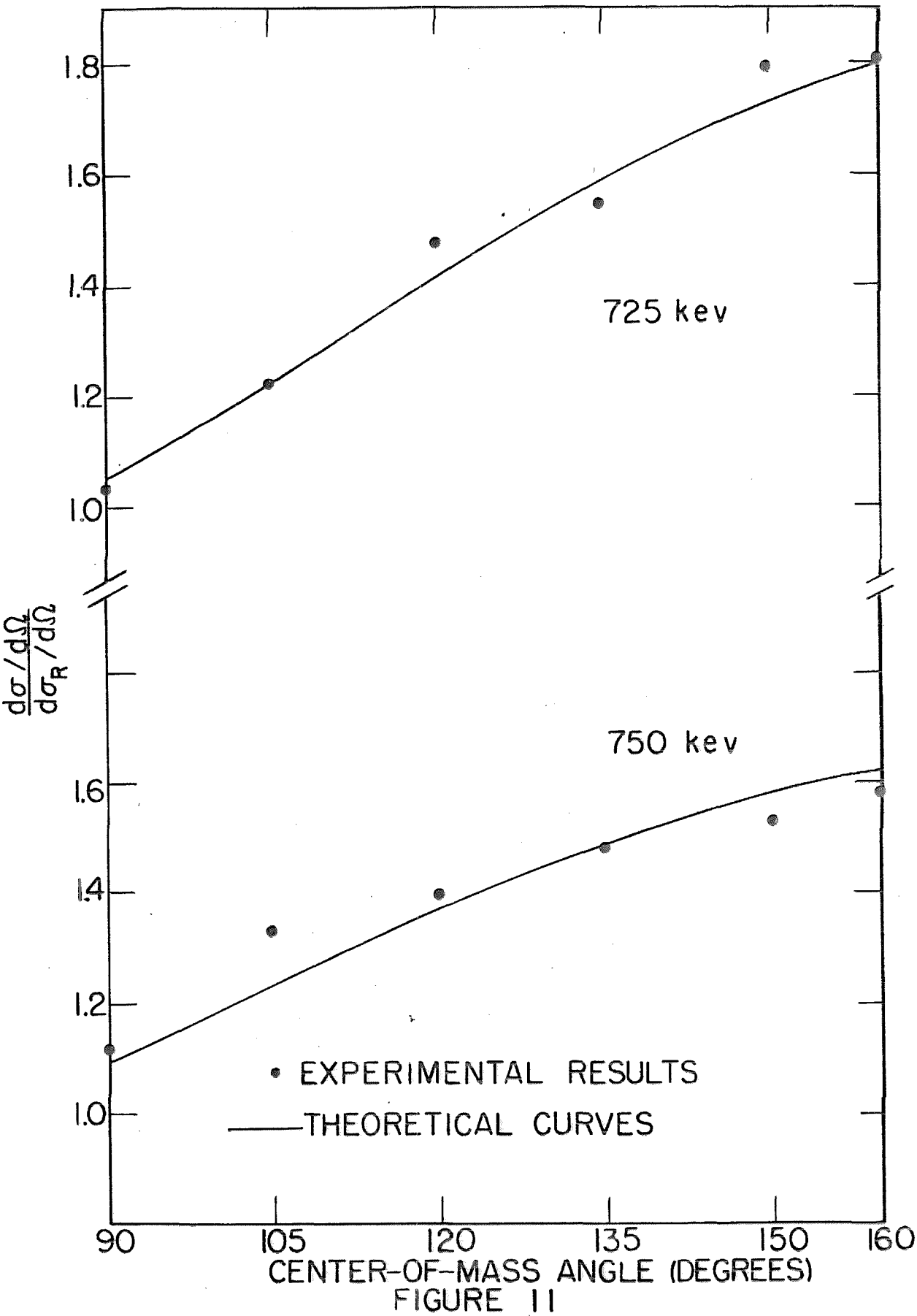
1.8
1.6
1.4
1.2
1.0
725 kev
750 kev
1.6
1.4
1.2
1.0
$\frac{d\sigma/d\Omega}{d\sigma_R/d\Omega}$
• EXPERIMENTAL RESULTS
——THEORETICAL CURVES
90
105
120
135
150
160
CENTER-OF-MASS ANGLE (DEGREES)

FIGURE 11

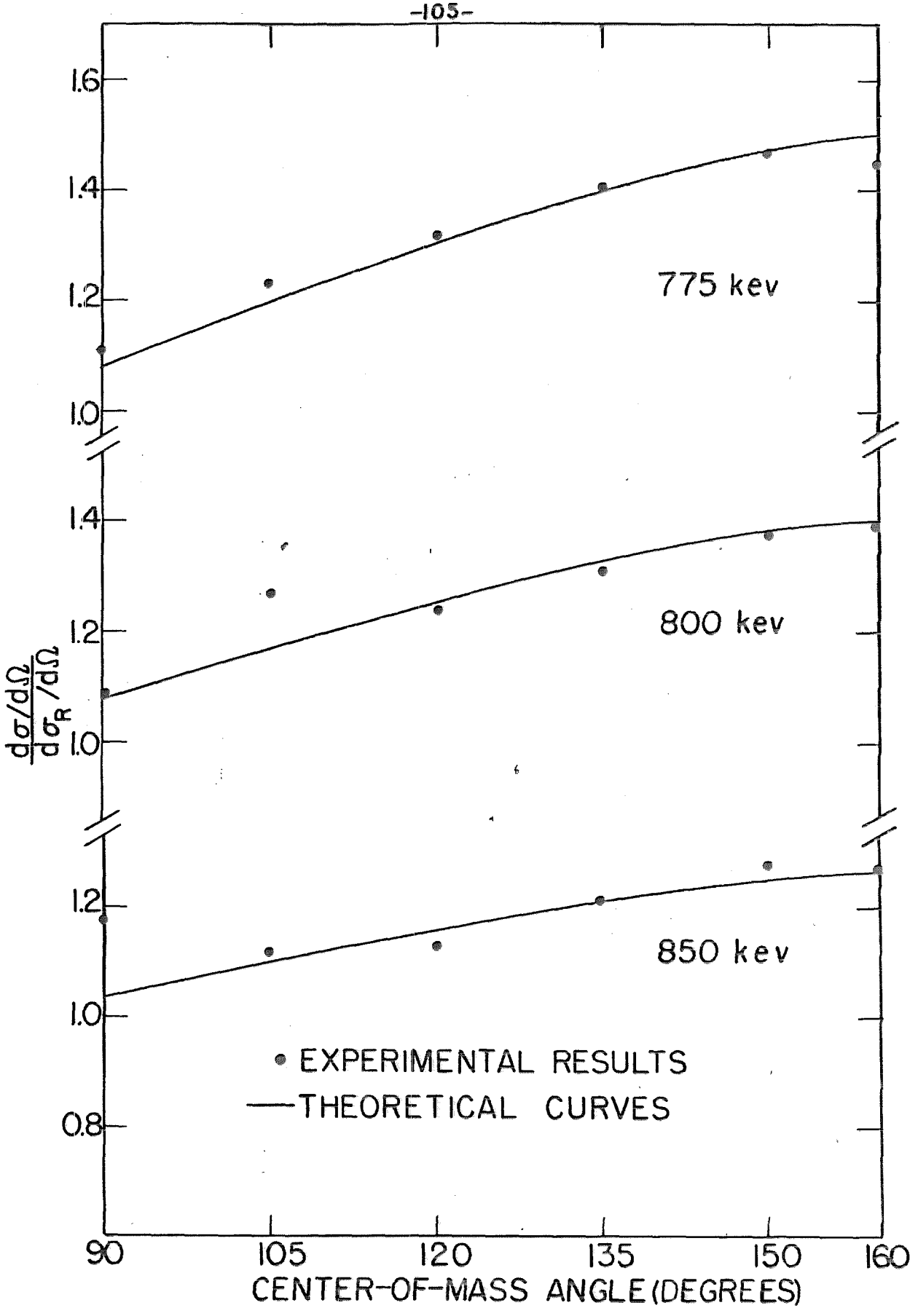
1.6
1.4
1.2
1.0
775 kev
1.4
1.2
1.0
800 kev
1.2
1.0
0.8
850 kev
$\frac{d\sigma/d\Omega}{d\sigma_R/d\Omega}$
• EXPERIMENTAL RESULTS
—THEORETICAL CURVES
90
105
120
135
150
160
CENTER-OF-MASS ANGLE (DEGREES)

FIGURE 12

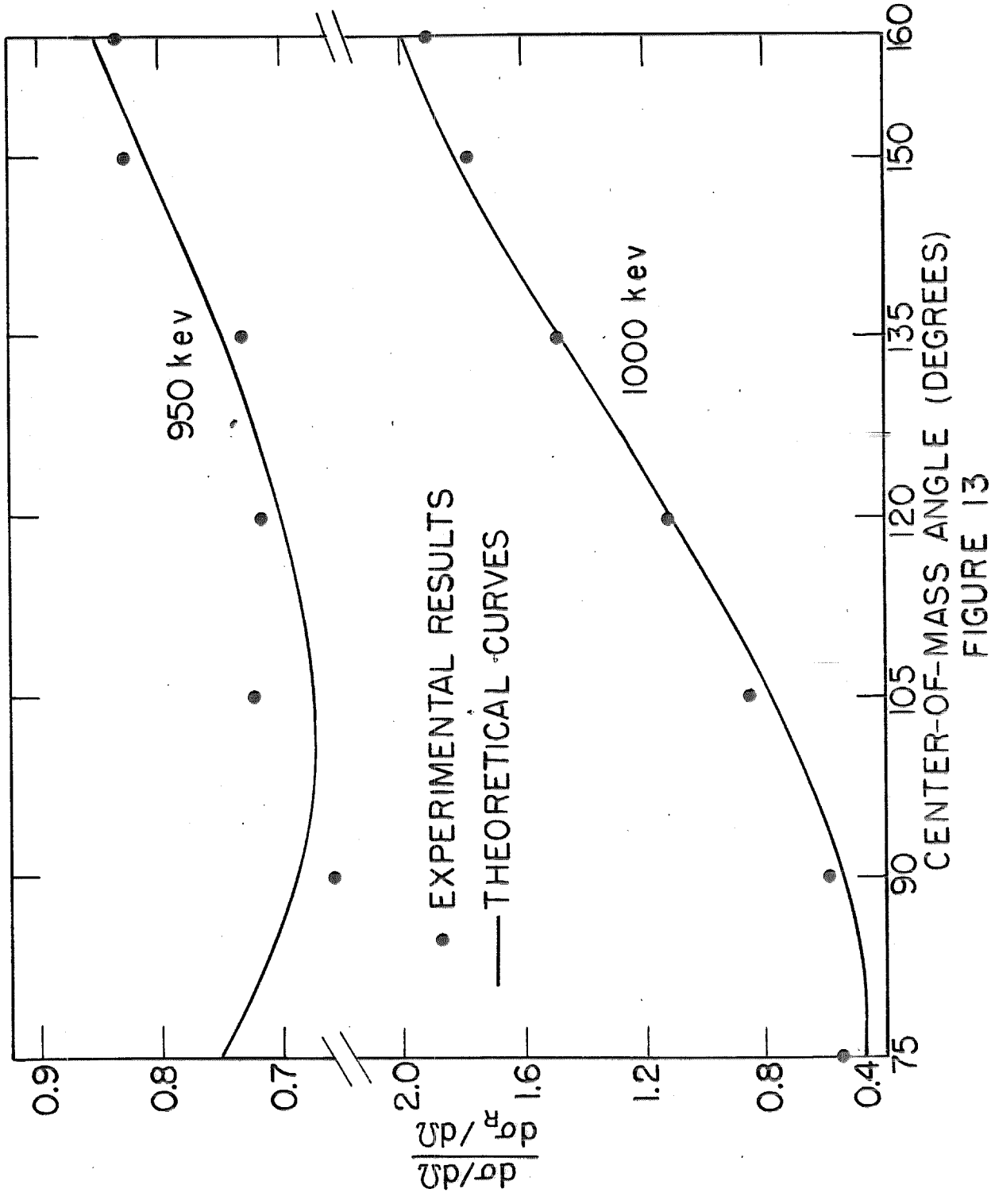
950 kev
1000 kev
• EXPERIMENTAL RESULTS
— THEORETICAL CURVES
$\frac{d\sigma/d\Omega}{d\sigma_R/d\Omega}$
0.9
0.8
0.7
2.0
1.6
1.2
0.8
0.4
75
90
105
120
135
150
160
CENTER-OF-MASS ANGLE (DEGREES)

FIGURE 13

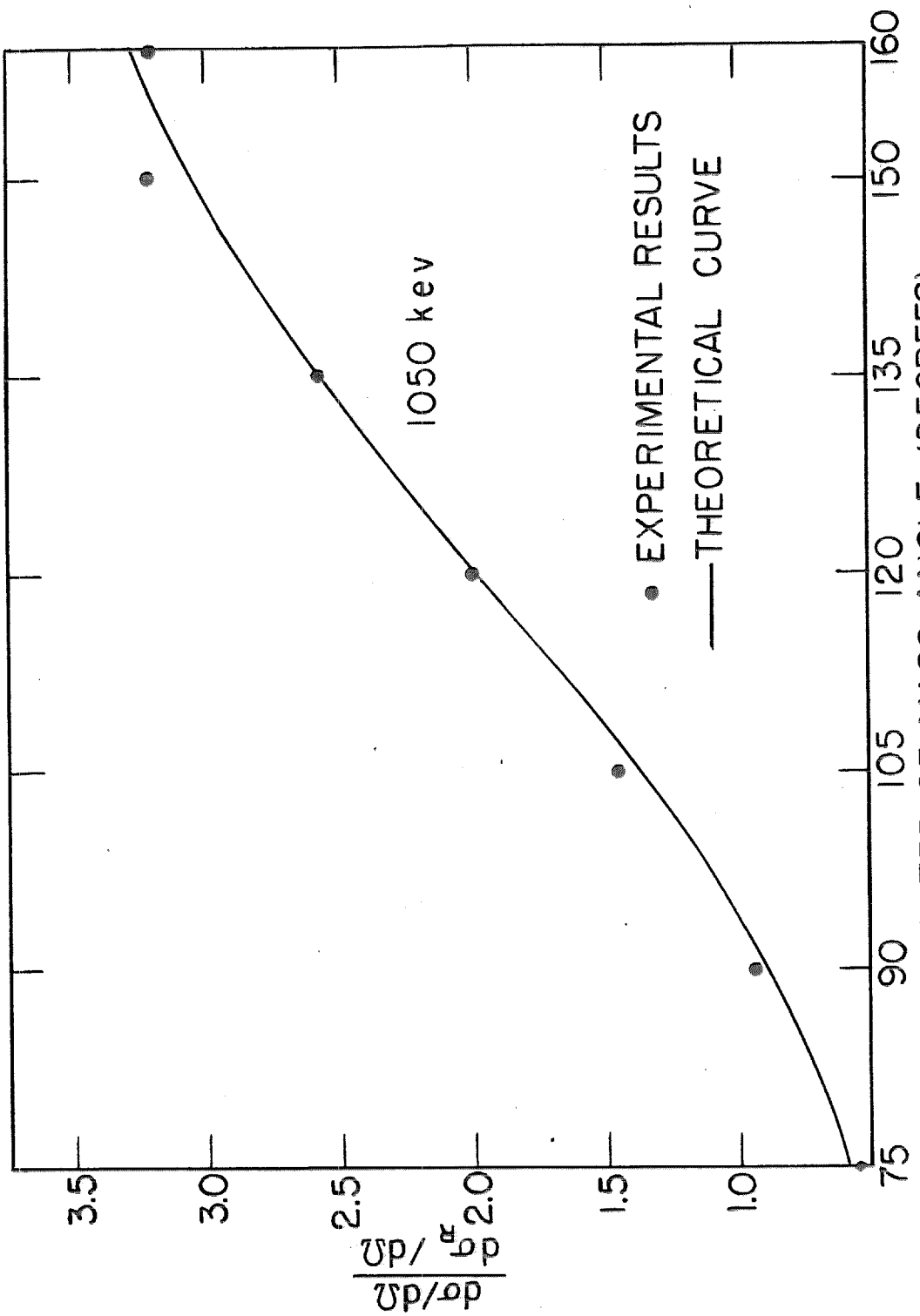
1050 kev
EXPERIMENTAL RESULTS
THEORETICAL CURVE
$\frac{d\sigma/d\Omega}{d\sigma_R/d\Omega}$
3.5
3.0
2.5
2.0
1.5
1.0
75
90
105
120
135
150
160
CENTER-OF-MASS ANGLE (DEGREES)

FIGURE 14

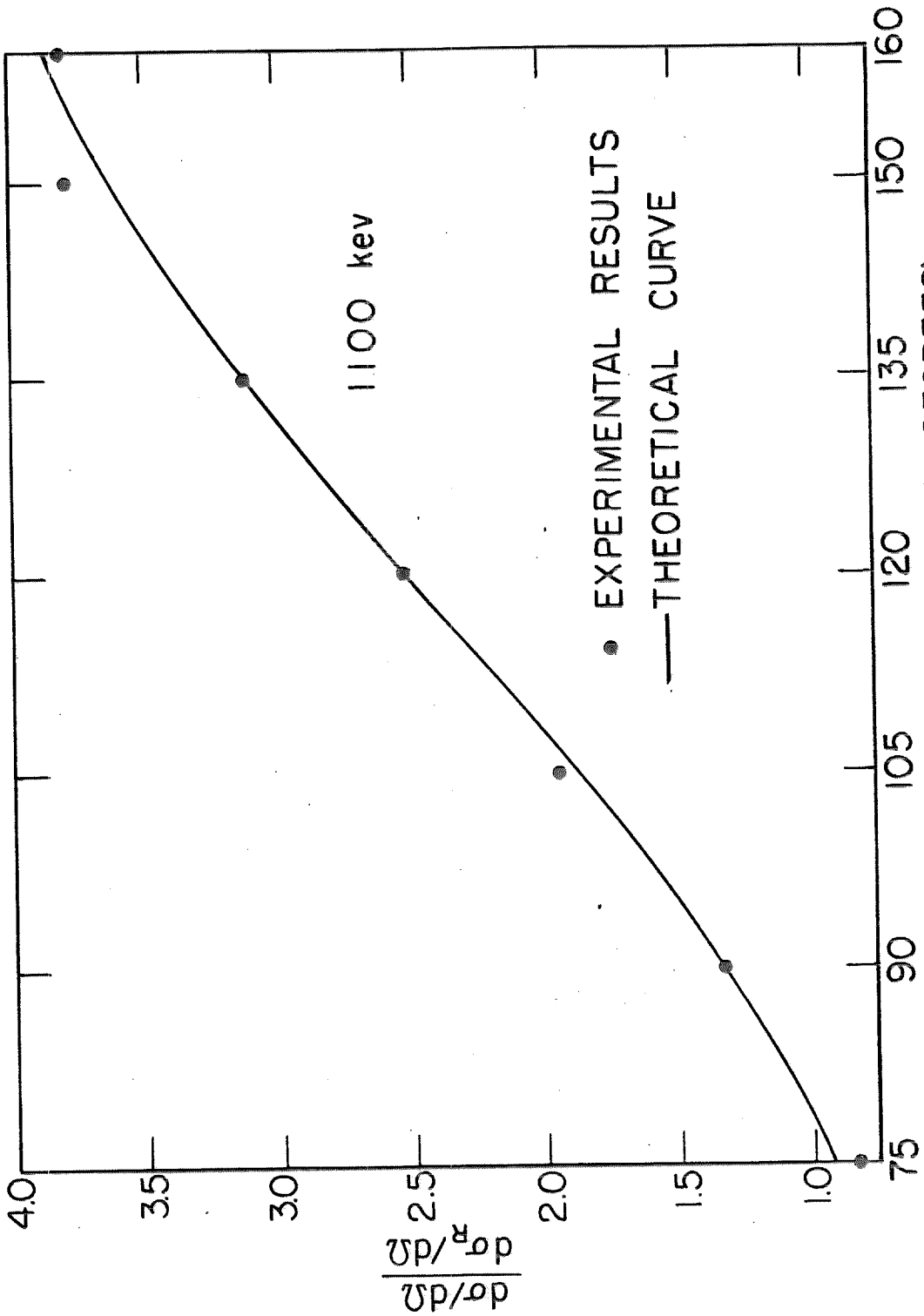
1100 kev
EXPERIMENTAL RESULTS
THEORETICAL CURVE
dσ/dΩ / dσR/dΩ
4.0
3.5
3.0
2.5
2.0
1.5
1.0
75
90
105
120
135
150
160
CENTER-OF-MASS ANGLE (DEGREES)

FIGURE 15

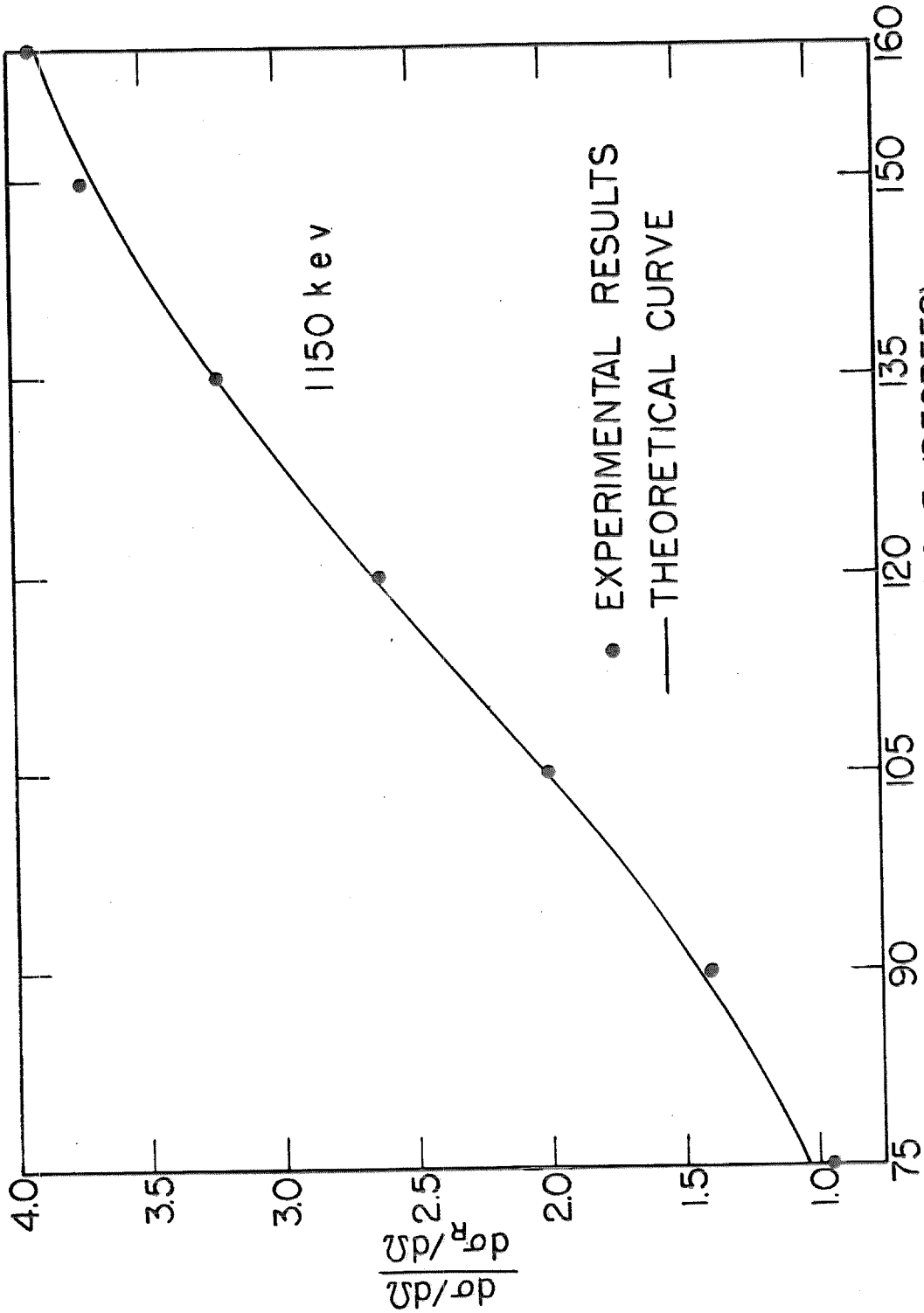
1150 kev
EXPERIMENTAL RESULTS
THEORETICAL CURVE
dσ/dΩ / dσR/dΩ
CENTER-OF-MASS ANGLE (DEGREES)
4.0
3.5
3.0
2.5
2.0
1.5
1.0
75
90
105
120
135
150
160

FIGURE 16

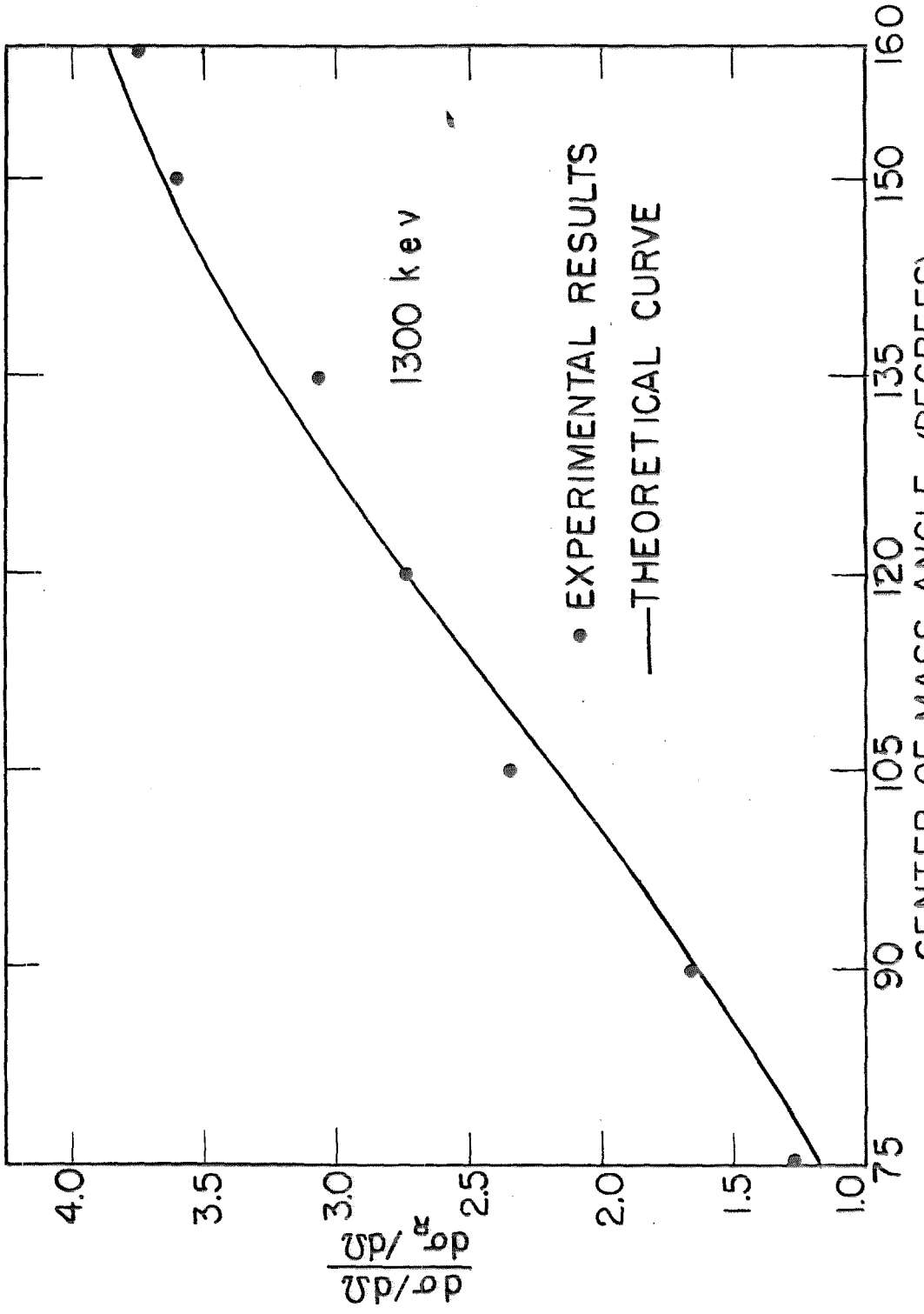
1300 kev
• EXPERIMENTAL RESULTS
—THEORETICAL CURVE
$\frac{d\sigma/d\Omega}{d\sigma_R/d\Omega}$
4.0
3.5
3.0
2.5
2.0
1.5
1.0
75
90
105
120
135
150
160
CENTER-OF-MASS ANGLE (DEGREES)

FIGURE 17

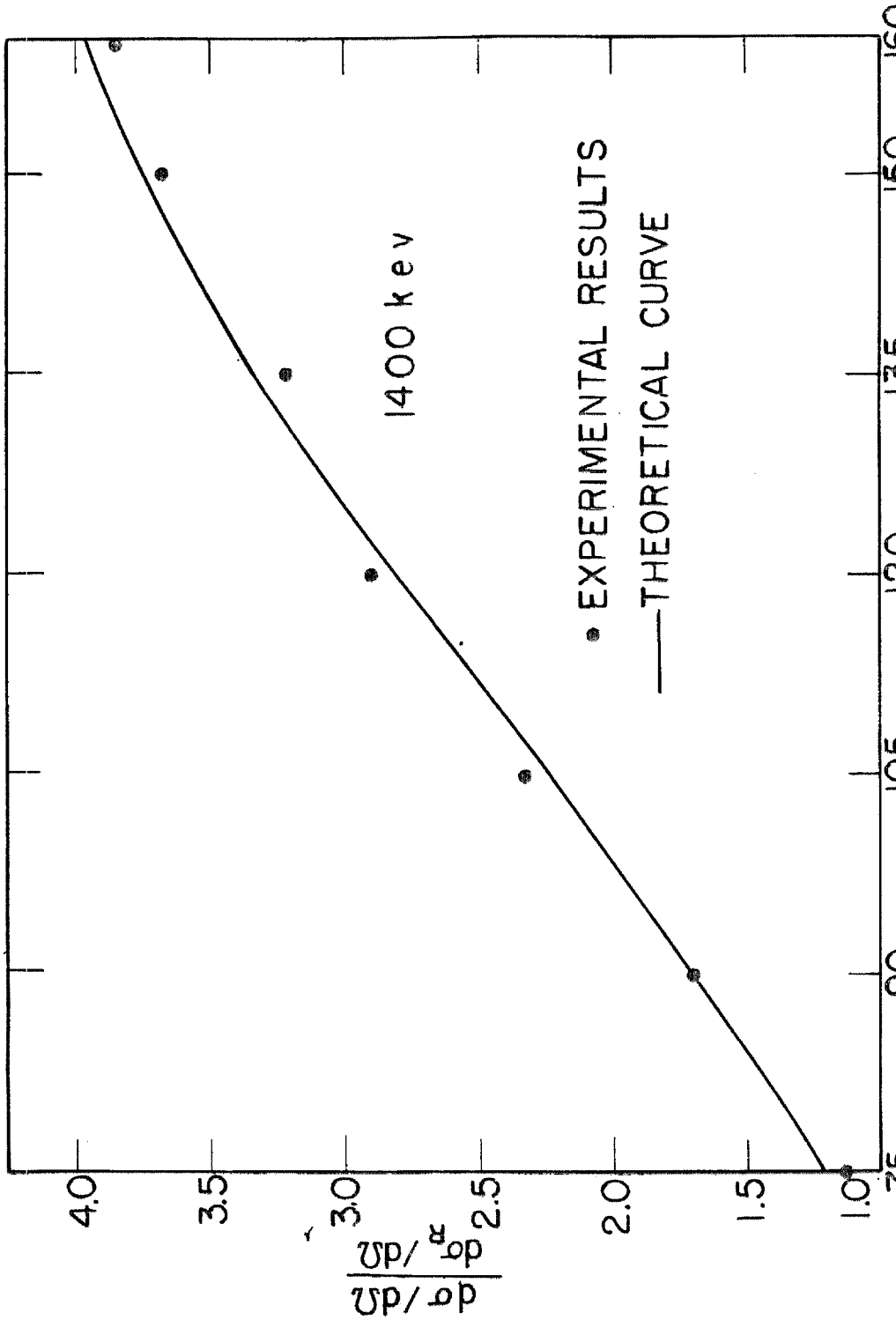
1400 kev
• EXPERIMENTAL RESULTS
—THEORETICAL CURVE
$\frac{d\sigma/d\Omega}{d\sigma_R/d\Omega}$
4.0
3.5
3.0
2.5
2.0
1.5
1.0
75
90
105
120
135
150
160
CENTER-OF-MASS ANGLE (DEGREES)

FIGURE 18

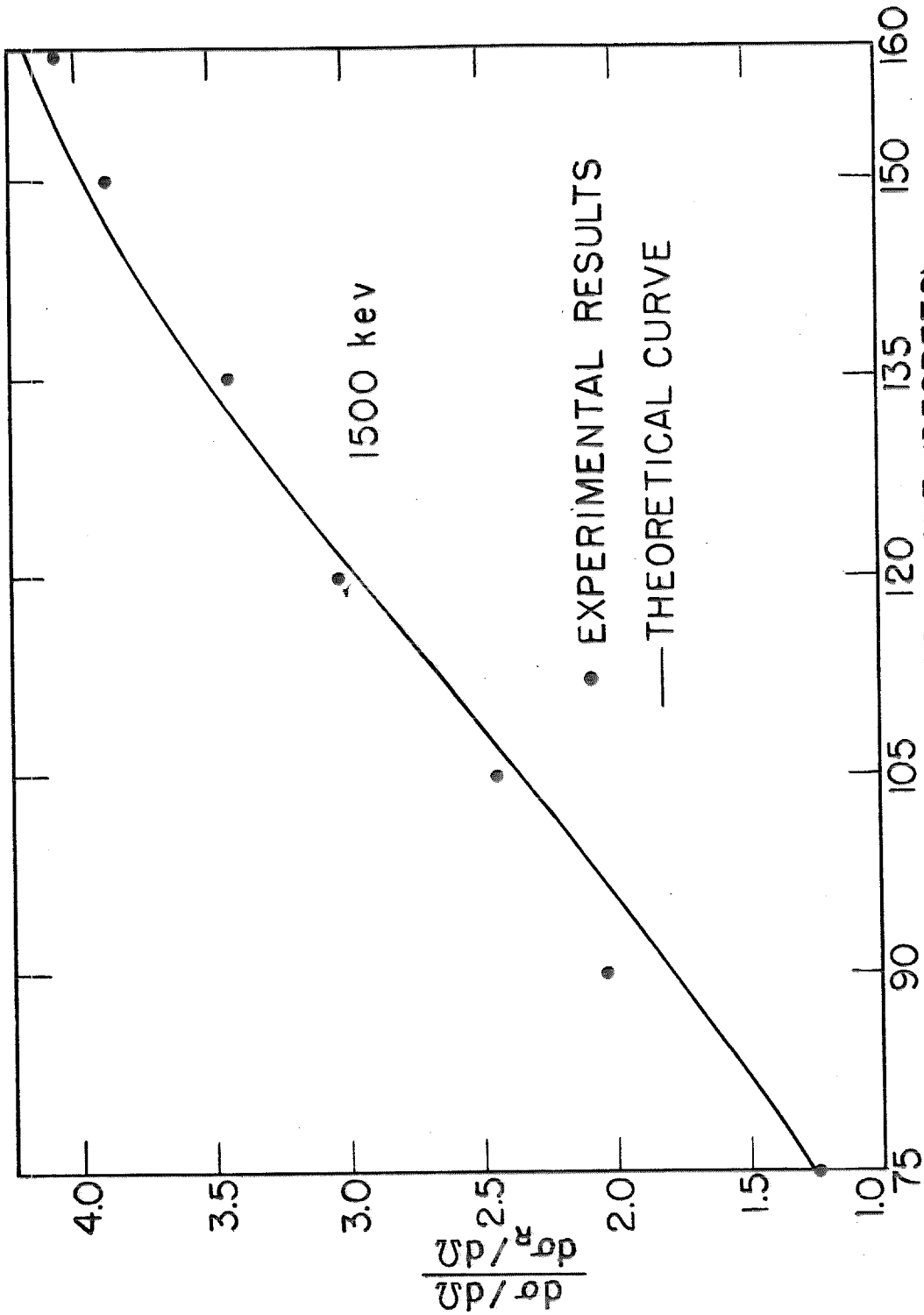
1500 kev
• EXPERIMENTAL RESULTS
— THEORETICAL CURVE
$\frac{d\sigma/d\Omega}{d\sigma_R/d\Omega}$
4.0
3.5
3.0
2.5
2.0
1.5
1.0
75
90
105
120
135
150
160
CENTER-OF-MASS ANGLE (DEGREES)

FIGURE 19

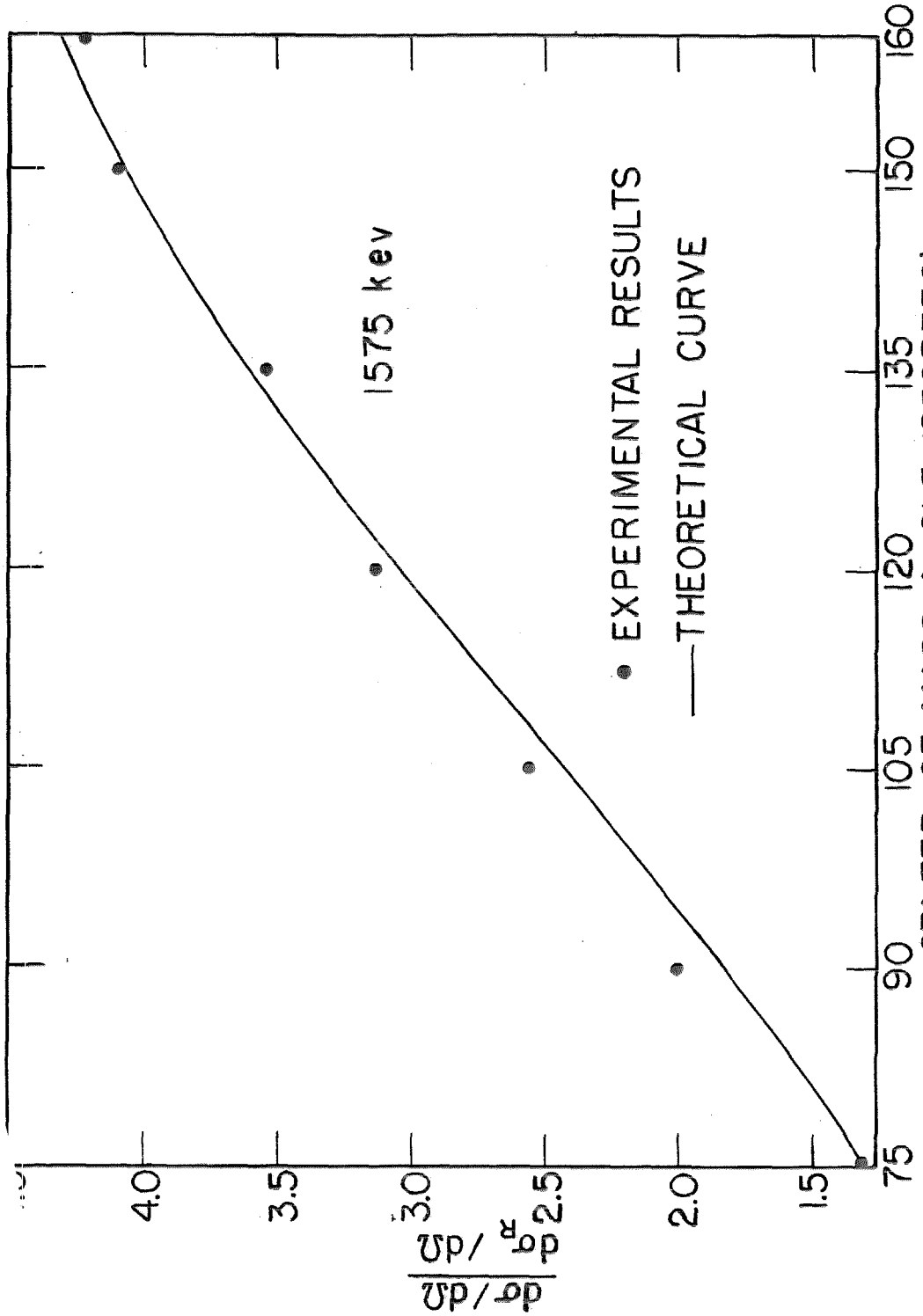
1575 kev
EXPERIMENTAL RESULTS
THEORETICAL CURVE
$\frac{d\sigma/d\Omega}{d\sigma_R/d\Omega}$
4.0
3.5
3.0
2.5
2.0
1.5
75
90
105
120
135
150
160
CENTER-OF-MASS ANGLE (DEGREES)

FIGURE 20

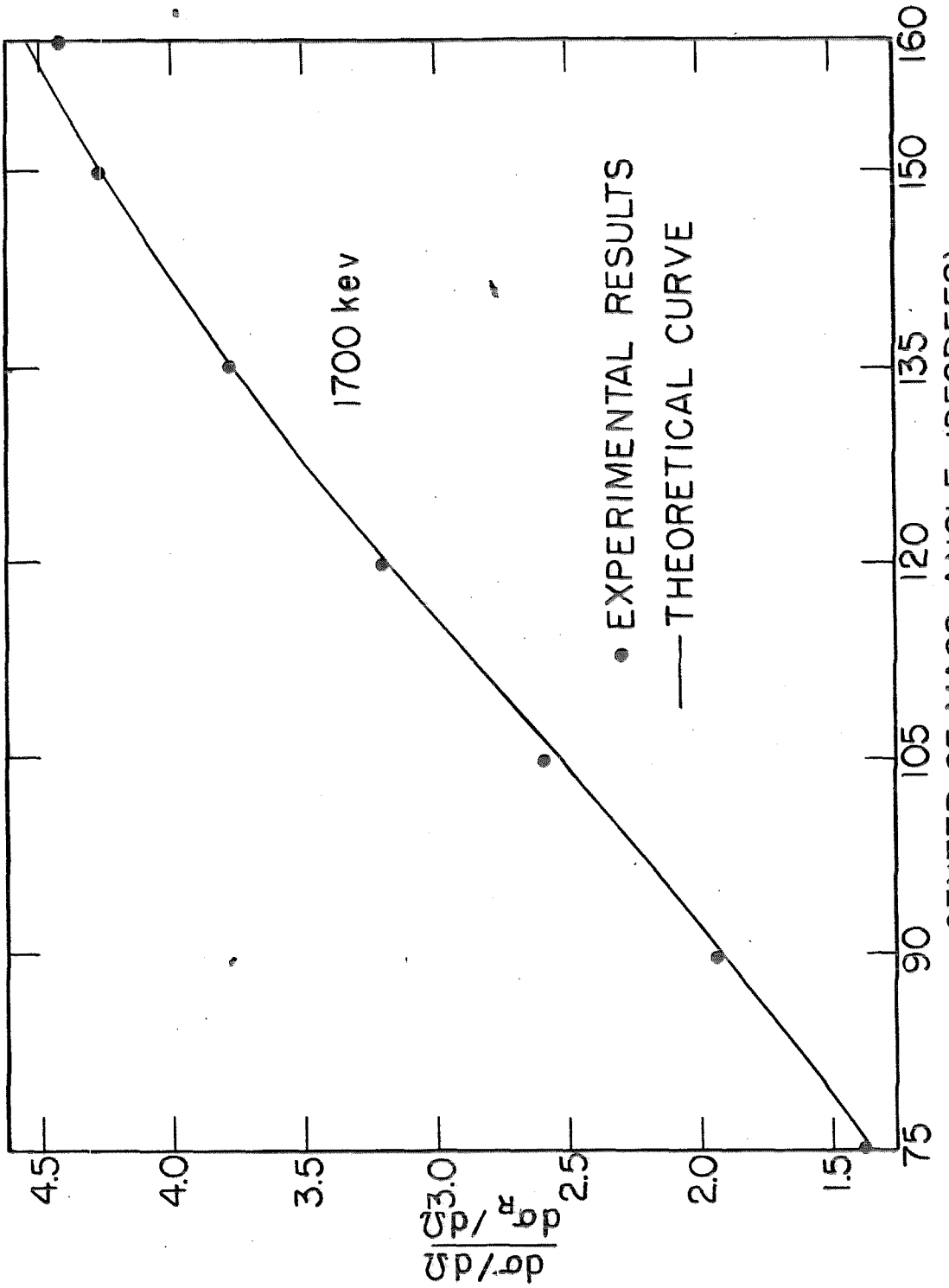
1700 kev
• EXPERIMENTAL RESULTS
— THEORETICAL CURVE
$\frac{d\sigma/d\Omega}{d\sigma_R/d\Omega}$
4.5
4.0
3.5
3.0
2.5
2.0
1.5
75
90
105
120
135
150
160
CENTER-OF-MASS ANGLE (DEGREES)

FIGURE 21

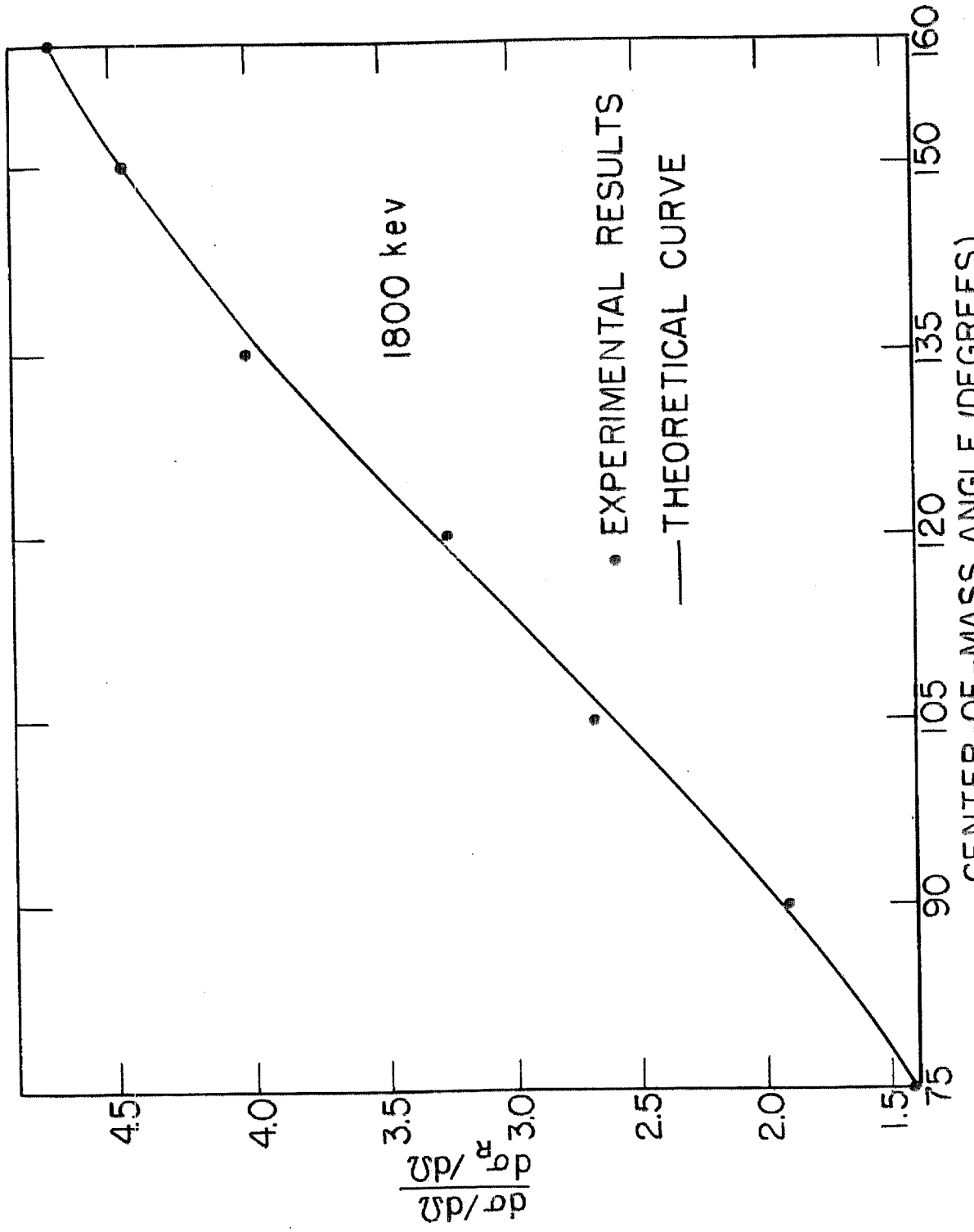
1800 kev
• EXPERIMENTAL RESULTS
— THEORETICAL CURVE
$\frac{d\sigma/d\Omega}{d\sigma_R/d\Omega}$
4.5
4.0
3.5
3.0
2.5
2.0
1.5
75
90
105
120
135
150
160
CENTER-OF-MASS ANGLE (DEGREES)

FIGURE 22

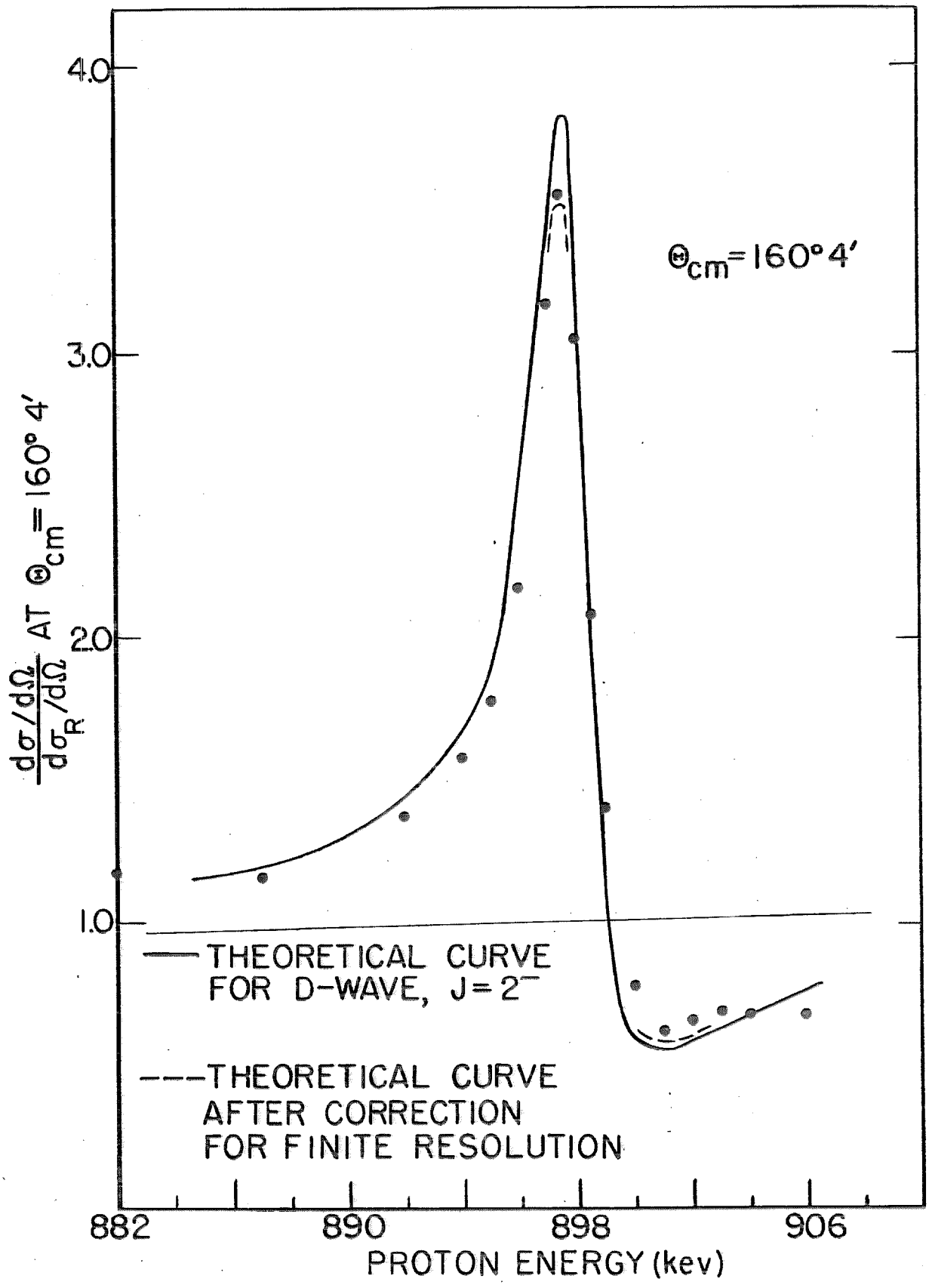
4.0
3.0
2.0
1.0
$\frac{d\sigma/d\Omega}{d\sigma_R/d\Omega}$ AT $\Theta_{cm}=160°4'$
$\Theta_{cm}=160°4'$
THEORETICAL CURVE FOR D-WAVE, J=2⁻
---THEORETICAL CURVE AFTER CORRECTION FOR FINITE RESOLUTION
882
890
898
906
PROTON ENERGY (kev)

FIGURE 23

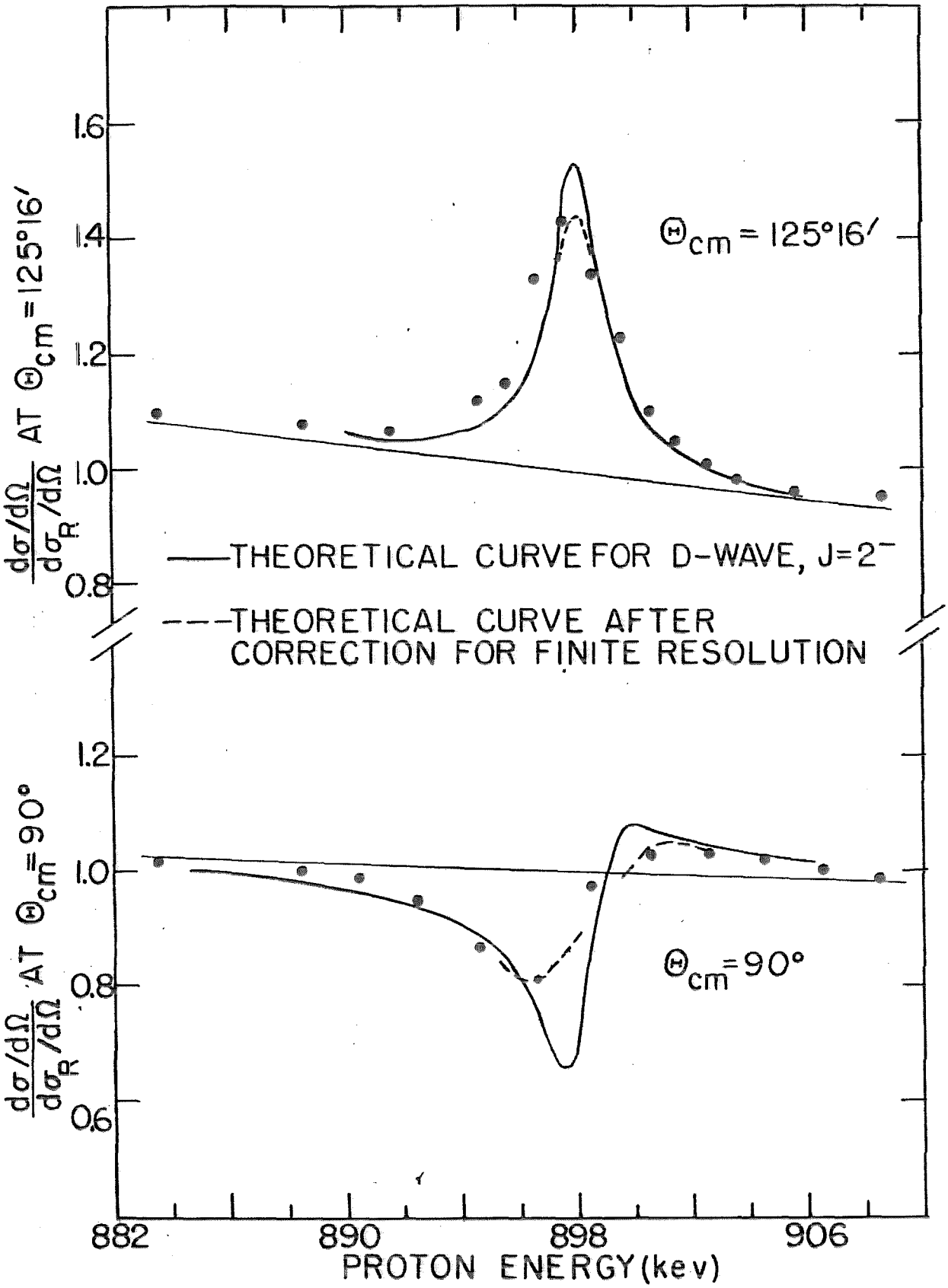
1.6
1.4
1.2
1.0
0.8
$\frac{d\sigma/d\Omega}{d\sigma_R/d\Omega}$ AT $\Theta_{cm}=125°16'$
$\Theta_{cm}=125°16'$
——THEORETICAL CURVE FOR D-WAVE, J=2⁻
---THEORETICAL CURVE AFTER CORRECTION FOR FINITE RESOLUTION
1.2
1.0
0.8
0.6
$\frac{d\sigma/d\Omega}{d\sigma_R/d\Omega}$ AT $\Theta_{cm}=90°$
$\Theta_{cm}=90°$
882
890
898
906
PROTON ENERGY (kev)

FIGURE 24

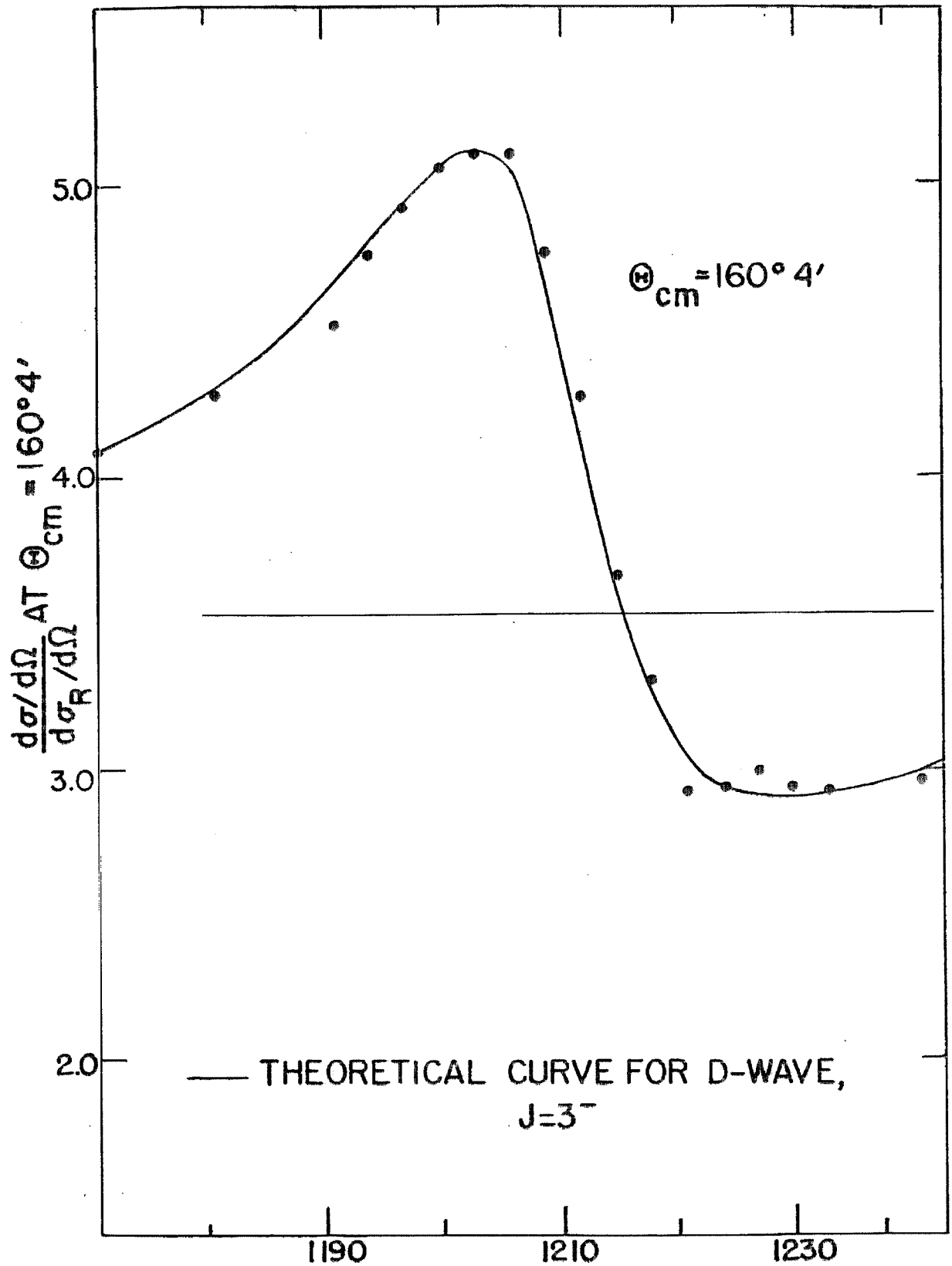
5.0
4.0
3.0
2.0
$\frac{d\sigma/d\Omega}{d\sigma_R/d\Omega}$ AT Θ_{cm} = 160° 4'
Θ_{cm} = 160° 4'
THEORETICAL CURVE FOR D-WAVE, J=3⁻
1190
1210
1230
PROTON ENERGY (kev)

FIGURE 25

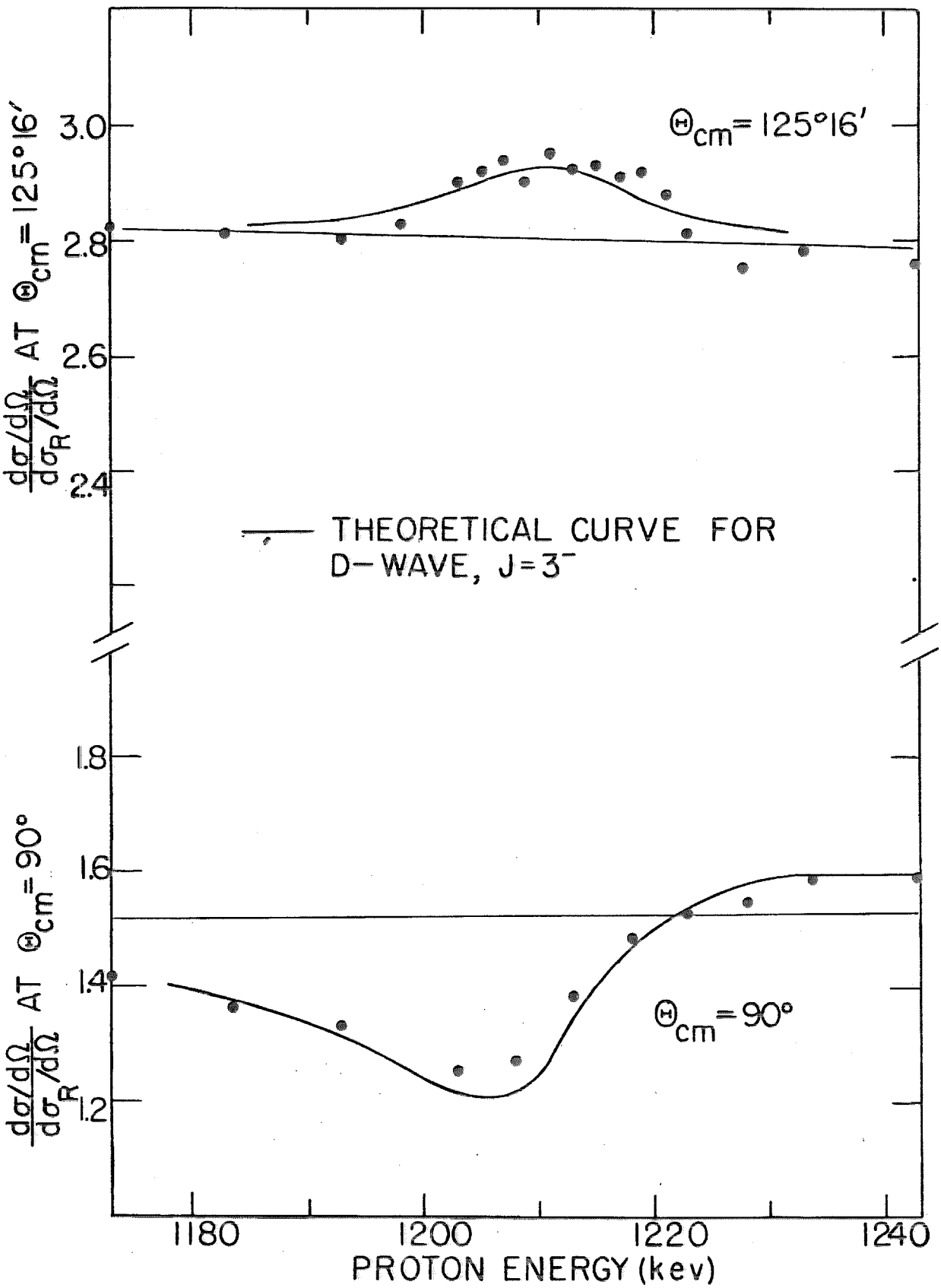
$\frac{d\sigma/d\Omega}{d\sigma_R/d\Omega}$ AT Θ_{cm} = 125°16′
3.0
2.8
2.6
2.4
Θ_{cm} = 125°16′
THEORETICAL CURVE FOR
D-WAVE, J=3⁻
$\frac{d\sigma/d\Omega}{d\sigma_R/d\Omega}$ AT Θ_{cm} = 90°
1.8
1.6
1.4
1.2
Θ_{cm} = 90°
1180
1200
1220
1240
PROTON ENERGY (kev)

FIGURE 26

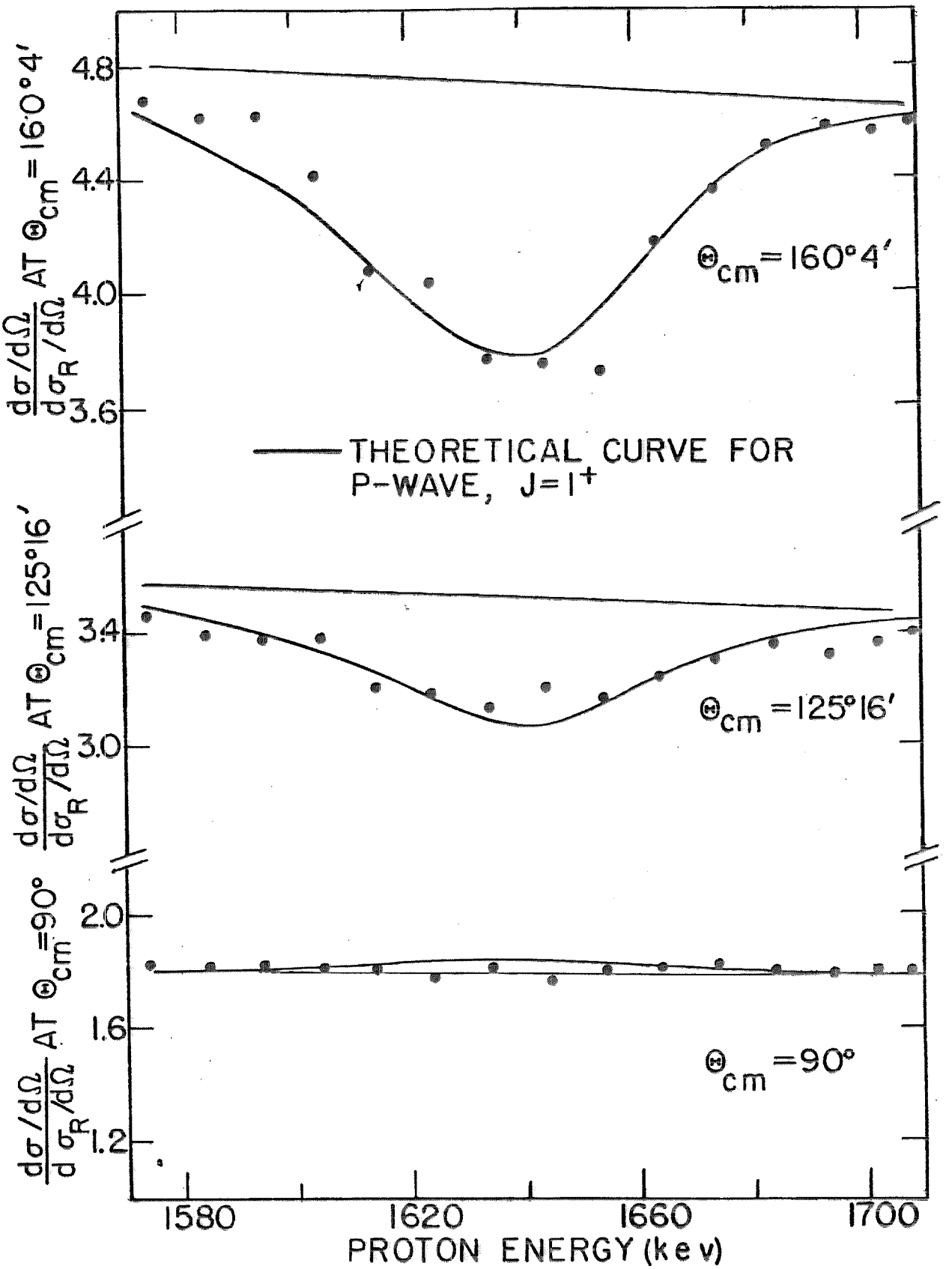
4.8
4.4
4.0
3.6
$\frac{d\sigma/d\Omega}{d\sigma_R/d\Omega}$ AT Θ_{cm}=160°4′
Θ_{cm}=160°4′
THEORETICAL CURVE FOR
P-WAVE, J=1+
3.4
3.0
$\frac{d\sigma/d\Omega}{d\sigma_R/d\Omega}$ AT Θ_{cm}=125°16′
Θ_{cm}=125°16′
2.0
1.6
1.2
$\frac{d\sigma/d\Omega}{d\sigma_R/d\Omega}$ AT Θ_{cm}=90°
Θ_{cm}=90°
1580
1620
1660
1700
PROTON ENERGY (kev)

FIGURE 27

OUTGOING CHANNEL SPIN CONFIGURATIONS FOR $N^{15}(p,p)N^{15}$

INCOMING CHANNEL SPIN CONFIGURATIONS

	(0, 0)	(1, 1)	(1, 0)	(1, −1)
(0,0)	$f_c + Y_0^0 f_{00ss}^0 + Y_1^0 f_{00pp}^1 + Y_2^0 f_{00dd}^2$	$\frac{1}{\sqrt{2}} Y_1^{-1} f_{01pp}^1 + \frac{1}{\sqrt{2}} Y_2^{-1} f_{01dd}^2$		$-\frac{1}{\sqrt{2}} Y_1^1 f_{01pp}^1 - \frac{1}{\sqrt{2}} Y_2^1 f_{01dd}^2$
(1,1)	$\frac{1}{\sqrt{2}} Y_1^1 f_{10pp}^1 + \frac{1}{\sqrt{2}} Y_2^1 f_{10dd}^2$	$f_c + Y_0^0 f_{11ss}^1 + \frac{1}{2} Y_1^0 f_{11pp}^1 + \frac{1}{2} Y_2^0 f_{11dd}^2 + \frac{2}{5} Y_2^0 f_{11dd}^3 + \frac{1}{\sqrt{15}} Y_4^0 f_{11dg}^3 + \frac{1}{3} Y_4^0 f_{11gg}^5$	$-\frac{1}{2} Y_1^1 f_{11pp}^1 - \frac{1}{2\sqrt{3}} Y_2^1 f_{11dd}^2 + \frac{4\sqrt{3}}{15} Y_2^1 f_{11dd}^3 - \frac{1}{\sqrt{6}} Y_4^1 f_{11dg}^3 + \sqrt{\frac{8}{45}} Y_4^1 f_{11gg}^5$	$-\frac{1}{\sqrt{6}} Y_2^2 f_{11dd}^2 + \frac{\sqrt{6}}{15} Y_2^2 f_{11dd}^3 + \frac{1}{\sqrt{6}} Y_4^2 f_{11dg}^3 + \sqrt{\frac{2}{45}} Y_4^2 f_{11gg}^5$
(1,0)		$-\frac{\sqrt{3}}{5} Y_2^{-1} f_{11dd}^3 + \frac{1}{\sqrt{6}} Y_4^{-1} f_{11dg}^3 + \frac{\sqrt{10}}{9} Y_4^{-1} f_{11gg}^5$	$f_c + Y_0^0 f_{11ss}^1 + \frac{3}{5} Y_2^0 f_{11dd}^3 - \frac{2}{\sqrt{15}} Y_4^0 f_{11dg}^3 + \frac{5}{9} Y_4^0 f_{11gg}^5$	$\frac{\sqrt{3}}{5} Y_2^1 f_{11dd}^3 + \frac{1}{\sqrt{6}} Y_4^1 f_{11dg}^3 + \frac{\sqrt{10}}{9} Y_4^1 f_{11gg}^5$
(1,−1)	$-\frac{1}{\sqrt{2}} Y_1^{-1} f_{10pp}^1 - \frac{1}{\sqrt{2}} Y_2^{-1} f_{10dd}^2$	$-\frac{1}{\sqrt{6}} Y_2^{-2} f_{11dd}^2 + \frac{\sqrt{6}}{15} Y_2^{-2} f_{11dd}^3 + \frac{1}{\sqrt{6}} Y_4^{-2} f_{11dg}^3 + \sqrt{\frac{2}{45}} Y_4^{-2} f_{11gg}^5$	$-\frac{1}{2} Y_1^{-1} f_{11pp}^1 + \frac{1}{2\sqrt{3}} Y_2^{-1} f_{11dd}^2 + \frac{4\sqrt{3}}{15} Y_2^{-1} f_{11dd}^3 - \frac{1}{\sqrt{6}} Y_4^{-1} f_{11dg}^3 + \sqrt{\frac{8}{45}} Y_4^{-1} f_{11gg}^5$	$f_c + Y_0^0 f_{11ss}^1 + \frac{1}{2} Y_1^0 f_{11pp}^1 + \frac{1}{2} Y_2^0 f_{11dd}^2 + \frac{2}{5} Y_2^0 f_{11dd}^3 + \frac{1}{\sqrt{15}} Y_4^0 f_{11dg}^3 + \frac{1}{3} Y_4^0 f_{11gg}^5$

FIGURE 28

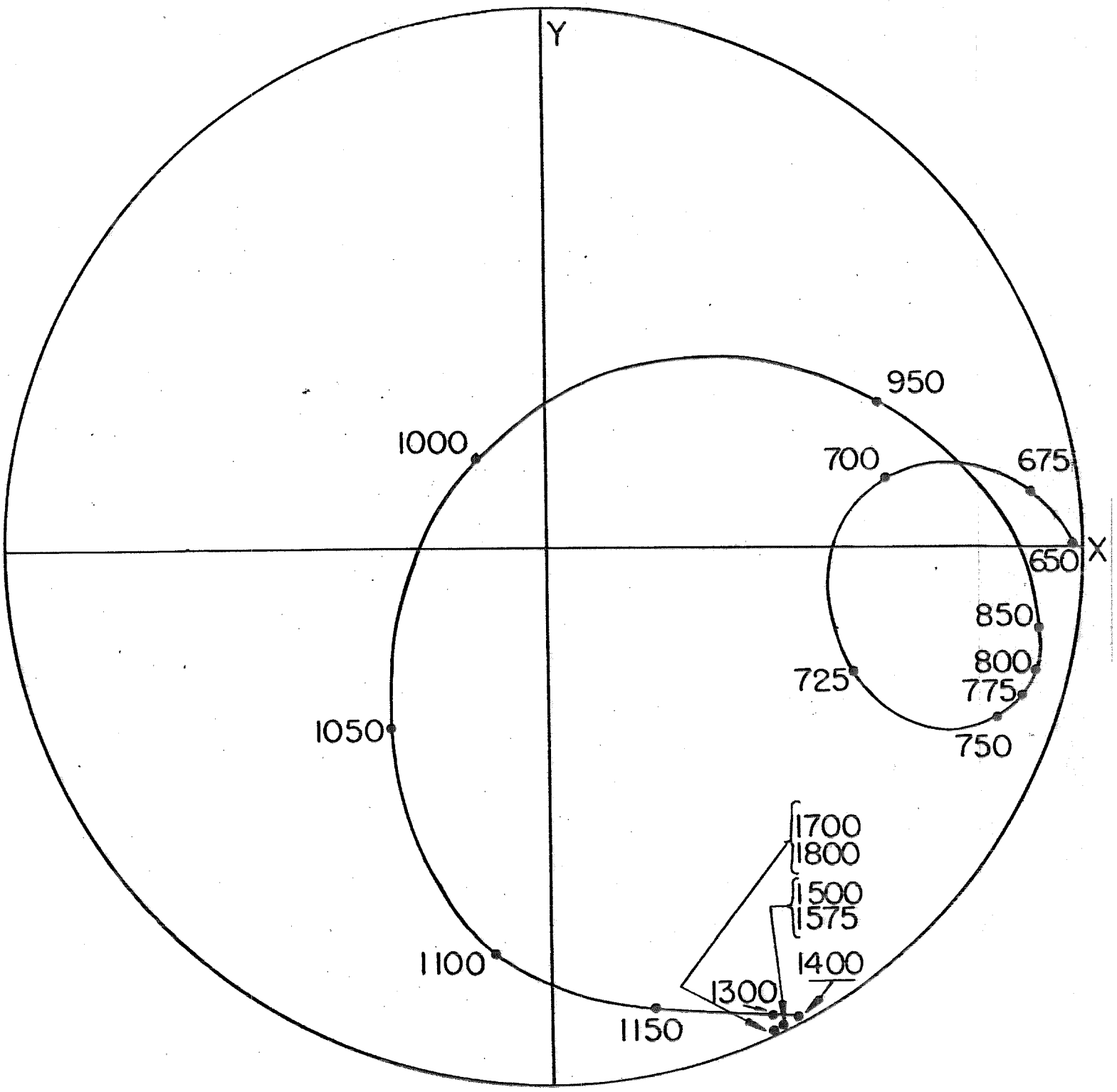

SCATTERING AMPLITUDE DIAGRAM

FIGURE 29

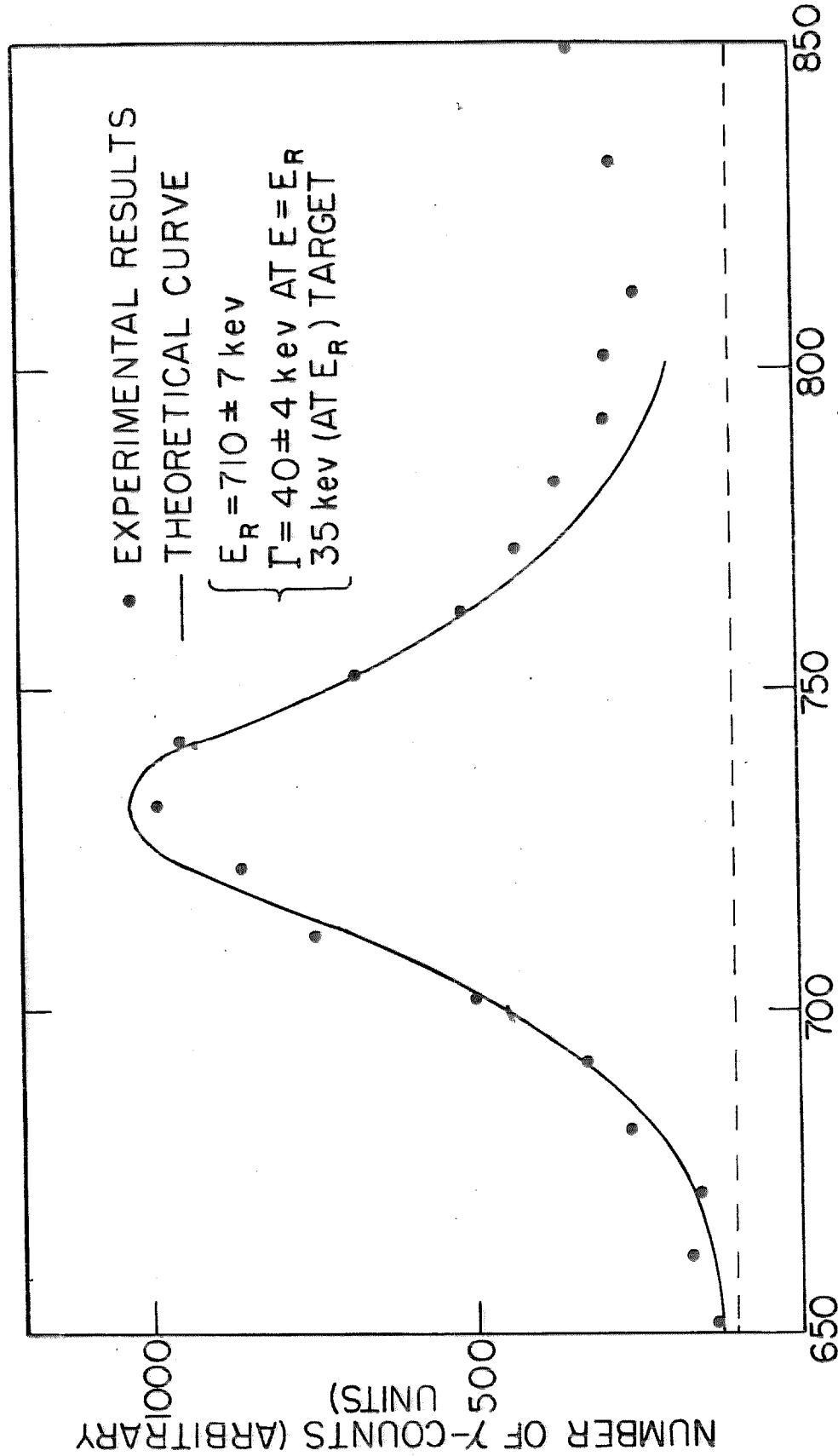
• EXPERIMENTAL RESULTS
— THEORETICAL CURVE
E_R = 710 ± 7 kev
Γ = 40 ± 4 kev AT E = E_R
35 kev (AT E_R) TARGET
NUMBER OF γ-COUNTS (ARBITRARY UNITS)
1000
500
650
700
750
800
850
INCIDENT PROTON ENERGY (kev)

FIGURE 30

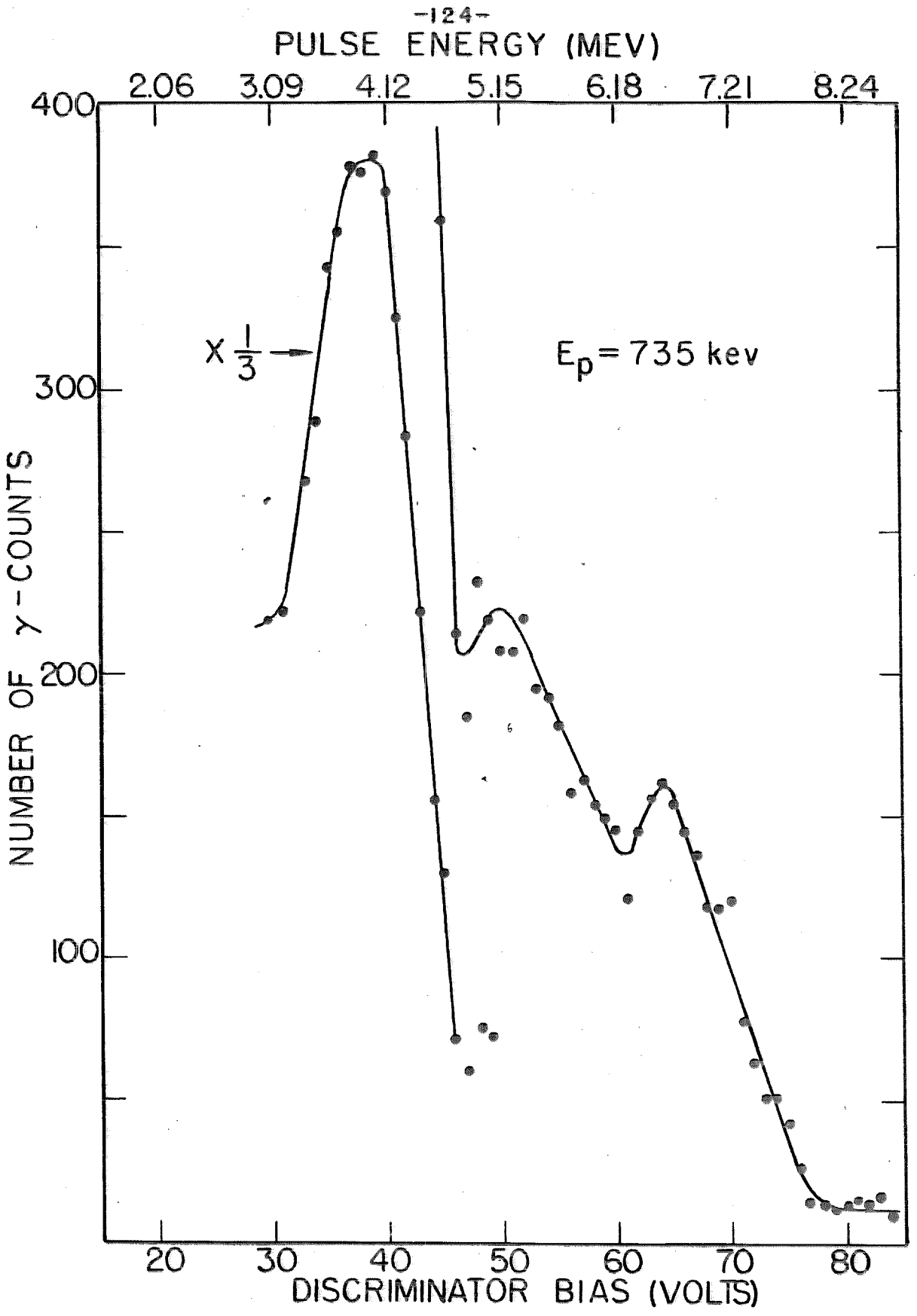
PULSE ENERGY (MEV)
2.06
3.09
4.12
5.15
6.18
7.21
8.24
400
300
200
100
NUMBER OF γ-COUNTS
X 1/3
Ep = 735 kev
20
30
40
50
60
70
80
DISCRIMINATOR BIAS (VOLTS)

FIGURE 31

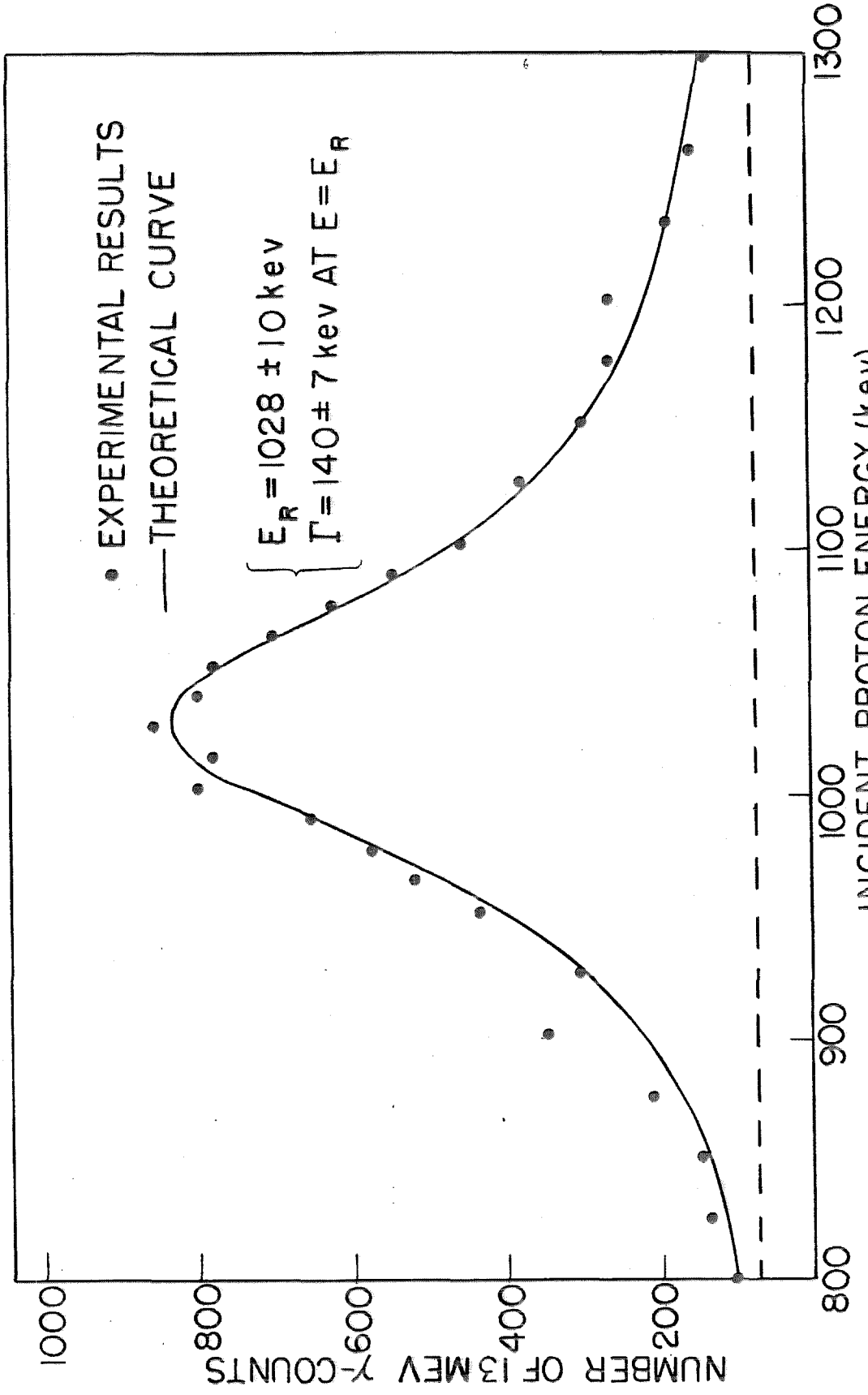
• EXPERIMENTAL RESULTS
—THEORETICAL CURVE
E_R = 1028 ± 10 kev
Γ = 140 ± 7 kev AT E = E_R
NUMBER OF 13 MEV γ-COUNTS
INCIDENT PROTON ENERGY (kev)
800
900
1000
1100
1200
1300
200
400
600
800
1000

FIGURE 32

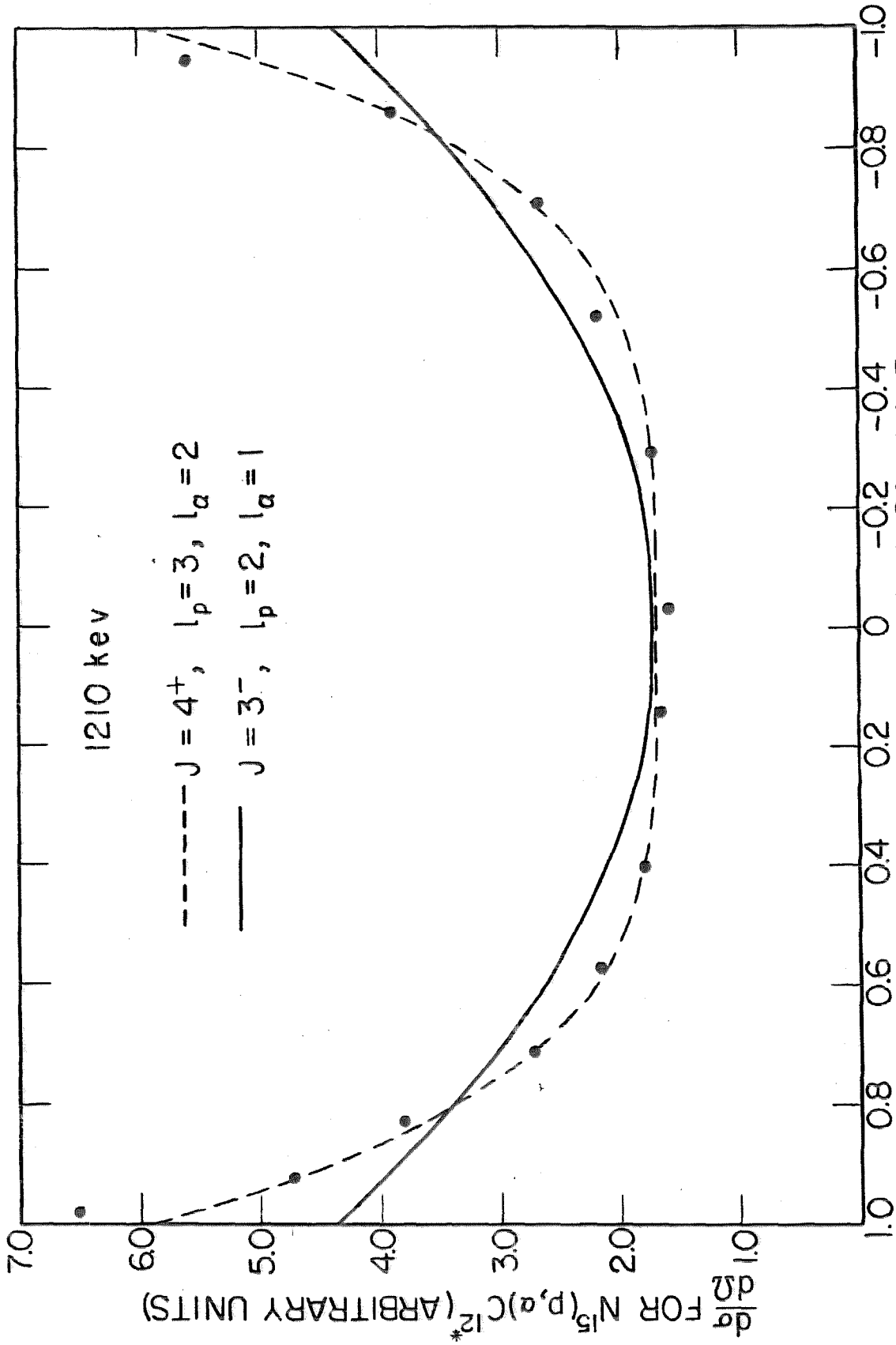
1210 kev
J = 4+, Lp = 3, La = 2
J = 3−, Lp = 2, La = 1
dσ/dΩ FOR N15(p,α)C12* (ARBITRARY UNITS)
COSINE CENTER-OF-MASS ANGLE
7.0
6.0
5.0
4.0
3.0
2.0
1.0
1.0
0.8
0.6
0.4
0.2
0
-0.2
-0.4
-0.6
-0.8
-1.0

FIGURE 33

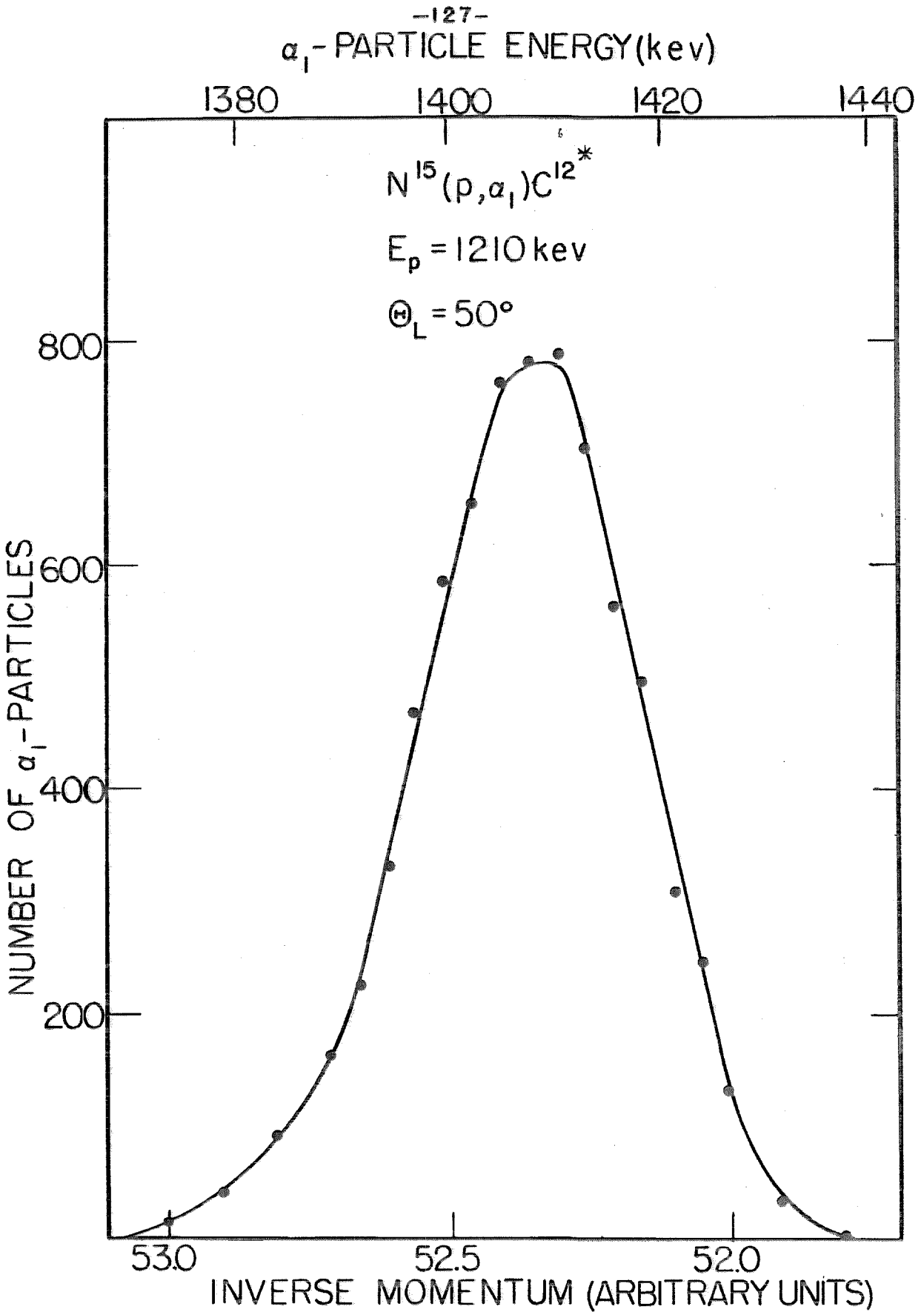
α_1-PARTICLE ENERGY(kev)
1380
1400
1420
1440
$N^{15}(p,\alpha_1)C^{12*}$
E_p = 1210 kev
Θ_L = 50°
800
600
400
200
NUMBER OF α_1-PARTICLES
53.0
52.5
52.0
INVERSE MOMENTUM (ARBITRARY UNITS)

FIGURE 34

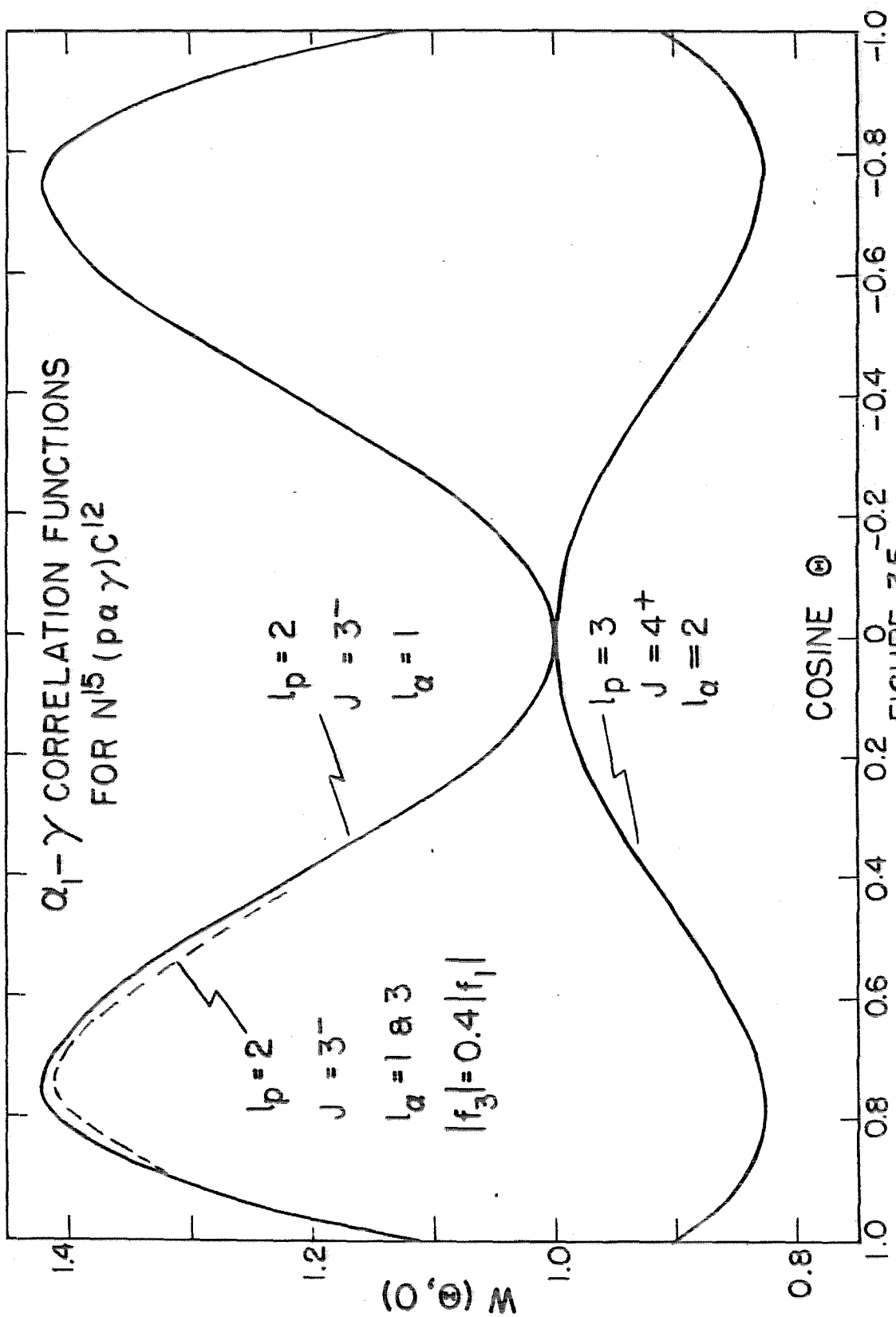
$\alpha_1-\gamma$ CORRELATION FUNCTIONS
FOR $N^{15}(p\alpha\gamma)C^{12}$
$l_p=2$
$J=3^-$
$l_\alpha=1$
$l_p=2$
$J=3^-$
$l_\alpha=1\ \&\ 3$
$|f_3|=0.4|f_1|$
$l_p=3$
$J=4^+$
$l_\alpha=2$
W (Θ, 0)
COSINE Θ
1.4
1.2
1.0
0.8
1.0
0.8
0.6
0.4
0.2
0
-0.2
-0.4
-0.6
-0.8
-1.0

FIGURE 35

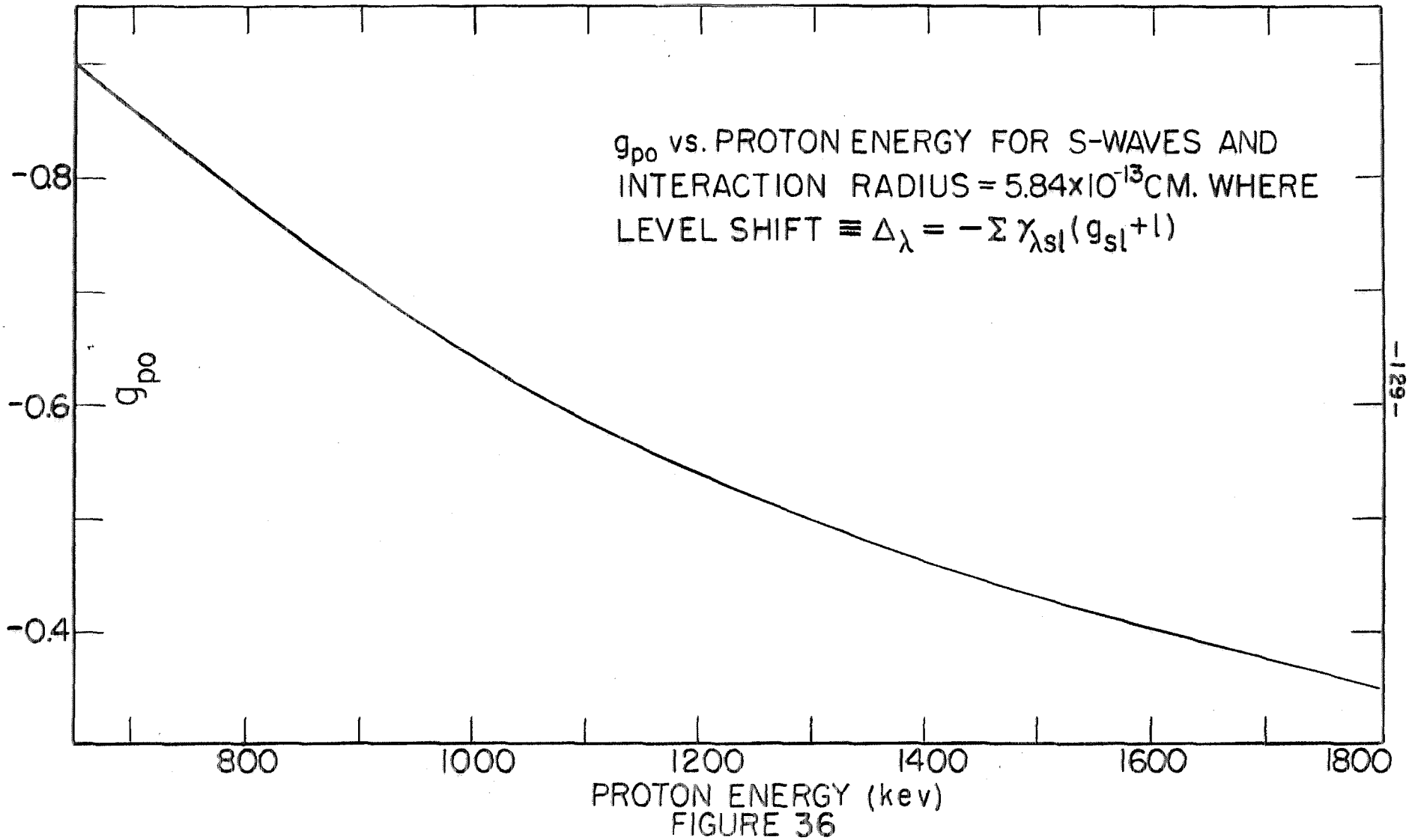
g_{po} vs. PROTON ENERGY FOR S-WAVES AND
INTERACTION RADIUS = 5.84×10^{-13} CM. WHERE
LEVEL SHIFT $\equiv \Delta_\lambda = -\Sigma \gamma_{\lambda sl}(g_{sl}+1)$
g_{po}
-0.8
-0.6
-0.4
800
1000
1200
1400
1600
1800
PROTON ENERGY (kev)
FIGURE 36